Adaptation of Nontraditional Control Techniques to Nonlinear Micro and Macro Mechanical Systems

Mohammed F. Daqaq

Dissertation submitted to the Faculty of the
Virginia Polytechnic Institute and State University
in partial fulfillment of the requirements for the degree of

Doctor of Philosophy
in
Engineering Mechanics

Ali H. Nayfeh, Chair
Craig Woolsey
Daniel J. Inman
Saad Ragab
Scott L. Hendricks

July 28, 2006
Blacksburg, Virginia

Keywords: Container crane, Torsional micromirror, Delayed-position feedback, Input shaping, Nonlinear interaction, Reduced-order model.

Adaptation of Nontraditional Control Techniques to Nonlinear Micro and Macro Mechanical Systems

Mohammed F. Daqaq

(ABSTRACT)

We investigate the implementation of nontraditional open-loop and closed-loop control techniques to systems at the micro and macro scales. At the macro level, we consider a quay-side container crane. It is known that the United States relies on ocean transportation for 95% of cargo tonnage that moves in and out of the country. Each year over six million loaded marine containers enter U.S. ports. Current growth predictions indicate that container cargo will quadruple in the next twenty years. To cope with this rapid growth, we develop a novel open-loop input-shaping control technique to mitigate payload oscillations on quay-side container cranes. The proposed approach is suitable for automated crane operations, does not require any alterations to the existing crane structure, uses the maximum crane capabilities, and is based on an accurate two-dimensional four-bar-mechanism model of a container crane. The shaped commands are based on a nonlinear approximation of the two-dimensional model frequency and, unlike traditional input-shaping techniques, our approach can account for large hoisting operations. For operator-in-the-loop crane operations, we develop a closed-loop nonlinear delayed-position feedback controller. Key features of this controller are that it: does not require major modifications to the existing crane structure, accounts for motion inversion delays, rejects external disturbances, and is superimposed on the crane operator commands. To validate the controllers, we construct a 1:10 scale model of a 65-ton quay-side container crane. The facility consists of a 7-meter track, 3.5-meter hoisting cables, a trolley, a traverse motor, two hoisting motors, and a 50-pound payload. Using this setup, we demonstrated the effectiveness of the controllers in mitigating payload oscillations in both of the open-loop and closed-loop modes of operation.

At the micro level, we consider a micro optical device known as the torsional micromirror. This device has a tremendous number of industrial and consumer market applications in-

cluding optical switching, light scanning, digital displays, etc. To analyze this device, we develop a comprehensive model of an electrically actuated torsional mirror. Using a Galerkin expansion, we develop a reduced-order model of the mirror and verify it against experimental data. We investigate the accuracy of representing the mirror using a two-degrees-of-freedom lumped-mass model. We conclude that, under normal operating conditions, the statics and dynamics of the mirror can be accurately represented by the simplified lumped-mass system. We utilize the lumped-mass model to study and analyze the nonlinear dynamics of torsional micromirrors subjected to combined DC and resonant AC excitations. The analysis is aimed at enhancing the performance of micromirrors used for scanning applications by providing better insight into the effects of system parameters on the microscanner's optimal design and performance. Examining the characteristics of the mirror response, we found that, for a certain DC voltage range, a two-to-one internal resonance might be activated between the first two modes. Due to this internal resonance, the mirror exhibits complex dynamic behavior. This behavior results in undesirable vibrations that can be detrimental to the scanner performance.

Torsional micromirrors are currently being implemented to provide all-optical switching in fiber optic networks. Traditional switching techniques are based on converting the optical signal into electrical signal and back into optical signal before it can be switched into another fiber. This reduces the rate of data transfer substantially. To realize fast all-optical switching, we enhance the transient dynamic characteristics and performance of torsional micromirrors by developing a novel technique for preshaping the voltage commands applied to activate the mirror. This new approach is the first to effectively account for inherent nonlinearities, damping effects, and the energy of the significant higher modes. Using this technique, we are able to realize very fast switching operations with minimal settling time and almost zero overshoot.

Dedication

To my parents with all my love and admiration ...

Acknowledgments

I would like to start by thanking two people to whom I am extremely indebted. My advisors Drs. Ali Nayfeh and Ziyad Masoud, without whom, the completion of this work would not have been possible. Their encouragement, patience, resourcefulness, thoughtfulness, and support have enlightened my path.

I would also like to thank my committee members: Dr. Daniel Inman, for his support, encouragement, and caring attitude. It is an honor to have worked with him; Dr. Craig Woolsey, for his friendship, brilliant comments, and fresh ideas. To him, I owe my current knowledge in control theory; Dr. Saad Ragab for his advice, encouragement, and patience; and Dr. Scott Hendricks for his support and unbelievable teaching skills. He has a unique approach to explaining dynamics which expanded my horizon and increased my appreciation to this subject.

I would like to thank all of the people and friends I met as a part of the Nonlinear Dynamics group. Especially, Drs. Eihab Abdel-Rahman and Haider Arafat for their collaboration, unselfishness, and invaluable comments; I thank Dr. Zhao Pong, Dr. Mohammed Younis, Dr. Waleed Faris, Dr. Sameer Imam, Dr. Nader Nayfeh, Mr. Greg Vogl, Mr. Bashar Hammad, Mr. Osama Marzouk, Mr. Imran Akhtar, and particularly Mrs. Sally Shrader for her friendship and endless help in the last five years.

Special thanks and appreciation are due to my best friends: Mr. Rachad Al-Bundukji, Mr. Sameer Arabasi, Mr. Saif Rayyan, Mr. Basel Al-Sultan, Mr. Qasem Abdelal, Mr. Sadeq

Al-Nasser, Dr. Khaled Al-Hazza, Dr. Majed Majeed, Dr. Ziyad Masoud, Dr. Mohannad Al-Saghir, and Dr. Konda Reddy. Without them, my life in Blacksburg would not have been the same.

Most importantly, I would like to thank my family, without whom, I would not have been able reach this point: My father, Mr. Farid Daqaq, who has given more than he can to see me at this point in my career, his support, love, and care are greatly admired; My mother, Mrs. Hana Daqaq, for her endless love, kindness, support, encouragement, and continuous care from day one. I would like to tell her that her dream has come true; My brother and sisters, Alia, Ruba, Manal, and Nihad, for their endless love, patience, care, and encouragement; and finally my aunts, Nabila and Rudayna, for their continuous love, encouragement and support.

Finally, I would like to thank God for all his blessings, especially, my family, friends, advisors, and the opportunity to accomplish this work.

Contents

List of Figures

List of Tables

Chapter 1

Introduction

This dissertation is divided into two major topics that deal with modeling, dynamics, and effective control of systems at the micro and macro scale. We consider a quay-side container crane as an example at the macro level and an optical micro device known as a torsional micromirror as an example at the micro level. In analyzing both topics, we follow similar guidelines. We start by developing a comprehensive model of the system at hand. We carefully analyze the model and use it to study the linear and nonlinear dynamics of the system. Based on this careful analysis, we develop a reduced-order model that captures the significant dynamics of the system. We utilize the resulting reduced-order model to develop effective control techniques that enhance the dynamic characteristics of each system.

In this Chapter, we present a general overview of quay-side container cranes and the latest advances in the modeling, dynamics, and control of cranes. Afterwards, we provide a general description of torsional micromirrors and their applications in optics. We shed some light on the major contributions and advances in the field of optical switching and present the major contributions and the outline of this dissertation.

1.1 Quay-Side Container Cranes

1.1.1 Modeling of Cranes

Cranes play a very important role in transportation and construction. As a result, there is an increasing demand on faster, bigger, and more efficient cranes to guarantee fast turn-around time, while meeting safety requirements. A crane consists of two main parts: a support mechanism (girder, jib, or a boom) and a hoisting mechanism, traditionally hoisting or multihoisting cables that are connected to a trolley or the boom tip at one side and to a hook or a spreader bar on the other side. The support mechanism delivers the payload to the target point, and the hoisting mechanism raises and lowers the payload to avoid obstacles in the path and deposit the payload at the target point.

A particularly important type of cranes is that of a quay-side container crane, Fig. 1.1, which is used to transfer payloads (containers) from ships to shore and vise versa. In this case, the supporting mechanism consists of a trolley moving along a girder, and the hoisting mechanism consists of four hoisting cables that are attached on one side to the trolley and on the other end to a spreader bar, which grabs containers. A special case of quay-side container cranes is that of a gantry or an overhead crane. Gantry cranes are much smaller than container cranes and have a similar support mechanism. The hoisting mechanism however is significantly different, it consists of one cable attached to the trolley at one side and to a hook, which grabs payloads on the other side.

Traditionally, a gantry crane is modeled as a simple pendulum with a rigid or flexible hoisting cable and a lumped mass at the end of the cable. The two most commonly used modeling approaches for gantry cranes are the lumped-mass and distributed-mass models. In the distributed-mass model, the hoisting cable is modeled as a distributed mass and the hook and payload are lumped as a point mass, which is applied as a boundary condition to this system. d'Andrea-Novel et al. [1, 2] and d'Andrea-Novel and Boustany [3] used the distributed-mass model. They ignored the inertia of the payload and modeled the cable

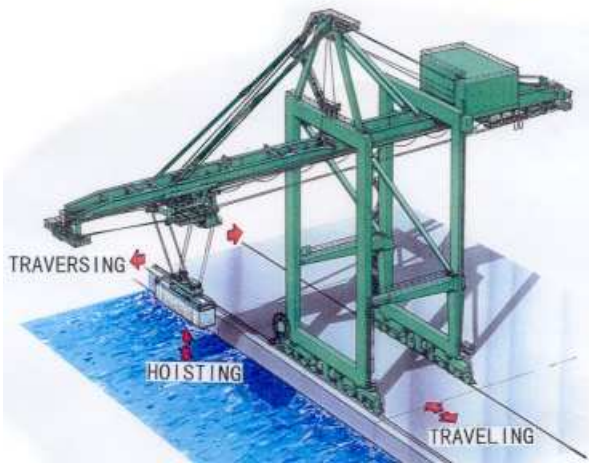

Figure 1.1: Typical quay-side container crane.

as a perfectly flexible, inextensible body using the wave equation. Others [4–6] extended the model to include the inertia of the payload by changing the boundary conditions at the payload end. However, the most widely used approach for crane modeling is the lumped-mass approach. The hoisting line is treated as a massless rigid link, and the payload is lumped with the hook and modeled as a point mass.

In the case of quay-side container cranes, the model is significantly different and therefore can not be modeled as a simple pendulum. The cables are hoisted from four different points on a trolley and are attached on the payload side to four points on a spreader bar, which lifts containers. The only accurate model available for quay-side container cranes is that of Masoud et al. [7] and Nayfeh [8]. They introduced a two-dimensional four-bar-mechanism model of a container crane. They considered the payload as a rigid body attached to two rigid massless links representing two of the four suspension cables. Using the geometry of the crane, the model was further simplified to a double pendulum with a kinematic constraint between the angles of both links of the pendulum.

1.1.2 Control of Cranes

Control of suspended objects, such as cranes, has seen mounting research interest since the early 1960's. Inertial forces on the payload due to crane commanded trajectories or operators commands can cause the payload to experience large sway oscillations. To avoid exciting these oscillations, crane operators resort to slowing down the operations so that oscillations do not cause safety concerns and possible damage of the payload. However, slowing down operations increases the cost of loading and unloading containers.

The level of control of payload oscillations varies according to the application at hand. In some applications, oscillations are acceptable while the payload is on its way to target, while the settling time and residual oscillations are kept very small to allow for accurate payload positioning. In other applications, such as nuclear reactors, or where the space around the crane is populated, the safety requirements are very strict. Thus large oscillations are not acceptable during and at the end of a transfer maneuver.

To achieve fast payload transfer operations while meeting the requirement of minimum oscillations during and at the end of the transfer maneuvers. Researchers have developed and implemented various control algorithms especially on gantry cranes. Next, we present a review of the major advances in this field.

Input-shaping control

One widely used open-loop control technique is input shaping [9]. For a long time, input shaping has been successfully implemented to improve the dynamic behavior of various systems at the macro scale. This technique uses a sequence of unique impulses to generate the desired input. When these impulses are convolved with the original input to the system, they result in zero residual vibrations. The magnitudes and time locations of the impulses are obtained by solving a set of vibration constraint equations derived from the response of the system to these impulses. In the frequency domain, input shaping has the effect of

producing zeros near the poles of the original system. The effectiveness of input shaping comes from the fact that it does not require any alterations to the original structure of the device or the installation of any additional mechanical and electronic components. It also uses the maximum system capabilities and usually generates smooth motion profiles.

Input-shaping technology is well established for linear systems. The technique uses estimates of the system's frequency and damping ratio to shape the input commands. Command shaping arguably started when Smith [9] proposed a method called the "Posicast Control" to move a plant without exciting its resonant frequency. His algorithm was based on shaping the input by dividing a single-step input into two equal impulses delayed in time by half the period of the system frequency. Singer [10] revolutionized the technique when he formalized input shaping into a mathematical theory. Using the general formula for the linear response of a system to a sequence of impulses, he developed a mathematical expression for the magnitude of the residual vibrations as a function of the impulses' amplitudes and locations (*known as the shaper parameters*). He then chose the shaper parameters to drive the magnitude of the residual vibrations to zero. This shaper is called the zero-vibration (ZV) shaper.

To realize more robustness to errors in the frequency and damping estimates, Singer and Seering [11] proposed a technique known as the zero-vibration derivative (ZVD) shaper. This technique uses the derivatives of the residual vibrations with respect to the frequency and damping as additional constraints, which are solved simultaneously with the residual vibration expression. Although, this technique was proven useful for very small frequency and damping variations, it did not provide an effective alternative to shape input commands for linear time-variant (LTV) systems where the frequency and/or damping vary significantly. In addition, this technique requires more and more impulses to be convolved with the original input to produce more zeros in the frequency domain, which drastically increases the shaped input duration, resulting in a longer shaper, and therefore a slower device operation.

Singhose [12], on the other hand, obtained more robustness by developing the extra insensitive (EI) shaper. This shaper specifies a tolerance limit on the residual vibration and

releases the zero residual vibration constraint. Using this technique robustness to errors in the frequency and damping can be achieved, but with nonzero residual oscillations.

Others [11, 13, 14] extended the application of input-shaping theory to suppress vibrations of a multimode linear system with single or multiple actuators. Their idea was to develop a shaped command for each mode separately and then convolve these commands to achieve a longer but effective shaper.

For nonlinear systems, where the frequency varies with the input magnitude, a general theory of input shaping has not been developed. Smith et al. [15] studied the implementation of input shaping to a general single-degree-of-freedom nonlinear system. Based on the total energy of the system, he used a semi-analytical approach to calculate the locations and amplitudes of the impulses. His technique, though very promising, failed to effectively account for damping losses.

In many demonstrations, input shaping was used to control suspended objects, in general, and gantry cranes, in particular. Alsop et al. [16] were among the first to propose a crane controller based on input shaping. The controller was used to automate ore unloader by accelerating the trolley in steps of constant acceleration then killing the acceleration when the payload reaches zero-oscillation angle (after multiples of a full period). The trolley then coasts at constant speed along the path for a period of time necessary to complete the transfer maneuver. A replicate of the acceleration procedure is used in the deceleration stage. The switching times for the acceleration and deceleration steps were calculated using an iterative computer procedure. Alsop et al. used a linear frequency approximation of a simple pendulum model. Their results demonstrated very little residual oscillations, while transient oscillation angles were the order of 10° during the acceleration/deceleration stages.

Nonlinear frequency approximation of a simple pendulum was also used to improve the performance of the single-step (SS) controller [17, 18]. Numerical simulations demonstrated that an acceleration profile based on the nonlinear frequency approximation can dampen the residual oscillations two orders of magnitude more than that based on a linear frequency ap-

proximation. The enhanced performance was most pronounced for longer coasting distances and higher accelerations.

Alzinger and Brozovic [19] showed that a double-step (DS) acceleration/deceleration profile results in a significant reduction in the travel time over a one-step acceleration profile. Testing on an actual crane has shown that the DS acceleration profile can deliver both faster travel and minimal payload oscillations at the target point.

Starr [20] used a symmetric DS acceleration/deceleration shaped profile to transport a suspended object with minimal oscillations. A linear approximation of the period of the payload is used to calculate the switching times and to generate an analytical expression for the acceleration profile. This work was later extended by employing a nonlinear approximation of the payload frequency to generate SS and DS symmetric acceleration profiles [21].

The performance of traditional input-shaping techniques is very sensitive to changes in system parameters, time delays, and external disturbances, and they require "*highly accurate values of the system parameters*" to achieve satisfactory system response [22]. While a good design can minimize the controller's sensitivity to modeling errors, it is much harder to alleviate the controller's sensitivity to changes in the hoisting cable length.

Kress et al. [23] showed analytically that input shaping is equivalent to a notch filter applied to a general input signal and centered around the natural frequency of the payload. They applied a second-order robust notch filter to shape the acceleration input. Numerical simulation and experimental verification of this strategy on an actual bidirectional gantry crane, moving at an arbitrary step acceleration and changing cable length at a very slow constant speed, showed that the strategy was able to suppress residual payload oscillations. They extended this work by developing a command shaping notch filter to reduce payload oscillation on rotary cranes excited by the operator commands. It was reported that, in general, there was no guarantee that applying such filter to the operator's speed commands would result in excitation terms having the desired frequency content, and that it only works for low-speed and acceleration commands [24]. Parker et al. [25] experimentally verified the

numerical simulation results.

Singer et al. [22] applied the ZVD shaper to gantry cranes. They found that, for relatively small trolley velocity and acceleration, the ZVD shaper was capable of reducing the sensitivity of the shaper to small-length variations (25% of the initial length). However, it was noted that, although input shaping became more robust to changes in the frequency and damping, the proposed technique resulted in considerably slower operations since more impulses were included in the input.

Singhose et al. [26] developed four different input-shaping controllers. They reported that the best controller produced a reduction of 73% in transient oscillations over the time-optimal rigid-body commands. However, they noted that "*transient deflection with shaping increases with hoist distance, but not as severely as the residual oscillations*". The numerical simulations showed that "*the percentage in reduction with shaping is dependent on system parameters*". As a result, the four controllers suffered degradation in performance when applied to crane maneuvers that involved hoisting.

Singhose et al. [27] studied the effect of hoisting on the input-shaping control of gantry cranes by comparing the sensitivity of five different shapers to changes in the cable length. They found that the shapers were more robust when based on the average frequency of the payload oscillations during the transfer maneuver. However, the residual oscillations increased significantly as the hoist distance was increased, but were within acceptable values for small hoisting distances (25% of the initial cable length).

Most of the literature dealt with the problem of developing shapers for gantry cranes where the system has a single hoisting line and can be modeled as a simple pendulum. Hoisting or lowering in that case is usually less than 25% of the initial cable length, and the trolley traverse motion, velocity, and acceleration are very small when compared to quay-side container cranes. In addition, in the case of container cranes where the crane operator moves with the trolley, one can not use the traditional techniques to increase the robustness of the shaper. Convolving many impulses to the input command will not only increase the travel

time drastically, but will also generate successive steps of acceleration and deceleration of the trolley, which usually result in motion discomfort for the crane operator.

For container cranes, the hoisting operations are usually larger than 50% of the initial cable length and the trolley has large velocities and accelerations to enable more than 50 m of payload traverse motion in very small amount of time. Under these circumstances, the available input-shaping techniques will suffer significant degradation in performance and therefore can not be applied to effectively control the oscillations of containers on quay-side cranes.

Feedback control

There is a vast amount of research on linear, optimal, adaptive, and nonlinear feedback control techniques for gantry cranes. Here, we shed some light on the major contributions in these areas. A more complete review of the literature on the dynamics and control of gantry cranes can be found in [28].

Hazlerigg [29] was the first to implement a feedback control strategy to gantry cranes. He used a compensator to dampen out payload oscillations. His technique was capable of effectively controlling payload oscillations at the payload natural frequency, but, due to control spill over, it introduced oscillations at higher frequencies.

A two-phase control strategy was proposed by Ohnishi et al. [30]. The first phase is a linear feedback controller that stabilizes the payload around its equilibrium position. The second phase is an input shaper that decelerates the trolley to a complete stop. This strategy was capable of minimizing residual oscillations, but was 30% slower than uncontrolled maneuvers.

Ridout [31] used a PID controller to eliminate residual oscillations for constant cable-length operations. Experimental results showed good performance at constant cable lengths, but large oscillations were obtained for maneuvers involving large hoisting operations.

A hybrid controller was first proposed by Virkkunen and Marttinen [32]. A shaped profile

was used to drive the trolley all the way to the target point. At the target, a Linear Quadratic Regulator (LQR) was used to eliminate any residual oscillations resulting from the unmodeled dynamics and/or any external disturbances. The controller was successful in suppressing residual oscillations.

Caron et al. [33] generated optimal trolley trajectories that result in minimum transient and residual payload oscillations. A PI tracker was then used to track these paths. A numerical investigation showed that this technique was capable of producing minimal residual oscillations, but could not reject external disturbances.

Using a linearized time-varying model of the crane, Moustafa [34] designed a feedback controller to suppress payload oscillations due to trolley motion and cable hoisting. Numerical simulations showed that this method was capable of producing very small payload oscillations, but it resulted in a large trolley overshoot.

Lee et al. [35] implemented a control strategy consisting of a combination of PI and PD controllers to suppress payload oscillations on gantry cranes. The PI controller tracks the trolley position and the PD controller dampens payload oscillations. The control technique was tested experimentally and found to be effective in minimizing both transient and residual oscillations of the payload for constant cable-length maneuvers.

In an application to quay-side container cranes, Yong et al. [36, 37] developed a state feedback controller for a rail-mounted quay-side crane. They proposed a novel technique to measure the sway angle. This technique is based on mounting an inclinometer on the top surface of the spreader bar, and using the geometry of the crane and angle relations to recover the actual sway angle. Although, the sway-angle measurement was based on the actual geometry of the crane, the authors used a simple-pendulum model to express the dynamics of the payload and verified the results experimentally using a single-cable rubber-tired gantry crane.

Nonlinear control techniques were also implemented to suppress payload oscillations on gantry cranes. In one demonstration, Zinober [38] used the sliding-mode technique to minimize the travel time and payload oscillations. The technique is not sensitive to changes in

cable length and payload mass, and it is capable of rejecting external disturbances. However, numerical simulations showed that the travel time is 10% longer than the time-optimal rigid-body trajectory.

DeSantis and Krau [39] used the sliding-mode technique to control the in-plane and out-of-plane payload oscillations in a bidirectional gantry crane. They compared the performance of the controller to traditional linear feedback control techniques. They found that the nonlinear controller is more capable of coping with changes in the system frequency, unmodeled dynamics, and external disturbances. On the other hand, the linear feedback technique was less sensitive to time delays.

Yu et al. [40] used a perturbation analysis to separate the slow and fast dynamics of a gantry crane. Two PD controllers were incorporated into the system. The first is a motion tracking controller to track a predefined trolley motion profile and the second is a fast-input controller to suppress payload oscillations. Due to the approach used to develop the model, this technique is only effective when the payload mass is an order of magnitude larger than that of the trolley.

Researchers [41–44] extensively studied the possibility of using time delay to control mechanical systems. It has been noted that systems with time delays exhibit interesting complex responses. Time delay has the capability of stabilizing or destabilizing dynamic systems. For this reason, they have been used as simple switches to control the behavior of systems, either by damping out the oscillations or creating chaotic responses which are sometimes desirable to secure communication signals [45].

Cheng and Chen [46] proposed a control strategy which employs time-delay control and feedback linearization to move a crane along a predefined path and to eliminate residual oscillations. Their results showed that the strategy is capable of delivering the payload to its target with minimal transient oscillations and almost no residual oscillations.

Masoud et al. [7] and Nayfeh [8] introduced a two-dimensional four-bar-mechanism model of a container crane. They approximated the model with a constrained double pendulum

to find a linear frequency approximation of the payload oscillation. The resulting frequency was then used to find the delay and gain of a nonlinear delayed-position feedback controller. The resulting controller was applied to the full crane model. The controller proved to be very effective in suppressing the transient and residual oscillations of containers at large trolley speeds and accelerations. The controller is insensitive to changes in the cable length and can reject external disturbances without a large control effort. More importantly the controller can augment any time delays in the system to the time delay required to generate the control input.

Nayfeh et al. [47] numerically compared the delayed-position feedback controller to PID and LQR controllers. They found that the controller based on time-delay was more effective in suppressing payload oscillations especially for fast maneuvers that include large hoisting operations.

Unlike input-shaping techniques, a well designed feedback controller has the ability to reject external disturbances and is more robust to changes in the cable length. Linear feedback controllers however suffer significant degradation in the performance at large trolley speeds and usually require alterations to the crane structure. More importantly, due to the control effort, feedback controllers do not use the maximum crane capabilities in terms of the crane speed and acceleration, which results in slower operations. Unlike small gantry or overhead cranes, the operator cabin is installed on the trolley in quay-side cranes to allow for safe loading and unloading operations, therefore the trolley motion profile directly affects the operator. Feedback controllers usually result in motion profiles that can cause operator discomfort, which sometimes suspended their implementation on quay-side container cranes.

1.2 MOEMS-Based Torsional Mirrors

1.2.1 Overview of Torsional Micromirrors

The development of easy and cheap microfabrication techniques led to mounting research into the development of various microdevices. These devices are characterized by their light weight, small size, and low-energy consumption, which made them very attractive substitutes for large components in tremendous industrial, military, medical, automotive, space and consumer market applications. The development of such devices also opened a number of new research areas into their implementation in many systems, including airbag systems, vehicle security systems, active suspension, sports training devices, earthquake detection, tanks, airplanes, shock and tilt sensing, micropumps, optical switches, energy harvesting, and head-mounted displays.

Microdevices are usually actuated using simple input signals. These signals (magnetic, piezoelectric, electrostatic, thermal, etc.) are used to drive the device to a desired static configuration (e.g., micro-switches, optical crossconnects, thermal biomorphs, etc.) or to continuously excite the device to achieve a certain dynamic behavior (e.g., micro-resonators, micro-scanners, filters, etc.). A deep understanding of the behavior of these devices in response to these simple input signals is necessary to provide designers with insight into the proper choice of the design parameters. This results in a better response and maximum performance capabilities as well as reduction in the time and cost associated with the trial-and-error process that is currently used to design microsystems. However, the understanding of the behavior of systems at the micro scale is not a trivial problem. Their operations usually involve coupled-energy domains, where electrostatics, fluidics, thermodynamics, and dynamics are inherently coupled in complex manners that require interacting CAD solvers to simulate their performance.

Currently, Micro-Opto-Electromechanical Systems (MOEMS) is one of the fastest growing areas in the micro industry. These systems consist of two main components: an electronic

component, which provides the actuation signal and is fabricated using integrated circuit (IC) technology; and a mechanical component, which represents the moving parts of the device and is usually micromachined on a silicon wafer. To realize the optical characteristics of these devices, a very reflective surface, usually very thin metal aluminum or gold sheets, is attached to the moving mechanical components. These systems are used in the micro-optical industry, where the devices are used to steer, reflect, or modulate light, depending on the application at hand.

Torsional micromirrors, Fig. 1.2 (*with permission from Computer Optics, Inc.* [48]), is the most famous and widely used MOEMS device. A micromirror consists of two identical microbeams fixed on one side and connected to a rigid plate (the mirror) on the other side. Two electrodes mounted beneath the mirror are used to rotate the mirror in either direction by supplying a voltage to the corresponding electrode.

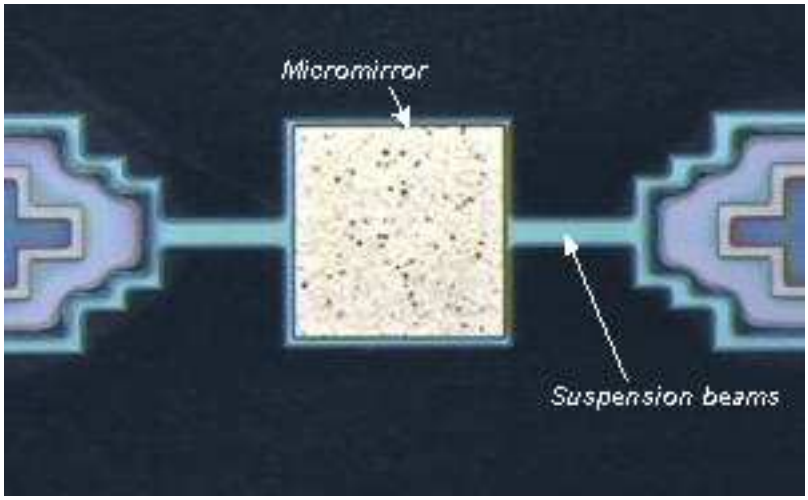

Figure 1.2: A microscopic view of a gold-plated torsional micromirror.

Torsional micromirrors are used for optical switching in fiber-optic networks [49–51], Fig. 1.3 (*with permission from Glimmerglass, Inc.* [52]). Optical networking depends on the development of optical switching technologies capable of transferring large volumes of data at high speed. The process of data transfer requires the light waves carrying the data to switch

from one fiber to another in order to reach their destination. If no switching occurs, each optical fiber is capable of transferring data in the range of hundreds of Gigabits per seconds [53]. Old switching techniques were based on converting optical signals to electrical signals and then back again to optical signals before they could be switched to another fiber. This optical-electrical conversion reduces the speed of data transmission substantially and causes data "traffic jams". After the development of the DWDM (Dense Wavelength Division Multiplexing) that allowed the growth of fiber-optic networks bandwidths, the search for better optical-switching techniques became a necessity.

Since optical fibres have a very small core diameter, usually between 2 and 10 micrometers, micromirrors were the best alternate solution for optical switching problems, their small size and light weight allow for easy implementation in fiber networks. In addition, micromirrors are capable of transmitting data only by reflecting light beams without converting light into electricity. This substantially increases the speed of optical switching and, therefore, increases the ability of fiber networks to handle data at any bandwidth.

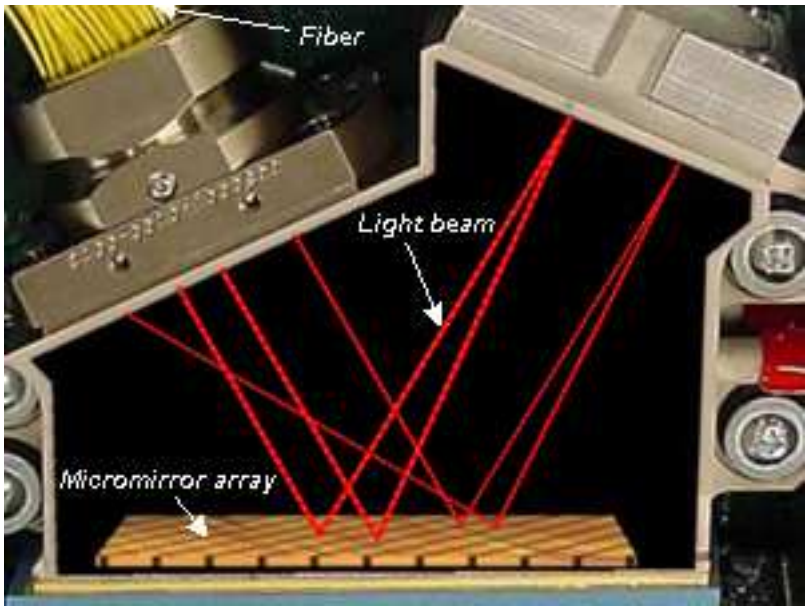

Figure 1.3: A schematic illustrating an array of micromirrors switching light between different fibers.

In optical switching applications, the micromirror needs to satisfy three requirements. The first is the realization of a precise orientation, which stems from the fact that unprecise mirror tilt angles might cause light beams to miss the small fiber core, especially if the distance between the micromirror and the fiber is increased, and hence might cause loss of data during switching. The second requirement is related to the dynamic response of the mirror to the step voltages used to actuate the mirror. In this aspect, the mirror is required to have minimal overshoot and settling time, which are necessary for minimizing the time between two successive switching operations. Finally, the magnitude of the step voltage required to drive the micromirror to the desired tilt angle needs to be minimal to minimize the power requirements of the electric circuits.

Torsional micromirrors are also implemented in projection displays [54]. Traditional projection displays are based on either Cathode-Ray Tubes (CRT), active matrix Liquid Crystal Displays (LCD), or Liquid Crystal Light Valves (LCLV). All of these technologies suffer either from performance or limitation problems. CRT and LCD suffer from stability and uniformity problems as well as limitations in their ability to produce high-brightness images. Although LCLVs were produced to overcome these shortcomings, they still suffer from stability problems and are very large and expensive.

To overcome these shortcomings, Texas Instruments used torsional micromirrors to produce the Digital Micro Device (DMD) [55, 56], Fig. 1.4 (*with permission from Texas Instruments.* [57]). The micromirror in this case serves as an electrostatically actuated light switch that reflects light from a light source through a lens to a screen. This technique has proved to be capable of producing stable, high-brightness images.

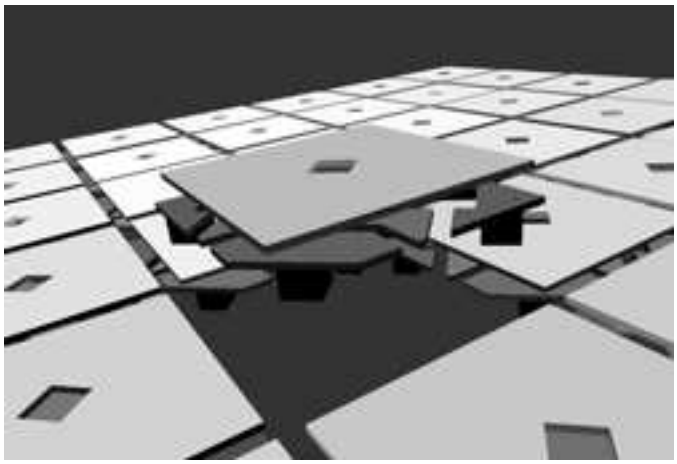

Figure 1.4: An array of DMDs used for switching light in digital displays.

Unlike optical switching techniques, where maintaining precise micromirror orientation is a big issue, precise tilt angles are guaranteed in DMDs. This stems from the fact that DMD operations do not require variable tilt angles. DMDs have only two positions: an on-position in which the pixel corresponding to the mirror appears bright, and an off-position in which the pixel corresponding to the mirror appears dark. These two positions are maintained using mechanical stoppers at each side of the mirror. A very important issue however is to minimize the voltage requirements. This is especially important in this case because each DMD forms only one pixel on a big screen that usually consists of millions of pixels.

The fast response of the micromirror and its ability to achieve large scanning angles by resonant electrostatic actuation makes it an appealing substitute for traditional scanning techniques. As a result, it has been successfully implemented in resonant optical microscanners [58]. To achieve large rotation angles while minimizing the voltage requirements, the micromirror is excited at its resonance frequency and then used to reflect and steer a laser beam along a surface. The laser beam is then reflected from the surface to be collected and analyzed through a photo detector. Resonant scanning mirrors are used in a variety of other applications, including laser printing, confocal microscopy, and scanning video displays.

Torsional micromirrors were also successfully introduced as a modulator and a reflector to

generate a pulse in a Q-switched fiber laser [59]. In such applications, the micromirror is excited at high frequency to modulate and produce a very high-power laser beam. It has been proven that this process is able to significantly reduce the size of the cavity and produce a laser pulse peek power that is 100 times higher than continuous pulse emission. Micromirrors have also proven useful in many other applications that include neural networks [60], phase modulating filters, optical computing [61], electrophotographic printers, and folded spectrum analyzers [62].

1.2.2 Review of Major Advances in the Literature

Statics and dynamics of torsional micromirrors

The analysis of the static behavior and the pull-in instability have occupied most of the literature available on torsional micromirrors. Various numerical and analytical techniques were introduced to investigate the pull-in phenomenon. A simple approach was introduced by Osterberg [63] for analyzing the static performance of a 1-DOF torsional micromirror. He used the parallel-plate approximation to estimate the electrostatic torque and an effective linear spring coefficient to estimate the mechanical stiffness. Although his model yielded rapid calculations his results showed 20% deviations from experimentally measured quantities. Hornbeck [64], on the other hand, developed an analytical expression for the electrostatic torque based on the solution of the Laplace equation between two semi-infinite tilted plates. Then he numerically solved for the mirror tilt angle at a given voltage and gradually increased the voltage until the pull-in point is reached. This numerical approach is extremely accurate, but requires successive numerical solutions of a complex nonlinear algebraic equation.

Degani et al.[65] studied the static pull-in characteristics of a torsional square-plate micromirror. Using a 1-DOF model consisting of a lumped mass attached to two torsional springs representing the suspension beams, he derived a polynomial algebraic equation for the pull-in

voltage and pull-in angle. This equation was then used to estimate the pull-in parameters of two microfabricated mirrors with two different suspension configurations. For both cases, a comparison between the pull-in parameters obtained experimentally and theoretically using the model showed less than 1% deviation.

Nemirovisky and Degani [66] developed an analytical methodology to find the pull-in parameters in electrostatic actuators. The model depends on the analytical expression of the actuator capacitance and the mechanical potential energy. Using this model, they investigated the effect of fringing field capacitance, parasitic capacitance, and trapped charges on the pull-in parameters. Several case studies, including a torsional micromirror, were easily analyzed using this analytical approach. Degani and Nemirovisky [67] used this analytical approach to develop a very accurate polynomial expression to calculate the pull-in parameters of a 1-DOF rectangular torsion-based actuator. The results of this analytical polynomial expression showed excellent agreement with a finite element/boundary element (FEM/BEM) simulations provided by MEMCAD4.8 Cosolve tool. Hah et al. [68] used the same approach to develop an analytical model for the pull-in parameters of a 1-DOF torsional micromirror and vertical comb-driven micromirrors. The analytical results were in excellent agreement with the experimental findings.

The influence of the electrode dimensions on the pull-in parameters of a torsional micromirror was studied by Zhang et al. [69, 70]. They developed a model of a 1-DOF torsional micromirror based on the parallel-plate capacitor approximation and used it to investigate the pull-in phenomenon. The numerical simulations were compared to experimental findings and the results were in good agreement.

Xiao et al. [71] proposed a design methodology for a 1-DOF torsional microactuator. The design approach is based on the analytical expressions for the pull-in voltage and pull-in angle. The scheme uses the pull-in angle, the maximum allowed operation voltage, and the width and length of the micromirror as inputs, and calculates the beam width, length, and depth, the gap distance, the electrode length, and the mirror natural frequency.

To increase the pull-in angle and extend the travel range of a 1-DOF torsional micromirror, Guardia et al. [72] proposed a methodology based on charge actuation. This methodology proved to be capable of almost doubling the rotation angle of the micromirror, but suffered significant degradation in performance due to the existence of parasitic charges. In addition, this technique showed a very steep decent to pull-in, which limits its practical applications.

Wetzel and Strozewski [73] were among the first to study the dynamic characteristics of a 1-DOF torsional micromirror. Treating the mirror as a lumped mass attached to two torsional springs representing the suspension beams, they developed a dynamical model of a micromirror used as a spatial light modulator. They numerically examined the dynamic response of the mirror and observed its transient and steady-state response. The numerical simulations were in good agreement with the experimental results.

Camon and Larnaudi [74] experimentally investigated the static and dynamic response of a 1-DOF torsional model of a micromirror. They studied the effect of electrode orientation on the static response of the mirror and found that, instead of using planar electrodes, one can vertically incline the electrodes at a certain angle and obtain significantly larger rotation angles for the same driving voltage. Experimentally, they were among the first to report a nonlinear softening behavior in the response. This softening behavior was more pronounced for higher voltages.

Sattler et al. [75] investigated the dynamic behavior of a 1-DOF torsional micromirror using both charge and voltage controlled analyses. They reported that the charge controlled analysis is not of a practical use since it shows a steep decent towards pull-in. They analyzed the transient dynamics of a micromirror under step voltage excitations and showed that, due to the effect of the mirror inertia, dynamic pull-in occurs at a voltage lower than that predicted by the static analysis.

Degani and Nemirovsky [76] were the first to model the pull-in parameters of a micractuator using a 2-DOF lumped-mass model. The effect of bending was included, and an analytical approach for the calculation of the pull-in parameters was introduced. The equations used

to determine the pull-in parameters were analytically derived utilizing the fact that the total energy of the actuator exhibits a maxima at pull-in. Two case studies were analyzed and the results were in excellent agreement with a finite difference and FEM/BEM simulations provided by MEMCAD4.8. Huang et al. [77] utilized this approach to study the static behavior of a 2-DOF torsional micromirror. They derived the equations governing the response of the mirror to a DC voltage and studied the effect of electrode size and position on the pull-in parameters. They found that the simulations are in good agreement with the experimental results.

Zhao et al. [78] considered the coupling effect between torsion and bending and developed an analytical model to study the dynamic characteristics of a 2-DOF torsional micromirror. They treated the mirror as a lumped mass attached to two springs. The springs represent the torsional and bending stiffnesses of the suspension beams. They numerically simulated the dynamic response of the mirror to step and pure AC voltage excitations. The numerical simulations were in good agreement with the results obtained using ANSYS.

Control of torsional micromirrors

For optical switching applications, the micromirror has to achieve the desired static configuration with enhanced transient dynamic characteristics. Towards that end, torsional micromirrors are often redesigned [79]. However, this approach can be costly, time consuming, and usually results in more complex devices. Consequently, the research has been directed towards various control techniques, which can be used to alter the input actuation signals to achieve the desired mirror response.

In general, the actuation signals can be controlled using either a closed-loop or an open-loop control technique. A well-designed closed-loop controller is generally more robust to errors in parameter estimates, does not require a very accurate model of the system, and can account for external disturbances, thus achieving a better and more stable response than the open-loop controllers. However, its application to systems at the micro scale is usually

very cumbersome and costly. Feedback measurements at the micro scale are very hard and require very accurate sensing techniques, especially because the signal-to-noise (SNR) ratio is very low. Even though the application of current sensing techniques at the laboratory level is hard but not impossible, their actual implementation on real systems at a large scale for manufacturing purposes is very costly and sometimes impossible using available technologies. For these reasons, a carefully designed open-loop control algorithm, such as input shaping, can be the best alternative.

Input shaping was not applied to torsional micromirrors. However, traditional shaping techniques were applied to a couple of systems at the microscale. In one demonstration, Borovic et al. [80] applied a variation of the ZV shaper to voltage commands used to excite a comb driven variable optical attenuator. The electrostatic field in their model is a linear function of the states. In this case, the device frequency is constant and traditional shaping techniques are expected to have excellent performance. One drawback of the work, however, is that the mathematical model and hence the shaped commands ignored the significant effects of higher modes, thereby resulting in some residual oscillations in the experiments.

In another demonstration, Popa et al. [81] developed a ZVD shaper for the input voltage applied to a thermal biomorph MEMS actuator. The shaper parameters were obtained using a simple discrete model. The shaper was then applied to a third-order Finite- Element Analysis (FEA) data used to model the system dynamics. The simulations showed excellent results when the shaper is applied to the discretized model, but some residual oscillations existed when the shaper was applied to the FEA model due to modeling errors and ignored nonlinearities.

Some feedback control algorithms were successfully applied at the laboratory level to enhance the transient dynamic characteristics of torsional micromirrors. Chiou et al. [82] proposed a control algorithm in which they divided the large-single electrode into multiple independent small electrodes. The small electrodes were then activated independently to achieve different voltage-angle relations. The advantage of the proposed technique is that, by switching

between different electrode patterns, one can achieve a quasilinear voltage-angle relation rather than the highly nonlinear voltage-angle relation resulting from a single electrode. Using this multiple electrostatic control configuration, they implemented a closed-loop fuzzy control algorithm capable of reducing the settling time by up to three times.

A closed-loop adaptive control technique was proposed by Liao et al. [83]. The proposed controller is capable of compensating for parameter variations and modeling uncertainties. To obtain feedback measurements, the authors proposed a differential capacitance approach in which the difference between the capacitance of the right and left electrode is used to measure the actual tilt angle of the mirror. The authors compared this controller to a traditional PID control technique and found that adaptive control realizes faster settling times and less tilt-angle overshoot.

Sane et al. [84] implemented a sliding-mode control algorithm with a first-order sliding function to a two-axis gimballed torsional micromirror. The proposed technique is implemented using a Position Sensing Diode (PSD) for feedback tilt-angle measurements. The robustness of the controller was analyzed and it was found that the controller is robust to variations in the mirror frequency and quality factor.

1.3 Dissertation Contributions

We divide the contributions of this dissertation into the following two major parts:

1. **Quay-side container cranes:**

    - Adapt input-shaping techniques to minimize payload oscillations on large quay-side container cranes. Unlike previous input-shaping controllers, which were based on a simple-pendulum model of the crane, the new technique is based on an accurate four-bar-mechanism model of the container crane and uses a nonlinear approximation of the model oscillation frequency.

- Develop a novel technique to calculate the shaper parameters used to generate an input command, which accounts for large hoisting operations with minimum residual oscillations. This approach uses a graphical representation of the phase plane that represents the response of the payload to a DS acceleration command. Our approach is more efficient than the ZVD shaper and can be extended to other LTV systems.
- Develop a hybrid controller to increase the robustness of input commands to errors in the estimated system parameters and to enable external disturbance rejection. The proposed controller augments the shaped commands with a nonlinear delayed-position feedback controller at the end of the transfer maneuver. This approach maximizes the controller effectiveness. The smooth shaped commands use the maximum crane capabilities to transfer the payload to the target point with minimum residual oscillations, and the feedback controller eliminates any remaining residual oscillations resulting from external disturbances and/or unmodeled dynamics.
- Design and build a 1:10 scale model of a 65-ton quay-side container crane. We use the experimental facility as a test bed to verify the theoretical models and to test the developed controllers.

2. **Torsional micromirrors:**

- Develop a comprehensive model of a torsional micromirror subjected to electric excitations.
- Develop a reduced-order model using a Galerkin expansion and verify it against experimental data. The model
  - accurately represents the static configuration of the mirror when subjected to DC excitations.
  - captures the significant dynamics of the mirror response when subjected to AC excitations.

- Investigate the accuracy of representing the statics and significant dynamics of the mirror using a 2-DOF lumped-mass model.
- Study the effects of the micromirror dimensions and electrode parameters on the pull-in instability and the natural frequencies of the mirror.
- Study the nonlinear dynamics of torsional micromirrors subjected to combined DC and resonant AC excitations. This analysis is necessary to provide better insight into the design of microscanners for faster operations and better performance.
- Analyze the effects of nonlinear interactions on the steady-state response of micromirrors and investigate possible techniques to avoid undesirable internal resonances.
- Develop a new technique for preshaping input commands to enhance the transient dynamic characteristics and performance of optical microswitches. This novel approach is the first to
  - effectively account for nonlinearities that cause voltage-frequency dependence.
  - account for damping effects and the energy of the significant higher modes.

  The new technique can be easily adapted to shape input commands applied to other nonlinear micro and macro systems. Using this approach, we were able to realize fast mirror switching operations with almost zero overshoot.

1.4 Dissertation Outline

The rest of the dissertation is organized as follows. In Chapter 2, we present a two-dimensional four-bar-mechanism model of a quay-side container crane. Using the geometry of the crane, we simplify the model into a constrained double-pendulum model that captures the significant dynamics of the system. We then use the simplified model to develop an approximate analytical expression for the model nonlinear frequency.

In Chapter 3, we use the analytical expression of the frequency to develop a SS input-shaping controller for fixed cable-length crane operations. We then develop a hybrid controller to increase the robustness of input commands to errors in the estimated system parameters and to enable external disturbance rejection. Finally, we develop a technique to design shaped commands that can account for large hoisting operations with minimum residual oscillations.

In Chapter 4, we present a brief description of a 1:10 scale model of a 65-ton quay-side container crane that we designed and built at Virginia Tech. We use the experimental setup to validate the theoretical models and implement the controllers using both of the open-loop input-shaping mode and the operator-in-the-loop closed-loop mode.

In Chapter 5, we develop a comprehensive model of a torsional micromirror . We first provide a general overview of the device, then we use Laplace's equation to derive an expression for the electrostatic energy. Using the resulting expression, we write the Lagrangian of the system and carry out a Galerkin expansion to develop a reduced-order model that captures the static and dynamic response of the mirror.

In Chapter 6, we define the linear eigenvalue problem and solve for the natural frequencies and associated mode shapes of the mirror. Based on the obtained results, we show that one can treat the mirror as a lumped mass attached to two springs representing the suspension beams.

In Chapter 7, we study the nonlinear dynamics of the micromirror. Using the method of multiple scales, we obtain a second-order nonlinear analytical approximation of the mirror steady-state response to combined DC and resonant AC excitations. In Chapter 8, we extend the nonlinear analysis to account for modal interactions.

In Chapter 9, we develop a new technique for preshaping input commands to enhance the transient dynamic characteristics and performance of optical microswitches. Finally, in Chapter 10, we present the conclusions and some recommendations for future work.

Chapter 2

Mathematical Modeling of Quay-Side Container Cranes

In this chapter, we develop a four-bar mechanism to model the actual hoisting mechanism of the quay-side container crane. This model is further simplified to a double-pendulum model with a kinematic constraint between the angles of both links of the pendulum. The simplified model is used for the purpose of controller design, however, numerical simulations are performed on the full model of the crane. For the purpose of comparison with input-shaping controllers developed using a simple-pendulum model, a nonlinear version of the traditional simple pendulum model is used.

2.1 Four-Bar-Mechanism Model

Figure 2.1 shows a two-dimensional side projection of a quay-side container crane. This four-bar mechanism is developed to model the actual dynamics of the crane. The container is grabbed using a spreader bar, which is then hoisted from the trolley by means of four cables, two of which are shown. The cables are spaced a distance d at the trolley and a

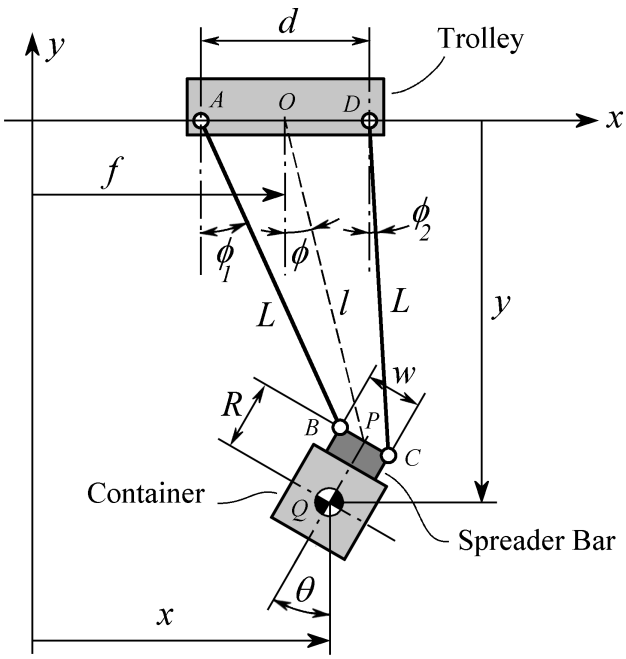

Figure 2.1: A schematic model of a container crane.

distance w at the spreader bar. The hoisting cables in the model are considered as rigid massless links with variable lengths. The specific equations of these holonomic constraints are

$$\Phi(\mathbf{q},t) = \begin{bmatrix} (x + R\sin\theta - \frac{1}{2}w\cos\theta - f + \frac{1}{2}d)^2 + (y - R\cos\theta - \frac{1}{2}w\sin\theta)^2 - L^2 \\ (x + R\sin\theta + \frac{1}{2}w\cos\theta - f - \frac{1}{2}d)^2 + (y - R\cos\theta + \frac{1}{2}w\sin\theta)^2 - L^2 \end{bmatrix} = 0 \tag{2.1}$$

where $\mathbf{q} = [x, y, \theta]^T$ is the generalized coordinate vector, which represents the three degrees of freedom of consideration.

Using Lagrange multipliers, one can write the set of differential-algebraic equations DAE's [85] as

$$\begin{bmatrix} \mathbf{M} & \Phi_{\mathbf{q}}^T \\ \Phi_{\mathbf{q}} & 0 \end{bmatrix} \begin{bmatrix} \ddot{\mathbf{q}} \\ \Lambda \end{bmatrix} = \begin{bmatrix} \mathbf{Q}^A \\ \Gamma \end{bmatrix} \tag{2.2}$$

where $\mathbf{M} = diag[m, m, m\bar{k}^2]$ is the inertia matrix, m is the mass of the payload and the

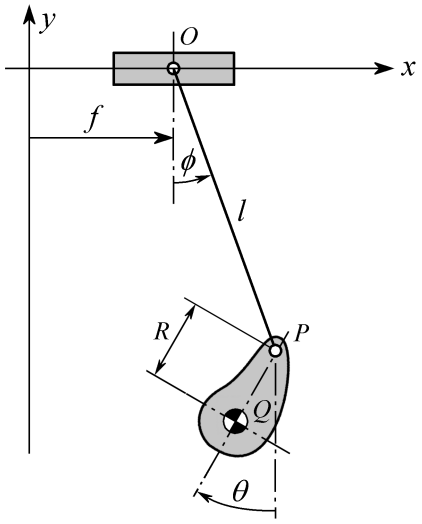

Figure 2.2: A schematic of a constrained double-pendulum model of a container crane.

spreader bar, $\bar{k}$ is the combined radius of gyration of the payload and spreader bar about point Q, $\mathbf{Q}^A = [0, -mg, 0]^T$ is the generalized applied force vector, Λ is the Lagrange multipliers vector, and

$$\Gamma = -(\Phi_{\mathbf{q}}\dot{\mathbf{q}})_{\mathbf{q}} - 2\Phi_{\mathbf{q}t}\dot{\mathbf{q}} - \Phi_{tt}, \qquad \Phi_{\mathbf{q}} = \frac{\partial \Phi}{\partial \mathbf{q}}, \qquad \Phi_{tt} = \frac{\partial^2 \Phi}{\partial t^2}, \qquad \Phi_{\mathbf{q}t} = \frac{\partial}{\partial t}(\frac{\partial \Phi}{\partial \mathbf{q}}). \tag{2.3}$$

2.2 Simplified Model

To better understand the dynamics of the system and to derive an analytical expression for the system frequency, which is essential to the controller design, we simplify the four-bar-mechanism model to a double-pendulum system with a variable length cable l, a fixed length link R, and a kinematic constraint relating the angles ϕ and θ, as shown in Fig. 2.2.

In Fig. 2.1, point O is the mid point between points A and D, and point P is the midpoint

between points B and C. The closing constraints of the loop $ABPO$ are

$$l\sin\phi - \frac{1}{2}w\cos\theta + \frac{1}{2}d = L\sin\phi_1 \tag{2.4}$$

$$l\cos\phi - \frac{1}{2}w\sin\theta = L\cos\phi_1 \tag{2.5}$$

Similarly, the closing constraints of the loop $ODCP$ can be written as

$$l\sin\phi + \frac{1}{2}w\cos\theta - \frac{1}{2}d = L\sin\phi_2 \tag{2.6}$$

$$l\cos\phi + \frac{1}{2}w\sin\theta = L\cos\phi_2 \tag{2.7}$$

Squaring and adding Equations (2.4) and (2.5) and squaring and adding Equations (2.6) and (2.7), we can eliminate L, ϕ_1, and ϕ_2 from the resulting equations and obtain the following relations:

$$\theta = -\phi + \arcsin\left(\frac{d}{w}\sin\phi\right) \tag{2.8}$$

$$l = \sqrt{L^2 - \frac{1}{4}(d^2 + w^2 - 2dw\cos\theta)} \tag{2.9}$$

Equation (2.8) represents the kinematic constraint between the angles ϕ and θ. The position vector to the center of mass of the payload of the constrained double pendulum is

$$\mathbf{r} = (f + l\sin\phi - R\sin\theta)\mathbf{i} - (l\cos\phi + R\cos\theta)\mathbf{j} \tag{2.10}$$

Using Equation (2.10), we write the kinetic and potential energies of the constrained double pendulum as

$$T = \frac{1}{2}ml^2\dot{\phi}^2 + \frac{1}{2}m(\bar{k}^2 + R^2)\dot{\theta}^2 + \frac{1}{2}m\dot{f}^2 - mRl\dot{\phi}\dot{\theta}\cos(\phi+\theta) + ml\dot{\phi}\dot{f}\cos\phi - mR\dot{\theta}\dot{f}\cos\theta \tag{2.11}$$

$$V = -mg(l\cos\phi + R\cos\theta) \tag{2.12}$$

Substituting the constraints (2.8) and (2.9) into Equations (2.11) and (2.12) results in the elimination of θ from the energy of the system. To derive the equation of motion that describes the time variation of ϕ, we use the Euler-Lagrange equation given by

$$\frac{\mathrm{d}}{\mathrm{dt}}\left(\frac{\partial\mathcal{L}}{\partial\dot{\phi}}\right) - \frac{\partial\mathcal{L}}{\partial\phi} = 0 \tag{2.13}$$

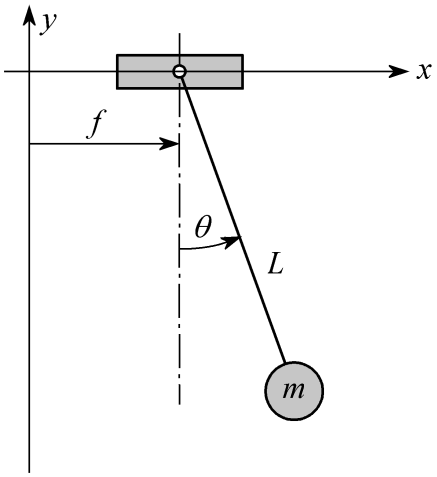

Figure 2.3: A schematic of a simple-pendulum model of a container crane.

where $\mathcal{L} = T - V$. Substituting Equations (2.11) and (2.12) into Equation (2.13) results in the full nonlinear equation of motion for the simplified system. Due to the lengthy expressions in the resulting equation, we only show expansions for special cases as necessary in the analysis.

2.3 Simple-Pendulum Model

An accurate model for gantry cranes is that of a simple pendulum attached to a moving cart, Fig. 2.3. The equation of motion for this model can be written as

$$\ddot{\theta} + \frac{2\dot{L}}{L}\dot{\theta} + \eta\cos\theta + \Omega_\circ^2 \sin\theta = 0 \tag{2.14}$$

where $\eta = \ddot{f}/L$ is the normalized trolley acceleration and $\Omega_\circ = \sqrt{g/L}$ is the linear frequency of the pendulum.

2.4 Nonlinear Frequency Approximation

To examine the effect of the frequency approximation on the system dynamics, we derive a nonlinear approximation of the frequency of the crane model for fixed-length operations.

We compare the numerical solution of the full equations of motion (2.2) to the analytical solution based on a linear and a nonlinear frequency approximation of the simplified model. To that end, we expand the equation of motion of the simplified model in a Taylor series up to cubic terms.

$$\ddot{\phi} + \omega_\circ^2 \phi + c_1 \phi^2 \ddot{\phi} + c_1 \phi \dot{\phi}^2 - c_2 \xi \phi^2 - c_3 \phi^3 + c_4 \xi = 0 \tag{2.15}$$

where

$$\begin{aligned}
\omega_\circ &= \sqrt{\frac{g({k_3}^2 + 2k_4 + {k_1}^2 k_3 R)}{k_3 \Gamma_0}}, \\
c_1 &= \frac{1}{\Gamma_0}\Bigg[\frac{4{k_4}^2}{{k_3}^2} + \frac{2k_1(3+2k_1)k_5 R}{k_3}, \\
&\quad + (k_1(1+k_1)^2 - 6k_2)k_3 R - 2(k_4 - 3k_1 k_2 R^2) + 6\bar{k}^2 k_1 k_2\Bigg], \\
c_2 &= \frac{k_3[k_3 + 6k_4 + R(6k_2 - {k_1}^3)]}{2\Gamma_0}, \\
c_3 &= g\frac{12k_4 - 24k_3^2 k_5 + k_3^2 + k_1^4 k_3 R - 24k_1 k_2 k_3 R}{6k_3 \Gamma_0}, \\
c_4 &= \frac{k_3(k_3 - k_1 R)}{\Gamma_0}, \\
\xi &= \frac{\ddot{f}}{k_3}, \\
\Gamma_0 &= \bar{k}^2 {k_1}^2 + (k_3 - k_1 R)^2.
\end{aligned}$$

and

$$\begin{aligned}
k_1 &= \frac{d-w}{w}, & k_2 &= \frac{d(d^2 - w^2)}{6w^3}, \\
k_3 &= \sqrt{L^2 - \frac{1}{4}(d-w)^2}, & k_4 &= \frac{dw}{8}, \\
k_5 &= \frac{dw(d^2 - 4L^2 + dw + w^2)}{24((d-w)^2 - 4L^2)^2}.
\end{aligned}$$

For simplicity, we expanded the equations around an equilibrium position defined by $\phi = 0$ rather than expanding around the actual equilibrium position corresponding to a given trolley acceleration ξ. This approximation holds for small oscillation angles, and will set an acceleration limit beyond which the accuracy of the analysis starts to deteriorate as we will show later in this section.

To find a nonlinear frequency approximation, we use the method of multiple scales [86]. First we scale Equation (2.15) by introducing a bookkeeping parameter ϵ, which is set to one at the end of this analysis, and scale ξ and θ at order ϵ; that is,

$$\phi = \epsilon\phi, \qquad \xi = \epsilon\xi. \tag{2.16}$$

Substituting the scaled parameters into Equation (2.15) yields

$$\ddot{\phi} + {\omega_\circ}^2\phi = -c_4\xi - \epsilon^2(c_1\phi^2\ddot{\phi} + c_1\phi\dot{\phi}^2 - c_2\xi\phi^2 + c_3\phi^3) \tag{2.17}$$

The time dependence is expanded in terms of the multiple time scales as follows

$$\begin{aligned} \frac{d}{dt} &= D_0 + \epsilon D_1 + \epsilon^2 D_2 + O(\epsilon^3) \\ \frac{d^2}{dt^2} &= D_0^2 + 2\epsilon D_0 D_1 + \epsilon^2 D_1^2 + 2\epsilon^2 D_0 D_2 + O(\epsilon^3) \end{aligned} \tag{2.18}$$

where $T_n = \epsilon^n t$ and $D_n = \frac{\partial}{\partial T_n}$. We then seek a solution in the form

$$\phi(T_0, T_1, T_2) = \phi_0(T_0, T_1, T_2) + \epsilon\phi_1(T_0, T_1, T_2) + \epsilon^2\phi_2(T_0, T_1, T_2) + O(\epsilon^3) \tag{2.19}$$

Substituting Equations (2.18) and (2.19) into Equation (2.17) and equating coefficients of like powers of ϵ, we obtain

$\underline{O(\epsilon):}$ $$D_0^2\phi_0 + \omega_\circ^2\phi_0 = -c_4\xi \tag{2.20a}$$

$\underline{O(\epsilon^2):}$ $$D_0^2\phi_1 + \omega_\circ^2\phi_1 = -2D_0D_1\phi_0 \tag{2.20b}$$

$\underline{O(\epsilon^3):}$ $$\begin{aligned} D_0^2\phi_2 + \omega_\circ^2\phi_2 = &- 2D_0D_1\phi_1 - 2D_0D_2\phi_0 - D_1^2\phi_0 - c_2\xi\phi_0^2 \\ &- c_1\phi_0(D_0\phi_0)^2 - c_1\phi_0^2D_0^2\phi_0 - c_3\phi_0^3 \end{aligned} \tag{2.20c}$$

The solution of Equation (2.20a) can be expressed as

$$\phi_0(T_0, T_1, T_2) = A(T_1, T_2)e^{i\omega_\circ T_0} - \frac{c_4\xi}{\omega_0^2} + cc \tag{2.21}$$

where A is a complex-valued function. Substituting Equation (2.21) into Equation (2.20b) and eliminating the terms that lead to secular terms, we obtain

$$D_1 A = 0 \qquad \Rightarrow \qquad A = A(T_2) \tag{2.22}$$

Now, substituting Equations (2.21) and (2.22) into Equation (2.20c) and eliminating the terms that lead to secular terms, we obtain the solvability condition

$$-2i\omega_\circ \frac{\partial A}{\partial T_2} + \frac{\xi^2 c_4}{\omega_\circ^2}(c_1 c_4 - 3\frac{c_3 c_4}{\omega_\circ^2} - 2c_2)A + (2\omega_\circ^2 c_1 - 3c_3)A^2\bar{A} = 0 \tag{2.23}$$

Introducing the polar transformation

$$A = \frac{1}{2}a(T_2)e^{i\beta(T_2)} \tag{2.24}$$

into Equation (2.23) and separating real and imaginary parts, we obtain the following two modulation equations:

$$\frac{\partial a}{\partial T_2} = 0 \tag{2.25}$$

$$\frac{\partial \beta}{\partial T_2} = \frac{\xi^2}{2\omega_\circ^3}\left[2c_2 c_4 - \frac{3c_3 c_4^2}{\omega_\circ^2} - c_1 c_4^2\right] - \frac{a^2}{4}\left[\frac{3c_3}{2\omega_\circ} + c_1\omega_\circ\right] \tag{2.26}$$

Solving Equations (2.25) and (2.26) we get the following approximate solution of Equation (2.17):

$$\phi = a\cos(\omega t + \beta_0) - \frac{c_4\xi}{\omega_\circ^2} \tag{2.27}$$

where

$$\omega = \omega_\circ\left[1 - a^2\left(\frac{3c_3}{8\omega_\circ^2} + \frac{c_1}{4}\right) + \frac{\xi^2}{2\omega_\circ^4}\left(\frac{-3c_3 c_4^2}{2\omega_\circ^2} + 2c_2 c_4 - c_1 c_4^2\right)\right] \tag{2.28}$$

is the nonlinear frequency approximation of the simplified model.

We tested the resulting approximation against a numerical solution of the full nonlinear equations of motion (2.2) for different values of ξ. The results showed that this approximation holds for $\xi \leq 0.1$ s^{-2}. As we explained earlier, this is due to linearizing around $\phi = 0$ rather

than the actual equilibrium position. This value sets a limit above which the nonlinear solution starts to deteriorate. However, container cranes normally operate at lower values of ξ ($0.015\ \mathrm{s}^{-2}$-$0.03\ \mathrm{s}^{-2}$). Figure 2.4 shows that the numerical integration and the multiple scale approximate solution closely match, while the linear frequency approximate solution quickly drifts away from the numerical solution as a result of the inaccurate frequency approximation.

Using Equation (2.14), we follow the same procedure to obtain the following nonlinear frequency approximation of the simple pendulum:

$$\Omega = \Omega_\circ \left(1 - \frac{a^2}{16} + \frac{\eta^2}{4\Omega_\circ^4}\right) \tag{2.29}$$

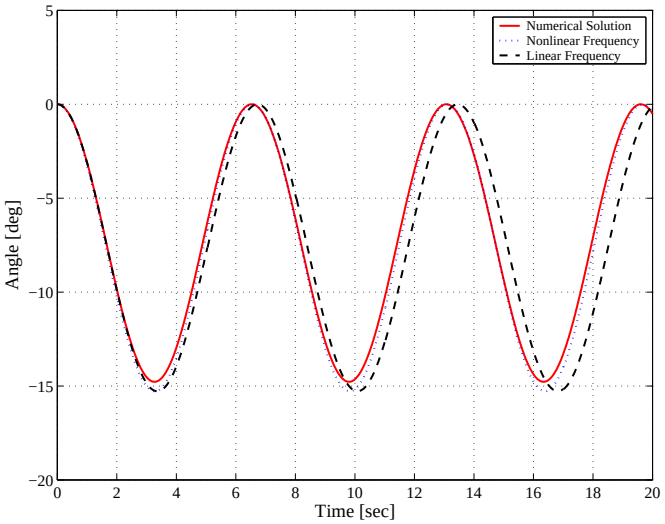

Figure 2.4: Payload sway angle for the constrained double-pendulum model of a container crane. The results are obtained for $L = 17.5\ m$, $R = 2.5\ m$, $\xi = 0.1\ s^{-2}$, $\phi_0 = 0$, and $\dot{\phi}_0 = 0$.

Chapter 3

Control of Container Cranes

In this chapter, we adapt input-shaping techniques to minimize payload oscillations on large quay-side container cranes. Unlike previous input-shaping controllers, which were based on a simple-pendulum model of the crane, the new techniques are based on an accurate four-bar-mechanism model of the container crane and use the nonlinear approximation of the model frequency obtained in Chapter 2. Furthermore, we develop a novel technique to calculate the shaper parameters used to generate input acceleration commands that can produce fast transfer operations which account for large hoisting and/or lowering maneuvers with minimal residual oscillations.

3.1 Constant Cable-Length Operations

A bang-off-bang or SS input-shaping controller, Fig. 3.1, works by generating an acceleration profile designed to cancel only its own oscillations. The controller is used to perform a transfer maneuver that produces zero residual oscillations.

For constant cable length L the response of the payload to an accelerating, decelerating, or coasting trolley (assuming the daping is very small) is illustrated in the phase portrait shown

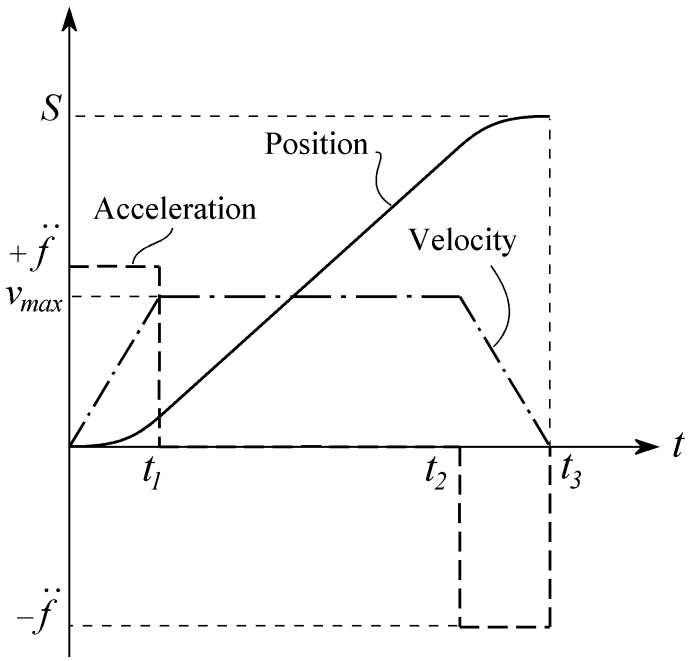

Figure 3.1: A schematic drawing showing the SS acceleration profile.

in Fig. 3.2. The figure shows that the solution is periodic with the payload exhibiting a limit cycle behavior. The center of the resulting limit cycle along the ϕ-axis is determined by the amplitude and sign of the associated fixed point.

Assuming that the cable length is known, the controller determines the magnitude of the constant acceleration $\ddot{f}$ and the switching times t_1, t_2, and t_3 to reach the target point with zero residual oscillations. First the trolley accelerates for the period of a half swing cycle $\Delta t_a = T_a/2$, where T_a is the period of the sway oscillation in the acceleration stage. The acceleration is then switched off for a period of time necessary to accomplish the load transfer, this period is called the coast stage. To bring the load into complete stop a negative acceleration is applied taking into account any known system inversion delays.

By design the coast time must be an odd multiple of half the period T_c of the sway oscillation in the coast stage. The coast time Δt_c depends also on the maximum acceleration achievable

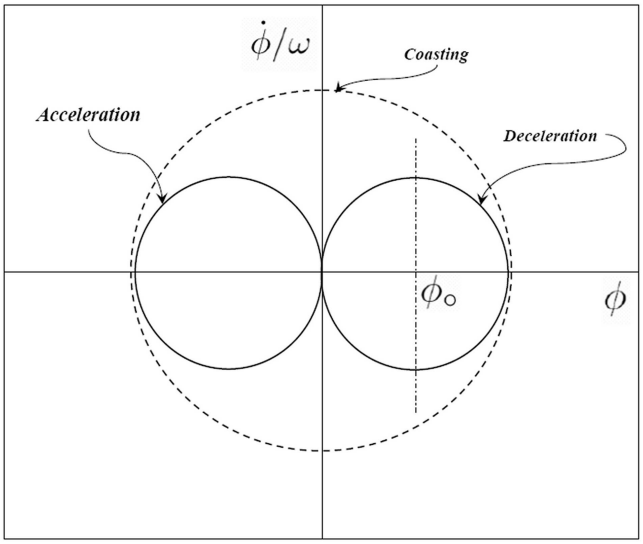

Figure 3.2: Phase portrait describing the dynamics of the crane payload for constant cable length.

by the trolley drives. Thus, we can define the coast time as

$$\Delta t_c = \frac{2n+1}{2} T_c, \qquad n = 0, 1, 2, 3, ... \tag{3.1}$$

where n is known as the number of coasting cycles. To account for motion inversion delays τ_s, n should be chosen such that Δt_c is greater than τ_s, in other words

$$n \geq \frac{1}{2}\left(\frac{2\tau_s}{T_c} - 1\right) \tag{3.2}$$

Here n is rounded up to the nearest integer including zero. The total distance traveled by the trolley in a full maneuver S derived from Fig. 3.1 is

$$S = \ddot{f}(\Delta t_a)^2 + \ddot{f}(\Delta t_a)(\Delta t_c) \tag{3.3}$$

Using the normalized acceleration $\xi = \ddot{f}/k_3$ and $\Delta t_a = T_a/2$ and substituting Equation (3.1) into Equation (3.3), the normalized travel distance $\delta = S/k_3$ is

$$\delta = \frac{1}{4}\xi T_a^2 + \frac{2n+1}{4}\xi T_a T_c \tag{3.4}$$

To adapt the input-shaping controller to the constrained double pendulum, the nonlinear frequency approximation, Equation (2.28), is used. Assuming zero initial conditions, we solve Equation (2.27) for a and then substitute back into Equation (2.28) to obtain

$$T_a = \frac{2\pi}{\omega_\circ}\left[1 + \frac{\xi^2}{2\omega_\circ^4}\left(2c_2c_4 - \frac{15c_3c_4^2}{4\omega_\circ^2} - \frac{3c_1c_4^2}{2}\right)\right]^{-1} \tag{3.5}$$

The period in the coast mode can be obtained by setting ξ equal to zero and substituting $a = -2c_4\xi/\omega_\circ^2$ into Equation (2.28). To find a which represents the amplitude of oscillation in the coast mode, we substitute $\omega t + \beta_0 = \pi$ into Equation (2.27) and obtain

$$T_c = \frac{2\pi}{\omega_\circ}\left[1 - \frac{4\xi^2c_4^2}{\omega_\circ^4}\left(\frac{c_1}{4} + \frac{3c_3}{8\omega_\circ^2}\right)\right]^{-1} \tag{3.6}$$

Now, we can summarize the controller algorithm as follows:

- Using the linear approximation for the coasting period T_c, determine the minimum number of coast cycles n.
- Solve Equation (3.4) for ξ and compare it with ξ_{max}, where ξ_{max} is the minimum of two values: the maximum acceleration that the trolley drives can provide and the maximum acceleration above which the nonlinear solution starts to deteriorate, which in this case is equal to ($0.1\ s^{-2}$). If ξ is greater than ξ_{max}, increment n up by one and recompute a new ξ.
- Compute the switching times t_1, t_2, and t_3 according to the following equations:

$$t_1 = \frac{T_a}{2}, \qquad t_2 = t_1 + \frac{2n+1}{2}T_c, \qquad t_3 = t_2 + t_1 \tag{3.7}$$

The generation of a shaped acceleration profile for a simple pendulum model follows the same procedure. However, in Equation (3.4), we substitute $\delta = \frac{S}{L}$ and use η rather than ξ. Assuming zero initial conditions, Equation (2.29) is used to calculate the nonlinear approximation of the periods in the bang and coat stages. The results are

$$T_a = \frac{2\pi}{\Omega_\circ}\left(1 + \frac{3\eta^2}{16\Omega_\circ^4}\right)^{-1} \tag{3.8}$$

$$T_c = \frac{2\pi}{\Omega_\circ}\left(1 - \frac{\eta^2}{4\Omega_\circ^4}\right)^{-1} \tag{3.9}$$

3.1.1 Numerical Simulations

To verify the accuracy of the obtained nonlinear frequency approximation of the simplified model, we generated shaped acceleration profiles based on the linear and nonlinear frequency approximations of the constrained double-pendulum model and applied them to the simplified model. Figure 3.3 (a) shows the shaped acceleration profiles for the linear and nonlinear cases. Figure 3.3 (b) illustrates that the magnitude of the residual oscillations associated with the linearly shaped acceleration profile are approximately 10 cm, while those associated with the nonlinearly-shaped profile are almost equal to zero. The simulations are based on typical dimensions of a 65-ton quay-side container crane: $R = 2.5\ m$, $d = 2.825\ m$, $w = 1.4125\ m$, and $S = 50\ m$. To generate the shaped profiles we also assume that n=1 ($T_c \leq \tau_s \leq 2T_c$).

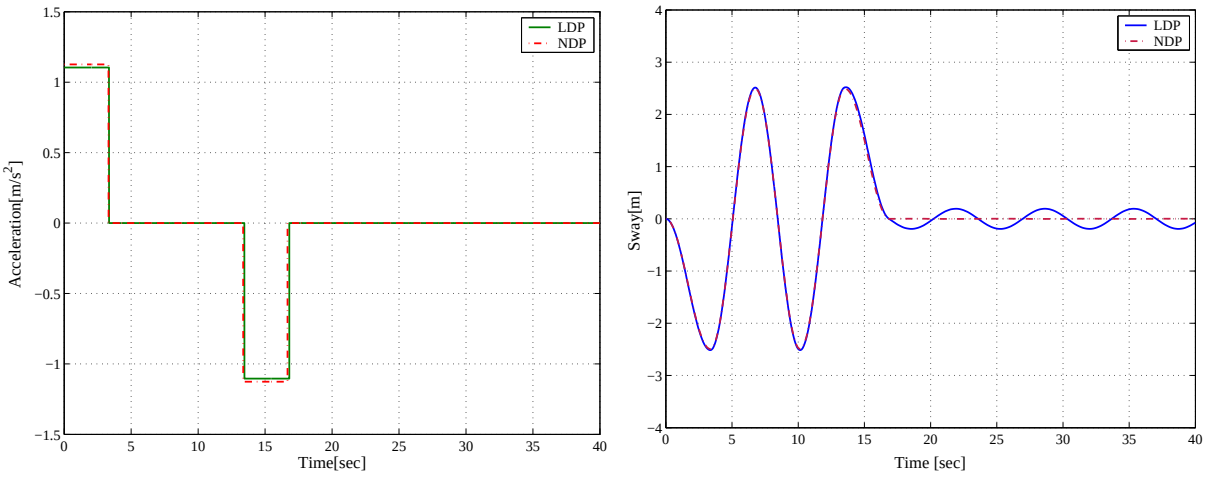

(a) Shaped operator commands.

(b) Payload sway.

Figure 3.3: Sway response of a constrained double pendulum model of a container crane to shaped operator commands. Results are obtained for $L = 17.5\ m$. LDP refers to linear frequency approximation of the double pendulum, and NDP refers to a nonlinear frequency approximation of the double pendulum.

We generate three acceleration profiles to drive the payload a distance of 50 m for a constant cable-length maneuver ($L = 17.5\ m$). The shaped acceleration profiles are based on the nonlinear frequency approximation of a simple pendulum and the linear and nonlinear frequency approximations of the simplified model. The results shown in Fig. 3.4 demonstrate that the shaped profile based on a simple pendulum does not reduce the residual oscillations. On the contrary, this shaped profile amplifies the residual oscillations to magnitudes that are even larger than the transient oscillations. On the other hand, the acceleration profiles based on the linear and nonlinear frequency approximations of the simplified model reduce the residual oscillations significantly. Furthermore, the nonlinearly shaped acceleration profile results in almost zero residual oscillations. This result has critical implications. Besides the fact that a simple pendulum model can not be used to model a quay-side container crane, the results demonstrate that the simplified model is a very accurate representation of the four-bar-mechanism model. This is obvious from the fact that, even at large trolley accelerations, a nonlinear approximation of the simplified model frequency results in almost zero residual oscillations on the full model.

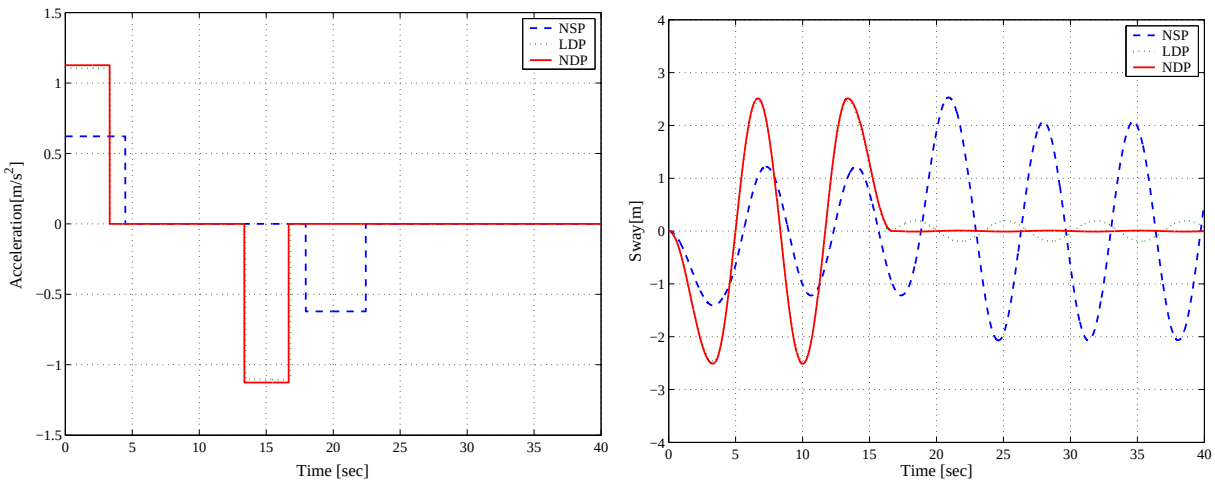

(a) Shaped operator commands.

(b) Payload sway.

Figure 3.4: Sway response of the full model of the container crane to shaped operator commands. Results are obtained for $L = 17.5\ m$. NSP refers to a nonlinear frequency approximation of a simple pendulum.

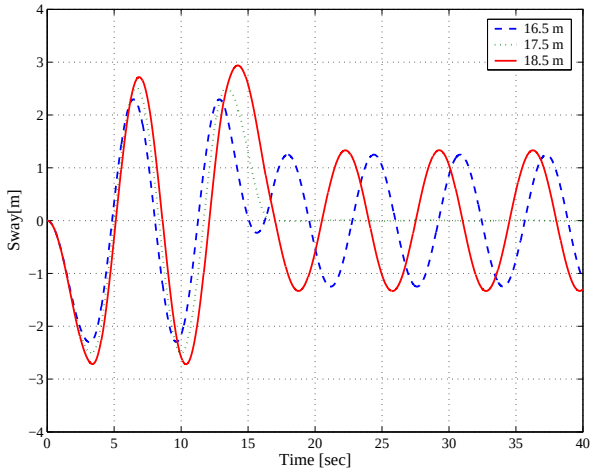

Figure 3.5: Sensitivity of the SS input-shaping controller to variations in the cable length: Sway response of the full model of the container crane to the shaped operator commands shown in Fig. 3.4(a).

Figure 3.5 demonstrates the sensitivity of the input-shaping controller to changes in the system parameters. The nonlinearly shaped acceleration profile shown in Figure 3.4 (a) is applied to the full model while varying the length of the hoisting cables. Simulations show that a change of 1.0 m in the cables length causes significant degradation in the controller performance.

3.2 Delayed-Position Feedback

To overcome the problem of the input-shaping controller sensitivity and to eliminate the residual oscillations, we apply a delayed-position feedback controller at the end of the transfer maneuver. The choice of delayed-position feedback controller is based on its ability to handle systems with inherent time delays. The controller can incorporate these delays in its parametric delay. Moreover, this controller was proven to have better performance than linear feedback and optimal controllers [47].

A number of factors were considered for applying a feedback controller only at the end of the

transfer maneuver. A significant factor is reducing the power required to perform a transfer maneuver with minimal residual oscillations. This stems from the fact that, for large sway angles, feedback control systems may require input accelerations that are beyond the normal operating accelerations, which may overload the trolley motors during the acceleration and deceleration stages. When applied at the end of a transfer maneuver performed using a shaped acceleration profile, feedback controllers require lower accelerations. This is due to the fact that a well-designed input-shaping controller is expected to produce significant reduction in the residual payload oscillations. Unlike feedback controllers, shaped commands can be designed to use the maximum crane capabilities and therefore result in faster operations. Moreover, feedback controllers produce continuously changing acceleration profiles, which affects the crane operator performance and comfort. Therefore, applying an efficient feedback controller only at the end of the transfer maneuver for a very short period of time eliminates excessive trolley motion. Thus maintaining comfortable working conditions for the crane operator.

The delayed-position feedback controller creates damping in the system by adding a delayed feedback component to the operator commands to the trolley drives. This component is proportional to the swing angle of the hoist line. The controller takes the following general form:

$$f = f_\circ + \hat{k} \sin \phi_{\tau_d} \tag{3.10}$$

where $\hat{k}$ is the feedback gain, τ_d is the delay time, $f_\circ$ is the operator input, and $\phi_{\tau_d} = \phi(t-\tau_d)$. To study the linear stability of the controller and to make a proper choice of the gain-delay combination, we substitute Equation (3.10) into Equation (2.15) and add a linear damping term to account for the damping in the system. Assuming that the operator input is slowly varying and keeping only linear terms yields

$$\ddot{\phi} + \omega_\circ^2 \phi + 2\mu\dot{\phi} + \frac{\hat{k}}{k_3}(\ddot{\phi}_{\tau_d} + 2\mu\dot{\phi}_{\tau_d}) = 0 \tag{3.11}$$

where μ is a linear damping coefficient. Now we seek an exponentially damped solution of

Equation (3.11) in the form

$$\phi = ce^{\sigma t}\cos(\omega t + \psi) \tag{3.12}$$

where c, σ, ω, and ψ are real constants. Substituting Equation (3.12) into Equation (3.11) and setting each of the coefficients of $\cos(\omega t+\psi)$ and $\sin(\omega t+\psi)$ equal to zero independently, we obtain the following two equations:

$$K(\sigma^2 + 2\mu\sigma - \omega^2)\sin(\omega\tau_d) - 2K\omega(\mu+\sigma)\cos(\omega\tau_d) - 2\omega(\sigma+\mu)e^{\sigma\tau_d} = 0 \tag{3.13}$$

$$K(\sigma^2 + 2\mu\sigma - \omega^2)\cos(\omega\tau_d) + 2K\omega(\mu+\sigma)\sin(\omega\tau_d) + (\sigma^2 + 2\mu\sigma - \omega^2 + \omega_\circ^2)e^{\sigma\tau_d} = 0 \tag{3.14}$$

where $\hat{k}/k_3 = K$. The stability of the system depends on the value of the parameter σ. The system is asymptotically stable for $\sigma < 0$ and unstable for $\sigma > 0$. To determine the boundaries of linear stability and instability we set σ equals to zero in Equations (3.13) and (3.14) and obtain

$$K\omega^2\sin(\omega\tau_d) + 2K\mu\cos(\omega\tau_d) + 2\mu\omega = 0 \tag{3.15}$$

$$2K\omega\mu\sin(\omega\tau_d) - \omega^2(1 + K\cos(\omega\tau_d)) + \omega_\circ^2 = 0 \tag{3.16}$$

Equations (3.15) and (3.16) can be normalized by dividing them by $\omega_\circ^2$, and setting the time delay τ_d proportional to the linear period of oscillation $T = 2\pi/\omega_\circ$. This yields

$$K\lambda^2\sin(2\pi\lambda\gamma) + 2K\nu\lambda\cos(2\pi\lambda\gamma) + 2\nu\lambda = 0 \tag{3.17}$$

$$2K\nu\lambda\sin(2\pi\lambda\gamma) - \lambda^2(1 + K\cos(2\pi\lambda\gamma)) + 1 = 0 \tag{3.18}$$

where $\lambda = \omega/\omega_\circ$, $\gamma = \tau_d/T$, and $\nu = \mu/\omega_\circ$. Manipulating Equations (3.17) and (3.18), we determine K and γ as functions of λ; the result is

$$K(\lambda) = -\frac{\sqrt{4\nu^2 + \lambda^2(\lambda^2 + 4\nu^2 - 1)^2}}{\lambda(\lambda^2 + 4\nu^2)} \tag{3.19}$$

$$\gamma(\lambda) = \frac{1}{2\pi\lambda}\left[\arctan\frac{2\nu}{\lambda(\lambda^2 + 4\nu^2 - 1)} + j\pi\right] \qquad j = 0, 1, 2, ... \tag{3.20}$$

The stability boundaries are determined by varying λ in Equations (3.19) and (3.20) and solving for K and γ. Figure 3.6 shows the stable and the unstable regions as predicted by the

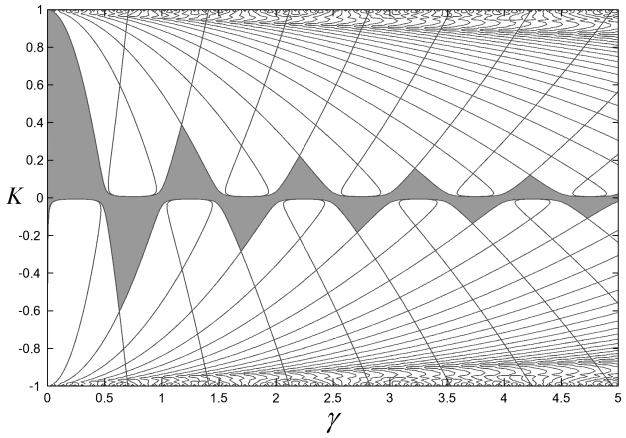

Figure 3.6: A stability plot of the delayed position-feedback controller for a relative damping $\nu = 0.0033$. The shaded areas represent the pockets of stability.

linear theory. Any gain-delay combination that lies inside the shaded areas of Fig. 3.6 leads to an asymptotically stable response. It is worth mentioning that there is infinite number of stability pockets, which decrease in size as the time delay of the controller τ_d increases. To determine the magnitude σ of the damping factor resulting from each gain-delay combination, we vary τ_d and K in Equation (3.13) and (3.14) and calculate σ. Figure 3.7 shows a contour plot for σ in the first pocket of stability.

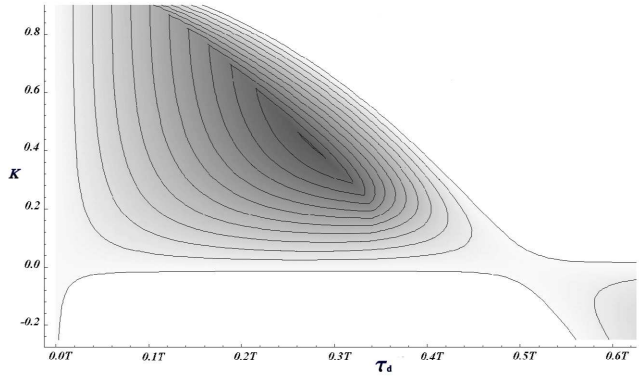

Figure 3.7: A contour plot of the damping as a function of the gain K and the delay τ_d, where τ_d is given in terms of the natural period of the uncontrolled system. The darker the areas are the higher the damping is.

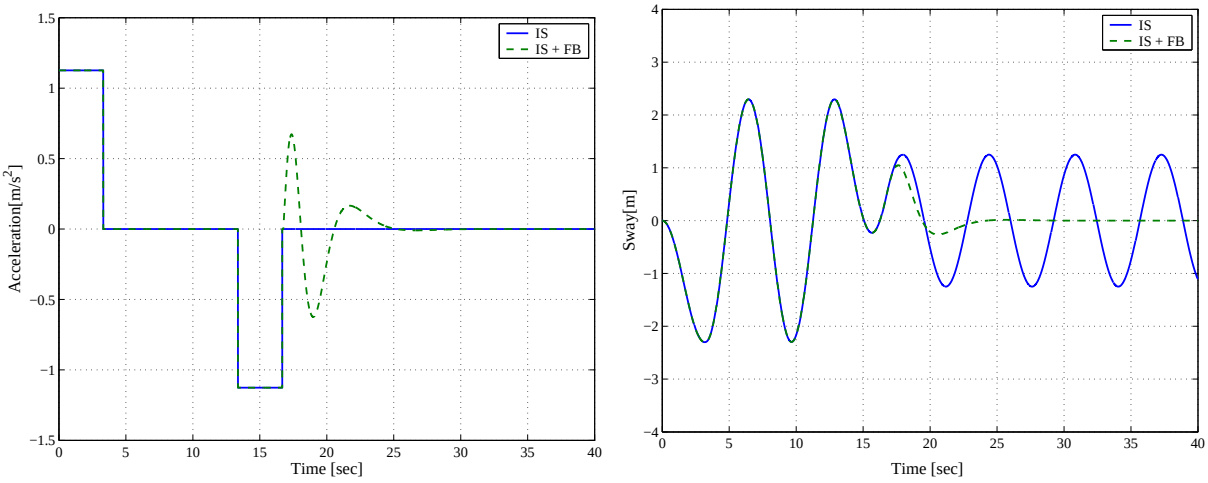

(a) Input acceleration profile.

(b) Payload sway.

Figure 3.8: Sway response of the full model of the container crane with input-shaping (IS) and combination of IS and feedback (FB) controllers. Results are obtained for $L = 16.5\ m$.

To demonstrate the performance of the hybrid controller, a shaped acceleration profile based on the nonlinear frequency approximation of the simplified model designed for a 17.5 m cable is applied to transfer a container positioned 16.5 m below the trolley a distance of 50 m. Figure 3.8 shows that the shaped command alone results in a residual sway of approximately 1.25 m, while a combination of input shaping and delayed-position feedback suppresses the residual sway to a magnitude less than 0.05 m within 4.5 s of the end of the transfer maneuver. The controller's gain-delay combination used in the simulations is $K = 0.4$ and $\tau_d = 0.28\ T$.

3.3 Variable-Length Operations

To better understand the dynamics of the system for operations that include hoisting, we linearize the equations of motion of the simplified model and obtain the following equation:

$$\ddot{\phi} + 2\mu(t)\dot{\phi} + \omega_\circ^2(t)\phi + \frac{\mu}{2\dot{L}}\ddot{f} = 0 \tag{3.21}$$

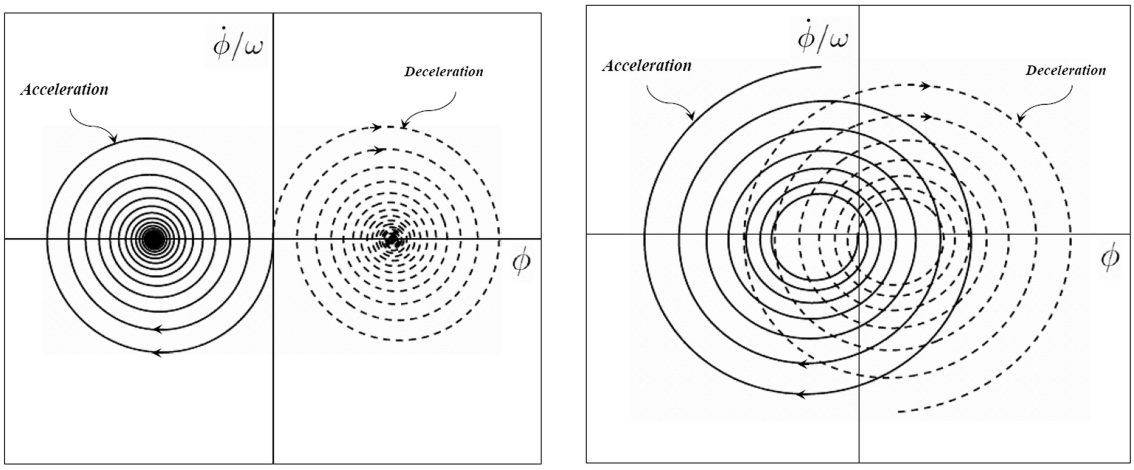

(a) $\dot{L} > 0$ (b) $\dot{L} < 0$

Figure 3.9: Phase portraits describing the dynamics of the crane payload.

where

$$\begin{aligned} \omega_\circ(t) &= \sqrt{\frac{g(L+\alpha^2 R) - \alpha\frac{dR\ddot{L}}{w}}{L^2 - 2\alpha RL + \alpha^2(\bar{k}^2 + R^2)}} \\ \mu(t) &= \frac{\dot{L}(L-\alpha R)}{L^2 - 2\alpha RL + \alpha^2(\bar{k}^2 + R^2)} \\ \alpha &= \frac{d-w}{w} \end{aligned} \tag{3.22}$$

In the above linear approximation, we assume that $l \approx L$. This assumption is justified, because, for small angles of oscillation, it yields less than 0.5% error in calculating the length l based on typical values of d, w, and L for container cranes.

Analyzing the dynamics involved in Equation (3.21) forms the basis for designing an effective input-shaping controller for maneuvers that involve large hoisting operations. First, we find the equilibrium solution of Equation (3.21) by letting $\dot{\phi} = \ddot{\phi} = 0$ and obtaining

$$\phi_L = -\frac{L - \alpha R}{g(L+\alpha^2 R) - \alpha\frac{dR\ddot{L}}{w}}\ddot{f} \tag{3.23}$$

For constant cable length and trolley acceleration, ϕ_L is constant and the dynamics of the payload is given in Fig. **??** (assuming the damping is very small). However, for operations

that include hoisting, the dynamic behavior of the payload is qualitatively different. The variation of L causes the equilibrium solution described by Equation (3.23) to vary along the ϕ-axis. If L increases, the magnitude of ϕ_L increases and vise versa. This equilibrium solution is known as a non-stationary fixed point. Moreover, in the case of hoisting $\dot{L} \neq 0$ and hence the term including $\dot{\phi}$ in Equation (3.21) is no longer equal to zero. This term acts as a damping term with the sign of $\dot{L}$ determining the type of damping. Therefore, the equilibrium solution of (3.21) is no longer a marginally stable center. The stability of this equilibrium solution is now determined by the sign of $\dot{L}$. For a positive $\dot{L}$, the damping is positive and the equilibrium solution is a stable focus (sink). On the other hand, for a negative $\dot{L}$, the damping is negative and the equilibrium solution is an unstable focus (source). The qualitative dynamic behavior of the payload around the non-stationary equilibrium solution is illustrated in Fig. 3.9 (b) and (c).

To design an effective input-shaping controller for variable-length operations, we use a variation of the SS acceleration profile. This profile is shown in Fig. 3.10 and is called a DS acceleration profile. Unlike the SS shaper, a well- designed DS shaper results in zero oscillations at the end of both of the acceleration and deceleration stages. This is very important since it minimizes the effects of damping and nonlinearities on the payload dynamics [87].

In a DS profile, the trolley accelerates at a constant rate a_{max} for time t_{a_1}, after which the trolley coasts at a constant velocity until time t_{c_1}. The trolley then accelerates again with the same acceleration until time t_{a_2} where the acceleration phase is concluded. Afterwards, the trolley coasts until time T, then decelerates in two steps similar to the acceleration stage. A shaped DS acceleration profile similar to the one shown in Fig. 3.10 uses the maximum system capabilities to achieve the required transfer maneuver with minimal transient and residual oscillations. To generate the required profile, the controller calculates the switching times such that the payload dynamics follow the phase portrait shown in Fig. 3.11. Ideally, this phase portrait drives the dynamics of the payload to end at the equilibrium point at the center of the phase portrait rather than a limit cycle around it.

To determine the switching times for this phase portrait, the trolley acceleration profile must satisfy two sets of constraints. The first set includes the dynamic constraints that involve the amplitudes of the response at the beginning and at the end of each acceleration step and the physical constraints on the crane motors.

To derive the dynamic constraints, we obtain an approximate homogeneous solution of Equation (3.21). For typical crane operations, $\dot{L}$ and $\ddot{L}$ are small quantities, hence $\mu(t)$ and $\omega_\circ(t)$ are slowly varying when compared to the fast dynamics of ϕ. As a result, one can use the WKB theorem [86] to obtain an approximate solution of Equation (3.21). Towards that end, we introduce the transformation

$$\phi(t) = P(t)U(t) \tag{3.24}$$

into the homogeneous part of Equation (3.21) and obtain

$$\ddot{P}U + 2\dot{U}\dot{P} + \ddot{U}P + 2\mu(t)(\dot{P}U + \dot{U}P) + \omega_\circ^2(t)PU = 0 \tag{3.25}$$

We set the coefficients of $\dot{U}$ equal to zero to obtain

$$\dot{P} = -\mu(t)P \Rightarrow P = c_1 e^{-\int \mu(t)dt} \tag{3.26}$$

Substituting Equation (3.26) back into Equation (3.25), yields

$$\ddot{U} + q(t)U(t) = 0 \tag{3.27}$$

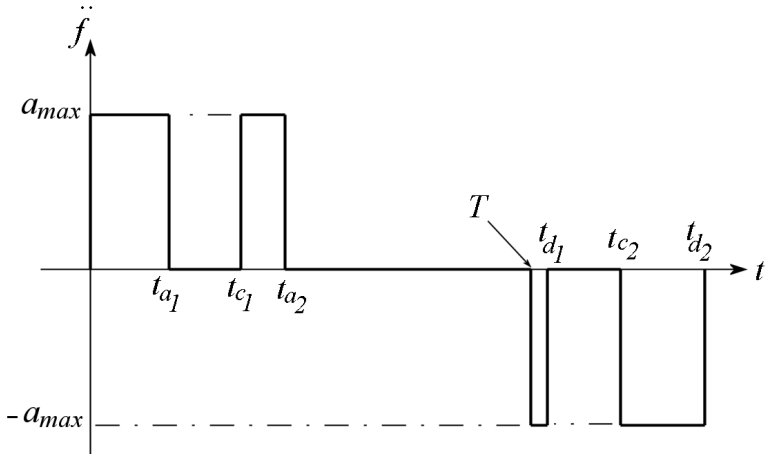

Figure 3.10: Typical acceleration profile of a DS input-shaping controller.

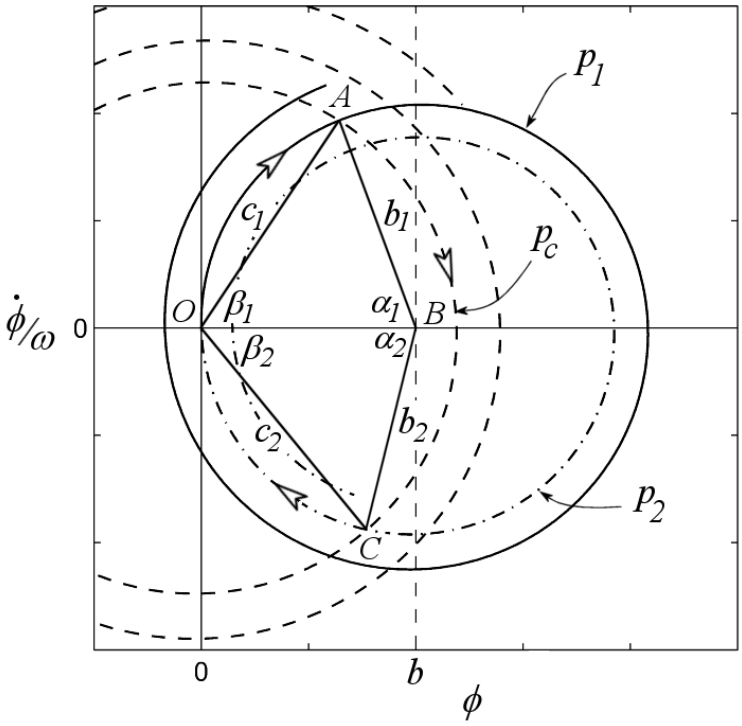

Figure 3.11: Graphical representation of the controller phase portrait.

where

$$q(t) = \omega_\circ^2(t) - \mu^2(t) - \dot{\mu}(t)$$

Since $q(t)$ is slowly varying, we can introduce the transformation $\tau = \epsilon t$ in Equation (3.27), here ϵ is a small dimensionless parameter. This yields

$$\frac{d^2U}{d\tau^2} + \lambda^2 q(\tau) U = 0 \tag{3.28}$$

where $\lambda = \epsilon^{-1}$. Using the WBK theorem and the fact that $\lambda \int \sqrt{q}\, d\tau = \epsilon\lambda \int \sqrt{q}\, dt = \int \sqrt{q}\, dt$, the solution of Equation (3.28) can be written as

$$U \approx q^{-1/4}\left\{e_1 \cos\left[\int \sqrt{q}\, dt\right] + e_2 \sin\left[\int \sqrt{q}\, dt\right]\right\} \tag{3.29}$$

where e_1 and e_2 are constants obtained using the initial conditions. Using Equation (3.24) and (3.26), we can write the approximate solution of Equation (3.21) as

$$\phi \approx q^{-1/4} e^{-\int \mu(t)\ dt}\left\{e_1 \cos\left[\int \sqrt{q}\, dt\right] + e_2 \sin\left[\int \sqrt{q}\, dt\right]\right\} \tag{3.30}$$

For typical hoist speeds and accelerations of quay-side cranes ($\dot{L} \leq 2\ m/s, \ddot{L} \leq 0.5\ m/s^2$), our simulations reveal that the approximate solution leads to very acceptable results. The controller design however does not use the total approximate solution, we only use the fact that the amplitude of the response is exponentially damped.

Over each acceleration or coasting step, we use an average value for the damping μ. Therefore, the amplitude of the response say χ at any time t can be related to the initial amplitude say χ_i at time t_i by

$$\chi = \chi_i e^{\mu_{avg}(t-t_i)} \tag{3.31}$$

where

$$\mu_{avg} = \frac{1}{t-t_i} \int_{t_i}^{t} \mu(\tau)\ d\tau \tag{3.32}$$

where τ is a dummy variable. In the first acceleration step, the trolley accelerates so that the new equilibrium solution is at point B, which is assumed to be stationary for typical crane parameters and operating range of the hoisting cable. The response then follows the path p_1 through a phase angle α_1 to point A. The amplitude of the response at that point is

$$b_1 = be^{\mu_{avg} t_{a_1}} \tag{3.33}$$

The second acceleration step t_{c_1} to t_{a_2} is designed to force the response of the system to home at the origin of the phase portrait at the end of this acceleration step. The system response follows the path p_2 through the phase angle α_2. Going back in time, the starting amplitude of oscillation of the second acceleration step at point C has to satisfy

$$b_2 = be^{-\mu_{avg}(t_{a_2}-t_{c_1})} \tag{3.34}$$

To guarantee the continuity of the response, points A and C are required to fall on the same coasting path p_c. This can be represented by the following relation:

$$c_2 = c_1 e^{\mu_{avg}(t_{c_1}-t_{a_1})} \tag{3.35}$$

A fourth dynamic constraint is derived from the physical constraints on the velocity and acceleration achievable by the trolley motors. This constraint can be enforced by restricting

the acceleration time so that the trolley velocity does not exceed the maximum achievable velocity by the trolley motors.

$$v_{max} = a_{max}(t_{a_1} + t_{a_2} - t_{c_1}) \tag{3.36}$$

The second set of constraints are geometric constraints which are derived directly from the graphical representation of the controller phase portrait, Fig. 3.11. Graphically, the coasting phase is split into two consecutive stages: β_1 and β_2. The first phase ends when the response crosses the zero velocity axis on the phase portrait at time t_o. Considering the upper triangle OAB, and using the geometric laws of sines and cosines, the following geometric constraints are obtained:

$$c_1^2 = b^2 + b_1^2 - 2bb_1\cos\alpha_1 \tag{3.37}$$

$$c_1 = b_1\frac{\sin\alpha_1}{\sin\beta_1} \tag{3.38}$$

Similarly, considering the lower triangle OCB, two other geometric constraints are derived

$$c_2^2 = b^2 + b_2^2 - 2bb_2\cos\alpha_2 \tag{3.39}$$

$$c_2 = b_2\frac{\sin\alpha_2}{\sin\beta_2} \tag{3.40}$$

The phase angles of the controlled performance in the acceleration and coasting phases can be related to the system frequencies and switching times by the following equations

$$\alpha_1 = \int_0^{t_{a_1}} \omega_a dt \tag{3.41}$$

$$\alpha_2 = \int_{t_{c_1}}^{t_{a_2}} \omega_a dt \tag{3.42}$$

$$\beta_1 = \int_{t_{a_1}}^{t_o} \omega_c dt \tag{3.43}$$

$$\beta_2 = \int_{t_o}^{t_{c_1}} \omega_c dt \tag{3.44}$$

where ω_a and ω_c are the frequency of payload oscillations in the accelerations and coasting stages, respectively. When a linear frequency approximation is used, $\omega_a = \omega_c = \omega_\circ$.

To reduce the above eight constraint equations into four equations in terms of only the unknown switching times t_{a_1}, t_o, t_{c_1}, and t_{a_2}, we substitute Equations (3.33), (3.38), (3.41), and (3.43) into Equation (3.37) and obtain

$$e^{(2\int_0^{t_{a_1}}\mu dt)}\frac{\sin^2(\int_0^{t_{a_1}}\omega_a dt)}{\sin^2(\int_{t_{a_1}}^{t_o}\omega_c dt)} = 1 + e^{(2\int_0^{t_{a_1}}\mu dt)} - 2e^{(\int_0^{t_{a_1}}\mu dt)}\cos\left(\int_0^{t_{a_1}}\omega_a dt\right) \tag{3.45}$$

Similarly, we substitute Equations (3.34), (3.40), (3.42), and (3.44) into Equation (3.39), and obtain

$$e^{(-2\int_{t_{c_1}}^{t_{a_1}}\mu dt)}\frac{\sin^2(\int_{t_{c_1}}^{t_{a_2}}\omega_a dt)}{\sin^2(\int_{t_o}^{t_{c_1}}\omega_c dt)} = 1 + e^{(-2\int_{t_{c_1}}^{t_{a_1}}\mu dt)} - 2e^{(-\int_{t_{c_1}}^{t_{a_1}}\mu dt)}\cos\left(\int_{t_{c_1}}^{t_{a_2}}\omega_a dt\right) \tag{3.46}$$

We also substitute Equations (3.33), (3.38), (3.34), (3.40), and (3.41)-(3.44) into Equation (3.35) and obtain

$$e^{(-\int_0^{t_{a_1}}\mu dt)}\frac{\sin(\int_{t_{c_1}}^{t_{a_2}}\omega_a dt)}{\sin(\int_{t_o}^{t_{c_1}}\omega_c dt)} = \frac{\sin(\int_0^{t_{a_1}}\omega_a dt)}{\sin(\int_{t_{a_1}}^{t_o}\omega_c dt)} \tag{3.47}$$

The final four constraint equations (3.36) and (3.45)-(3.47) are then numerically solved for the switching times of the controller. The same approach is used for both the acceleration and deceleration stages. The trolley coasting time between the acceleration and deceleration stages T is determined by the total travel distance of the trolley.

3.3.1 Numerical Simulations

Using the linear frequency approximation Equation (3.22), a shaped double-step acceleration profile is generated for a fixed cable-length transfer operation as shown in Fig 3.12(a). The resulting profile is then applied to the full equations of motion (2.2), and the phase portrait of the payload response is shown in Fig. 3.12(b). It is clear that even for large trolley input acceleration ($a = 1\ m/s^2$), the shaped acceleration produced a payload response with almost zero residual oscillations.

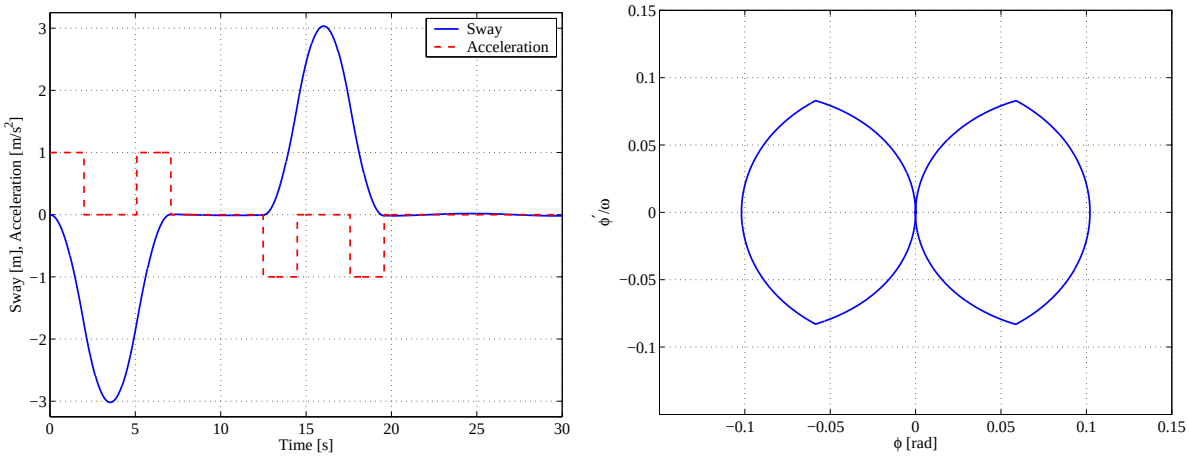

(a) Payload sway and trolley acceleration

(b) Phase portrait of the system response

Figure 3.12: Sway response of a container crane to shaped operator commands: $L = 32.5\ m$ and $S = 50\ m$.

This point is also illustrated in Fig. 3.13 where we show a comparison between the performance of the DS controller using the linear and nonlinear frequency approximations. The amplitude of the residual oscillations obtained with a linear frequency approximation is larger than that obtained with a nonlinear approximation. However, in contrast with the SS controller where the difference is large and cannot be tolerated, the difference here is very small and can be neglected. This is due to the fact that using the DS profile, the period over which large oscillations occur is so short that frequency approximation do not produce significant deviation from the desired system dynamics.

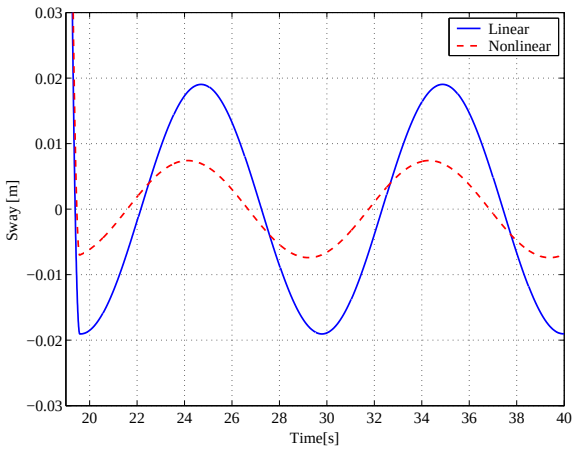

Figure 3.13: Residual oscillations of the payload resulting from a DS input-shaping controller: $L = 32.5\ m$ and $S = 50\ m$.

To illustrate the effectiveness of the new approach for variable cable-length operations, three simulations are presented to demonstrate a hoisting up, lowering, and a combined hoisting up and lowering maneuvers. In the first simulation, the payload is transferred 50 m. During the transfer operation the payload is hoisted up 15 m starting from a position 35 m below the trolley with an acceleration of 0.75 m/s^2, after the hoist acceleration is concluded in the first two seconds, the trolley starts to accelerate with a maximum acceleration of 0.5 m/s^2 to reach a maximum velocity of 3 m/s, Fig. 3.14(a). The payload motion trajectory is shown in Fig. 3.14(b), and the controller switching times are listed in Table 3.1. The total transfer

Table 3.1: Switching times of the controller for a hoisting maneuver from L_i to L_f.

$L_i\ (m)$	$L_f\ (m)$	$t_{a_1}\ (sec)$	$t_o\ (sec)$	$t_{c_1}\ (sec)$	$t_{a_2}\ (sec)$
35	20	2.5762	3.6751	3.9538	7.3777
20	20	3.0000	3.1859	3.3717	6.3717
20	25	3.3145	3.4186	3.9776	6.6632
20	35	3.4601	3.6677	4.7279	7.2678

operation is conducted in 25.6 seconds. The maximum oscillation amplitude is 12.2 mm after the acceleration stage and 15.4 mm at the end of the transfer maneuver. Figures 3.14(c)

and 3.14(d) show the payload oscillation and the phase portrait of the system dynamics throughout the transfer maneuver.

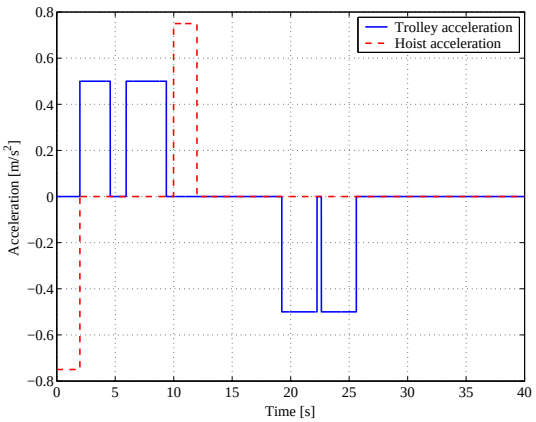

(a) Trolley and hoist acceleration

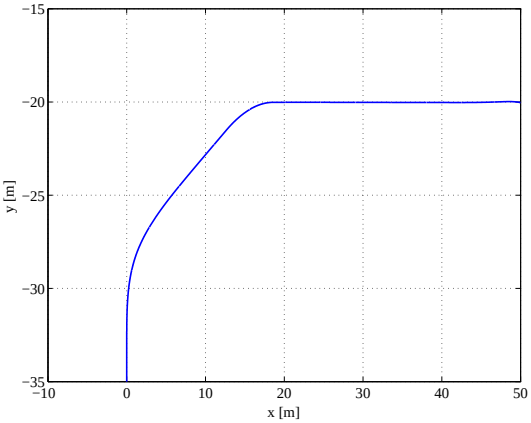

(b) Motion profile

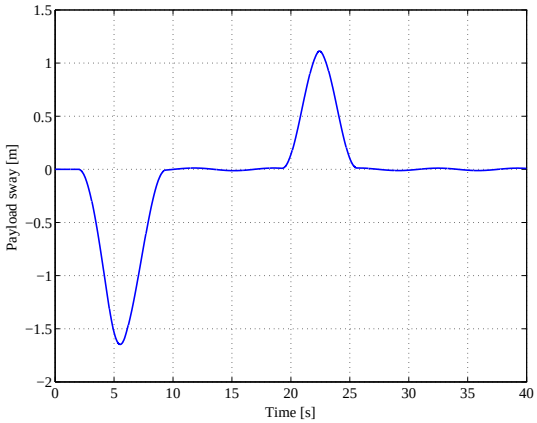

(c) Payload sway

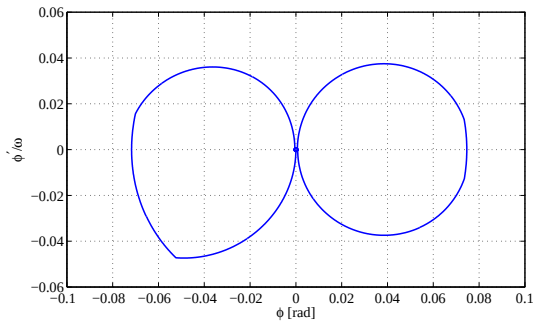

(d) Phase portrait

Figure 3.14: A transfer operation involving a 15 m hoisting.

In the second simulation, the payload is transferred 50 m starting from a position 20 m below the trolley. During the transfer operation the payload is lowered 15 m with an acceleration

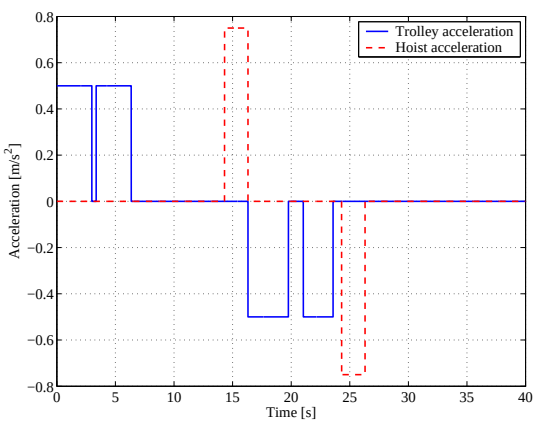

(a) Trolley and hoist acceleration

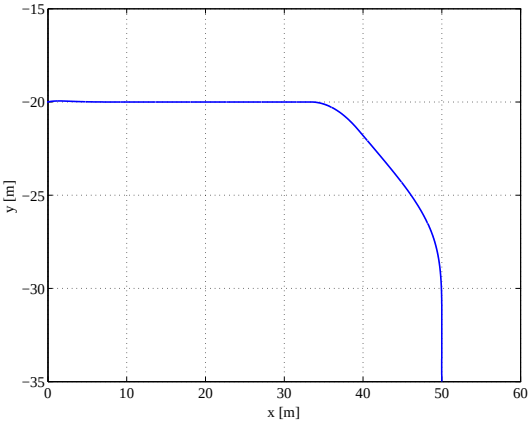

(b) Motion profile

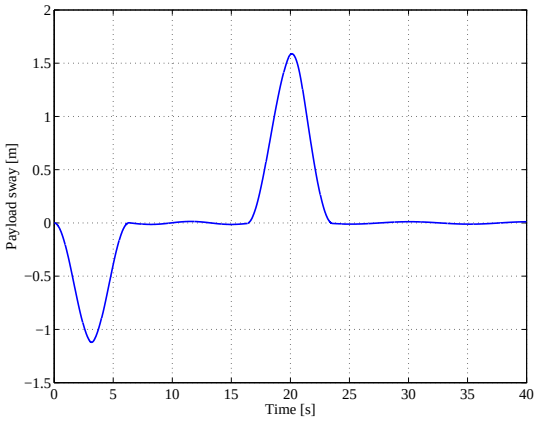

(c) Payload sway

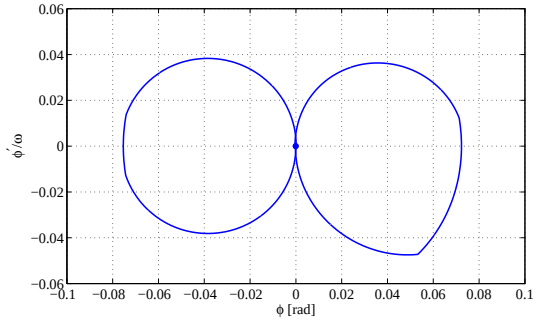

(d) Phase portrait

Figure 3.15: A transfer operation involving a 15 m lowering.

of 0.75 m/s^2, Fig. 3.15(a). The payload motion trajectory is shown in Fig. 3.15(b). The controller performance is shown in Figs. 3.15(c) and 3.15(d). The total transfer operation

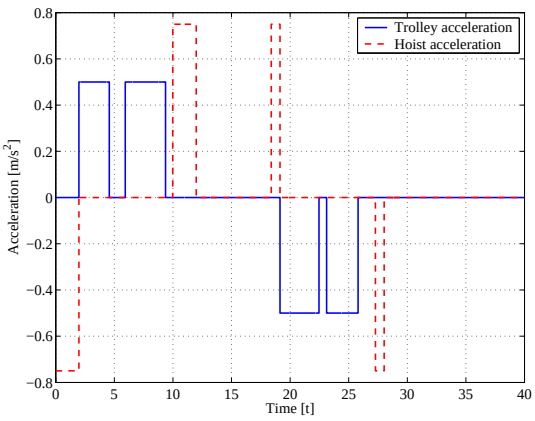

(a) Trolley and hoist acceleration

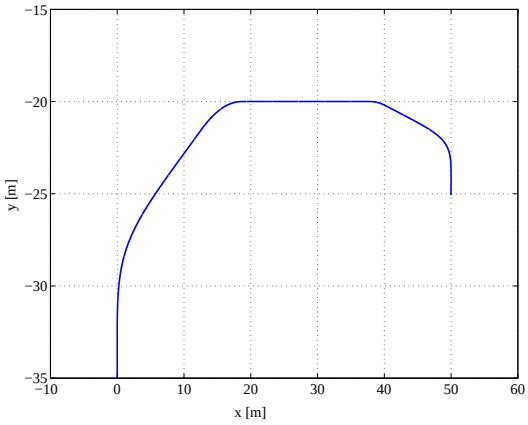

(b) Motion profile

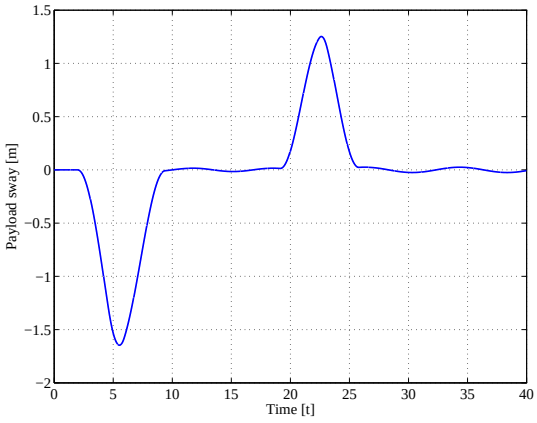

(c) Payload sway

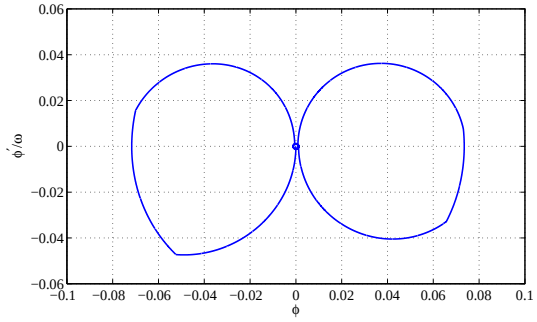

(d) Phase portrait

Figure 3.16: A transfer operation involving a 15 m hoisting and a 5 m lowering.

is concluded in 26.3 seconds. The amplitude of the resulting payload oscillations is 12.5 mm after the acceleration stage and 11.4 mm at the end of the transfer maneuver.

In the third simulation, the payload is transferred 50 m starting from a position 35 m below the trolley. During the transfer operation the payload is hoisted up 15 m and then lowered 5 m, Fig. 3.16(b). The system performance is shown in Fig. 3.16(c) and 3.16(d). The total transfer operation is concluded in 28 seconds. The amplitude of the resulting payload oscillations is 15.4 mm after the acceleration stage and 25 mm at the end of the transfer maneuver.

Chapter 4

Experimental Validation of the Controllers

In this chapter, we provide a brief description of a 1:10 scale model of a 65-ton quay-side container crane that we built to validate the theoretical models and test the controllers. We first validate the input-shaping controller that we designed in Chapter 3 for automated crane operations. Then, we illustrate the robustness and effectiveness of the delayed-position feedback controller through operator-in-the-loop experiments.

4.1 Experimental Setup

To validate the theory and the computer simulations, we built a 1:10 scale model of a 65-ton quay-side container crane, as shown in Fig. 4.1. The support mechanism consists of two 7 m aluminum tracks that are supported by 10 aluminum L-shaped supports. The supports are attached to the ceiling by twenty 5/8$''$ steel threaded rods. The trolley shown in Fig. 4.2 is assembled, mounted on the tracks, and actuated to move in either direction using a BM500E DC brushless rotary servomotor. The motor has a 4000 rpm rated speed,

Figure 4.1: A 1:10 scale model of a 65-ton quay-side container crane.

510 $N.m$ continuous torque, and 1.5 hp rated power. To achieve the required trolley speed and torque, the motor is mounted on a 1:5 ratio gear box.

The hoist mechanism consists of four steel cables connected to four aluminium pulleys at the trolley and to four points on the spreader bar. The spreader bar is attached to a 1:10 scale model of a 10 ft by 10 ft by 20 ft container. The four pulleys are actuated to rotate

in either direction using two BM500E DC brushless rotary servomotors. To achieve the required speed and torque, the two motors are mounted on two 1:35 ratio gearboxes. The rated capabilities and critical dimensions of the scaled model are available in Table 4.1.

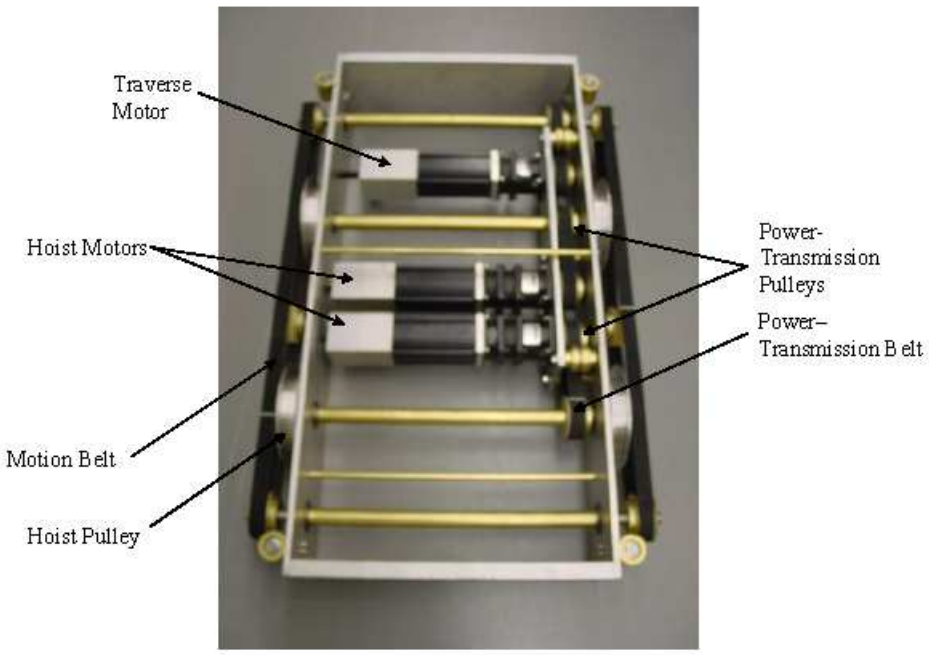

Figure 4.2: Assembled trolley of a 1:10 scale model of a 65-ton quay-side container crane.

Each motor is connected to a Velocity/Torque amplifier. The amplifier reads a differential +/-10 volts signal and commutates the motor using a sine wave current command. The commutation is achieved using a quadrature encoder mounted on the motor shaft. The input signal can be either a velocity or a torque command. In our application, we used the velocity input mode.

Two quadrature high precision optical encoders are mounted on two cables at each side of the trolley. The encoders are used to read the in-plane angle of the payload hoisting cables. The average of both readings is used to avoid any errors that might result from the container

Table 4.1: Rated capabilities and critical dimensions of the experimental setup.

Trolley velocity	1 m/s
Hoist velocity	1 m/s
Trolley acceleration	0.5 m/s^2
Hoist acceleration	0.5 m/s^2
Distance between hoisting cables at the trolley (d)	0.28 m
Distance between hoisting cables at the spreader bar (w)	0.14 m
Usable track length (S)	5 m
Distance between the center of gravity of the payload and the top of the spreader bar (R)	0.25 m
Maximum hoist distance	2.5 m

twist.

A data acquisition board is added to a 450 MHz desktop computer. The board has 8 channels of analog input, 8 channels of analog output, 8 encoder counters, and 32 channels of digital inputs/outputs. The board was used to sample the optical encoders data and to communicate with the amplifiers and the safety limit switches. A C++ code was developed to sample the data registers of the acquisition board, drive the amplifiers of the traverse and hoist motors, and communicate with the user interface devices. Two joysticks are used to simulate the operator-in-the-loop scenarios.

For safety concerns, a C++ code was used to calculate the trolley position on the tracks. If the trolley is within a certain distance from either end of the tracks, the current supplied to the traverse motor decreases gradually causing the trolley to decelerate and stop. A number of limit switches are mounted on each end of the track to ensure safety in case of code failure. These switches disable the amplifiers, causing the trolley to decelerate under its own inertia. To drive the trolley to complete stop, hydraulic dampers and air springs are installed at both ends of the track.

4.2 Experimental Validation of Input-Shaping Control

Two experiments were conducted to validate the input-shaping control technique that we proposed for automated crane operations. There are two performance measures for the controller. The first is that the controller incorporates the maximum crane capabilities listed in Table 4.1. This guarantees the conclusion of the transfer operation in minimal time. The second is that the magnitude of the residual oscillations is less than 5 mm in magnitude at the end of the transfer maneuver.

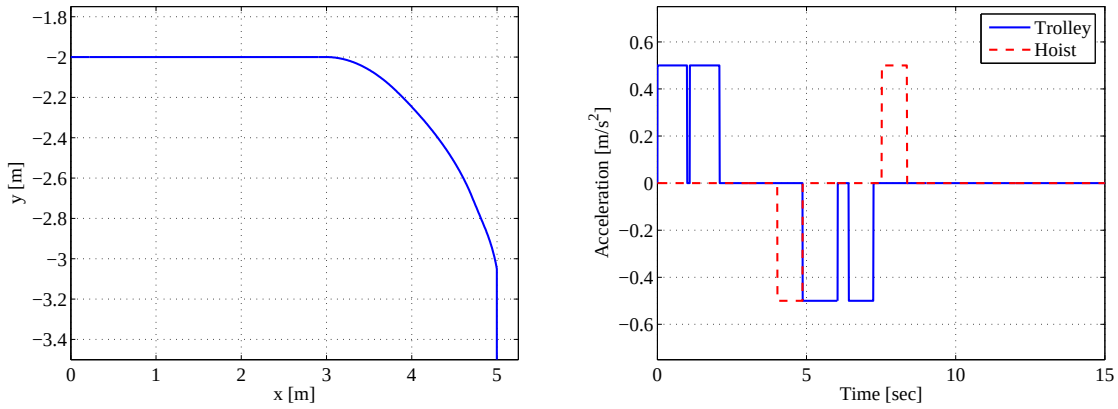

(a) Motion profile

(b) Trolley and hoist acceleration

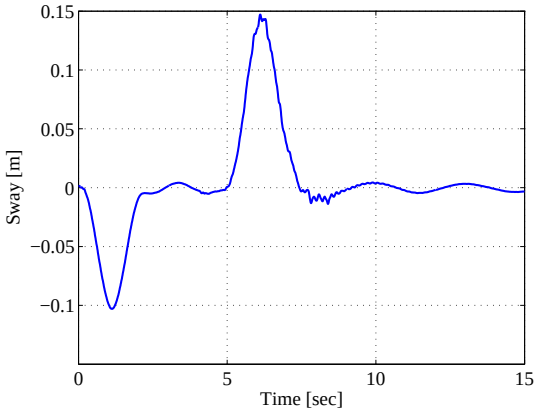

(c) Payload sway

Figure 4.3: A 5 m payload transfer operation involving a 1.5 m lowering.

In the first experiment, the payload is transferred 5 m. During the transfer operation the payload is lowered 1.5 m starting from a position 2 m below the trolley with an acceleration of 0.5 m/s^2. The payload motion trajectory is shown in Fig. 4.3(a). The trolley starts to accelerate with a maximum acceleration of 0.5 m/s^2 to reach a maximum velocity of 1 m/s, Fig. 4.3(b). The total transfer operation is conducted in 8.4 seconds. The resulting residual oscillations magnitude is less than 4 mm at the end of the acceleration stage and less than 4.5 mm at the end of the transfer maneuver. Figure 4.3(c) illustrates the payload sway throughout the transfer maneuver.

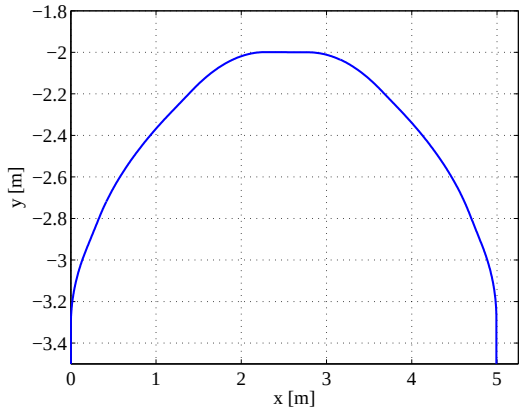

(a) Motion profile

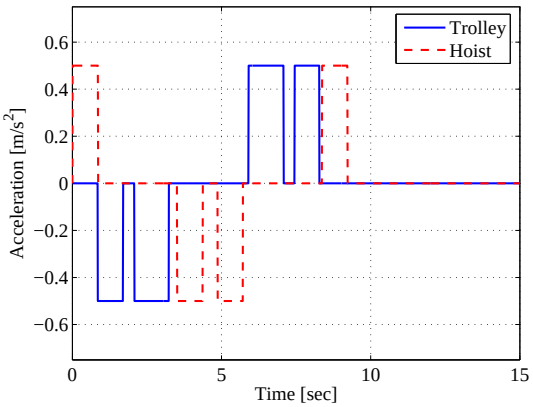

(b) Trolley and hoist acceleration

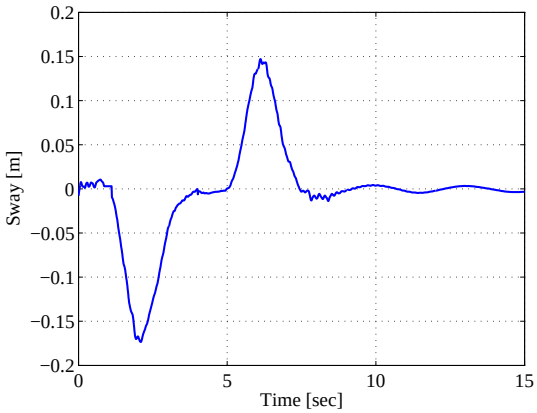

(c) Payload sway

Figure 4.4: A 5 m payload transfer operation involving a 1.5 m hoisting then 1.5 m lowering.

In the second experiment, the payload is transferred 5 m. During the transfer operation the payload is first hoisted 1.5 m starting from a position 3.5 m below the trolley then lowered 1.5 m starting form a position 2 m below the trolley. The payload motion trajectory is shown in Fig. 4.4(a). The trolley starts to accelerate with a maximum acceleration of 0.5 m/s^2 to reach a maximum velocity of 1 m/s and the payload is hoisted and lowered with a maximum acceleration of 0.5 m/s^2 to reach a maximum speed of 1 m/s, Fig. 4.4(b). The total transfer operation is conducted in 9.2 seconds. The maximum residual oscillations magnitude is less than 4.2 mm at the end of the acceleration stage and less than 4.5 mm at the end of the transfer maneuver. Figure 4.4(c) illustrates the payload sway throughout the transfer maneuver.

Many other automated crane experiments were conducted. These experiments involved different hoisting and lowering maneuvers. In all cases, the maximum crane capabilities were incorporated and the residual vibrations were less than 5 mm in magnitude, which demonstrates the effectiveness of the controller.

4.3 Experimental Validation of Delayed-Position Feedback Control

For operator-in-the-loop crane operations, input-shaping controllers do not provide an alternative. These controllers require predefined trolley and payload paths, which are not available if the operator was to operate the crane using the crane joysticks. Therefore, we use the delayed-position feedback controller analyzed in Chapter 3 to stabilize the payload for random trolley input commands and hoisting operations. The input commands were augmented with the controller feedback signal without interfering with the actual operator input.

To demonstrate the effectiveness and robustness of the controller, we conducted two exper-

iments. In the first experiment, an operator randomly moved the trolley along the crane tracks while performing random hoisting and lowering operations without switching on the controller. In the second experiment, the operator repeated the process but with the controller switched on. For safety concerns, because the payload sway can be dangerously large without control, we limited the trolley and hoist velocities to half the maximum crane capabilities in the first experiment, whereas we used the maximum capabilities of the crane in the second experiment.

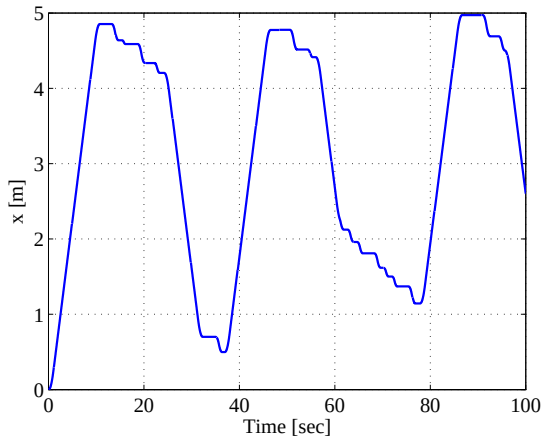

(a) Trolley motion profile

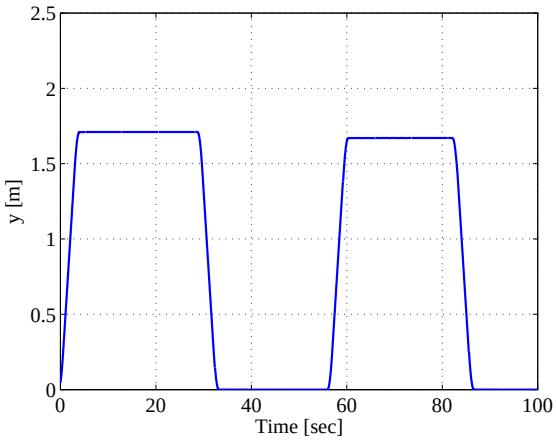

(b) Payload hoist profile

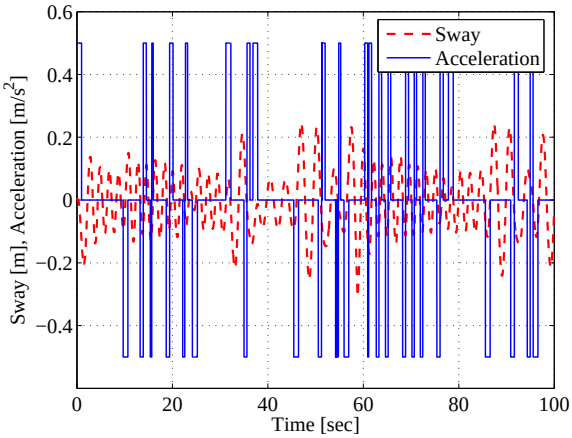

(c) Input acceleration and payload sway

Figure 4.5: Uncontrolled operator-in-the-loop operation of the container crane. Only half of the maximum crane capabilities were used in this experiment.

In the first experiment, the crane operator arbitrarily moved the trolley three times back and forth, Fig. 4.5(a). At the same time he hoisted and lowered the payload two times Fig. 4.5(b). As these maneuvers were conducted, the payload sway increased to dangerously large magnitudes up to 0.25 m as shown in Fig. 4.5(c). This is equivalent to almost 2.5 m sway on a full scale container crane. These sustained large oscillations existed even for the periods when the trolley is not moving. In fact, it is obvious in Fig. 4.5(a), that the crane

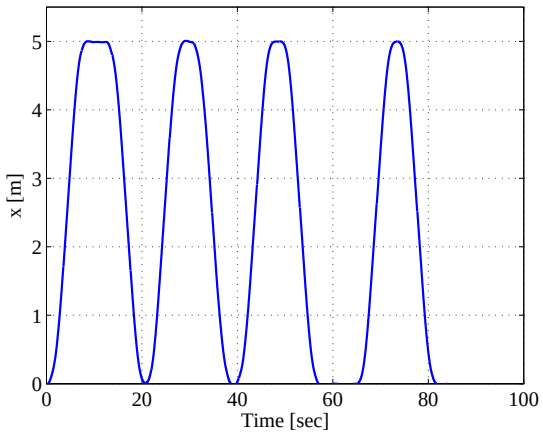

(a) Trolley motion profile

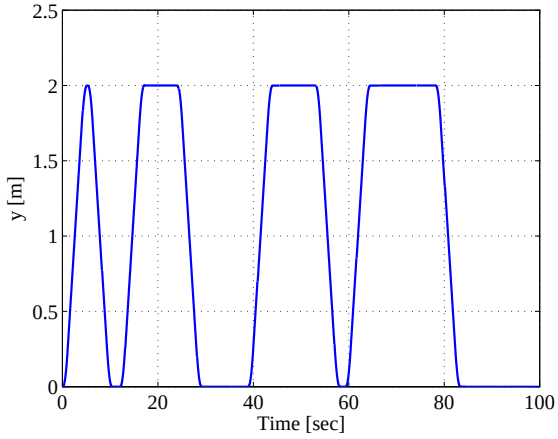

(b) Payload hoist profile

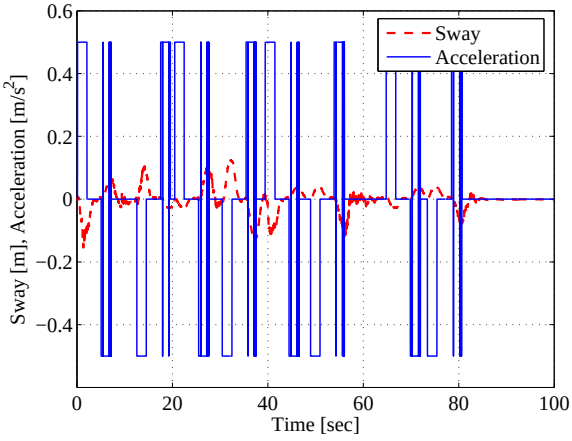

(c) Input acceleration and payload sway

Figure 4.6: Controlled operator-in-the-loop operation of the container crane. Maximum crane capabilities were used in this experiment.

operator tried to minimize these sustained oscillations by manually making the trolley track the payload using small steps in the trolley motion. However, with all of the effort and experience, these oscillations can still be large and dangerous and significantly increase the payload transfer time.

In the second experiment, the controller was switched on and the delayed feedback signal was added to the operator input. The operator moved the trolley four times back and forth on the track, Fig. 4.6(a), while simultaneously hoisting and lowering the payload four times, Fig. 4.6(b). Although, the experiment was conducted using the maximum velocity of the crane, the controller kept the payload oscillations minimal, as shown in Fig. 4.6(c). In fact, at the end of each acceleration or deceleration step, the controller was capable of driving the oscillations of the payload to less than 5 mm in less than 4 s.

Chapter 5

Modeling of Torsional Micromirrors

In this chapter, we develop a comprehensive model of a torsional micromirror subjected to electric excitations. First, we provide a general overview of the device, then we use Laplace's equation to derive an expression for the electrostatic energy. Using the resulting expression, we write the Lagrangian of the system and carry out a Galerkin expansion to develop a reduced-order model that captures the static and dynamic responses of the mirror.

5.1 The Micromirror

We consider the micromirror device shown in Fig. 5.1. This device was proposed by [69, 70]. It consists of two identical microbeams of length l, width w, and thickness h. The beams are fixed on one side and connected to a rigid rectangular plate (the mirror) on the other side. The mirror has a length L_m, width a, and thickness h. Beneath the micromirror there are two electrodes each of length b and width $c = (a_2 - a_1)/2$. The perpendicular distance between the undeformed position of the mirror and the electrodes is denoted as d. The whole microstructure is etched out of a silicon substrate that has a density ρ, a Young's modulus E, and a modulus of rigidity G.

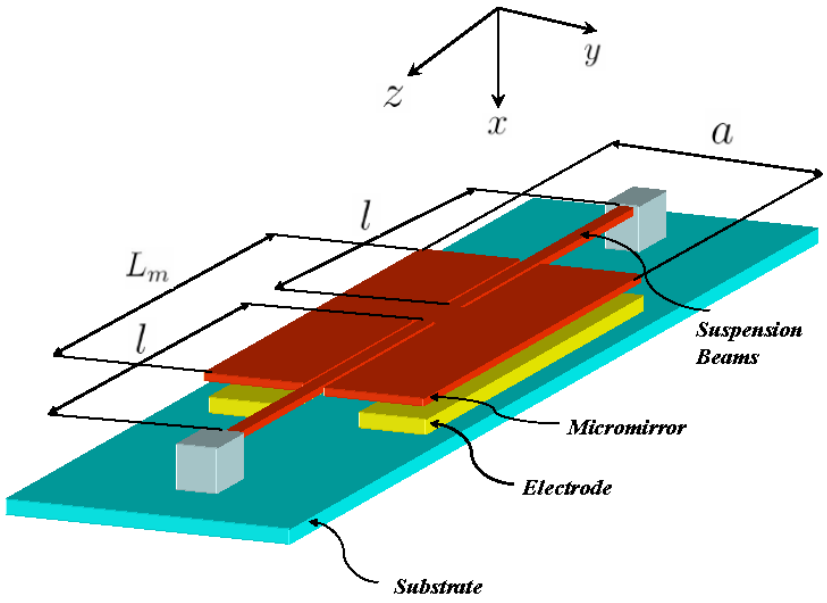

(a) Perspective view

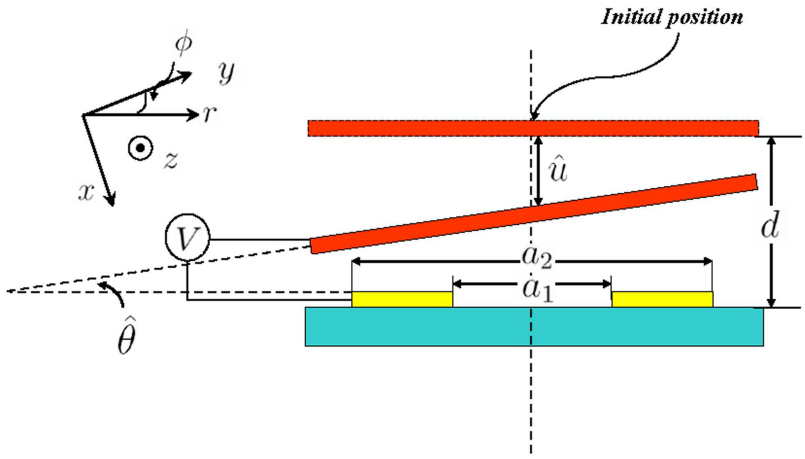

(b) Cross-sectional view

Figure 5.1: Schematic diagram of a micromirror.

The mirror is activated to rotate in either direction by supplying a voltage $V(\tau)$ to the corresponding electrode. This results in an electrostatic potential between the electrode and the mirror, which generates an electrostatic pressure P on the lower surface of the mirror, and hence produces a downward electrostatic force $\mathbf{F}_e$ and an electrostatic moment $\mathbf{M}_e$ around

the suspension point. Consequently, the microbeams undergo simultaneous and distributed torsion $\hat{\theta}(x,\tau)$ and deflection $\hat{u}(x,\tau)$ and the micromirror rotates an angle $\hat{\theta}_m(\tau)$ and deflects a distance $\hat{u}_m(\tau)$.

5.2 Electrostatic Actuation

Assuming that the mirror is infinitely long (thereby adopting the parallel-plate theory and neglecting non-uniformity in the electrostatic field due to fringing effects towards the ends), the electrostatic potential between the mirror and each of the electrodes can be represented by Laplace's equation with appropriate boundary conditions. In the cylindrical coordinates (r,ϕ,z), the electrostatic potential (Φ) is governed by

$$\begin{aligned} \frac{d^2\Phi(\phi)}{d\phi^2} &= 0 \\ \Phi(0) = 0, \qquad \Phi(\hat{\theta}_m) &= V \end{aligned} \tag{5.1}$$

whose solution can be expressed as

$$\Phi(\phi) = \frac{V}{\hat{\theta}_m}\phi \tag{5.2}$$

The electrostatic field $\mathbf{E}$ is given by

$$\mathbf{E} = -\nabla\Phi = -\frac{V}{r\hat{\theta}_m}\hat{\phi} \tag{5.3}$$

where $\hat{\phi}$ is the unit vector in the direction of ϕ. The electrostatic charge density on the mirror can be written as

$$\rho = \epsilon_0\mathbf{E} = \frac{\epsilon_0 V}{r\hat{\theta}_m} \tag{5.4}$$

where ϵ_0 is the dielectric constant of air. The resulting capacitance between the mirror and the bottom electrodes is

$$\begin{aligned} C = \frac{1}{V}\int \rho dA &= \frac{\epsilon_0}{\hat{\theta}_m}\int_0^b\int_{r_1}^{r_2}\frac{1}{r}drdz \\ &= \frac{\epsilon_0 b}{\hat{\theta}_m}\ln\frac{r_2}{r_1} \end{aligned} \tag{5.5}$$

where r_1 and r_2 are defined in Fig. 5.1(b) and can be further expressed as

$$r_1 = \frac{d-\hat{u}_m}{\tan\hat{\theta}_m} - \frac{a_2}{2}, \qquad r_2 = \frac{d-\hat{u}_m}{\tan\hat{\theta}_m} - \frac{a_1}{2} \tag{5.6}$$

Substituting Equation (5.6) into Equation (5.5), we obtain

$$C = \frac{\epsilon_0 b}{\hat{\theta}_m} \ln\left[\frac{d-\hat{u}_m - \frac{1}{2}a_1\tan\hat{\theta}_m}{d-\hat{u}_m - \frac{1}{2}a_2\tan\hat{\theta}_m}\right] \tag{5.7}$$

The total potential energy of the electrostatic force is given by

$$U_e = -\frac{1}{2}CV^2 = -\frac{\epsilon_0 b}{2\hat{\theta}_m}V^2 \ln\left[\frac{d-\hat{u}_m - \frac{1}{2}a_1\tan\hat{\theta}_m}{d-\hat{u}_m - \frac{1}{2}a_2\tan\hat{\theta}_m}\right] \tag{5.8}$$

Using Equation (5.8), we can derive the total electrostatic force and moment as follows:

$$\mathbf{F}_e = -\frac{\partial U_e}{\partial \hat{u}_m} = \frac{\epsilon_0 b}{2\hat{\theta}_m}V^2\left[\frac{1}{d-\hat{u}_m - \frac{1}{2}a_2\tan\hat{\theta}_m} - \frac{1}{d-\hat{u}_m - \frac{1}{2}a_1\tan\hat{\theta}_m}\right] \tag{5.9a}$$

$$\begin{aligned}\mathbf{M}_e = -\frac{\partial U_e}{\partial \hat{\theta}_m} = \frac{\epsilon_0 b}{2}V^2\Bigg\{&\frac{1}{\hat{\theta}_m}\left[\frac{\frac{1}{2}a_2\sec^2\hat{\theta}_m}{d-\hat{u}_m - \frac{1}{2}a_2\tan\hat{\theta}_m} - \frac{\frac{1}{2}a_1\sec^2\hat{\theta}_m}{d-\hat{u}_m - \frac{1}{2}a_1\tan\hat{\theta}_m}\right]\\ &+ \frac{1}{\hat{\theta}_m^2}\ln\left[\frac{d-\hat{u}_m - \frac{1}{2}a_2\tan\hat{\theta}_m}{d-\hat{u}_m - \frac{1}{2}a_1\tan\hat{\theta}_m}\right]\Bigg\}\end{aligned} \tag{5.9b}$$

For small rotation angles, one can assume that $(\sin\theta \approx \theta, \cos\theta \approx 1)$, which further simplifies the expressions for the electrostatic force and moment to

$$\mathbf{F}_e = \frac{\epsilon_0 b}{2\hat{\theta}_m}V^2\left[\frac{1}{d-\hat{u}_m - \frac{1}{2}a_2\hat{\theta}_m} - \frac{1}{d-\hat{u}_m - \frac{1}{2}a_1\hat{\theta}_m}\right] \tag{5.10a}$$

$$\mathbf{M}_e = \frac{\epsilon_0 b}{2\hat{\theta}_m^2}V^2\left\{\frac{d-\hat{u}_m}{d-\hat{u}_m - \frac{1}{2}a_2\hat{\theta}_m} - \frac{d-\hat{u}_m}{d-\hat{u}_m - \frac{1}{2}a_1\hat{\theta}_m} + \ln\left[\frac{d-\hat{u}_m - \frac{1}{2}a_2\hat{\theta}_m}{d-\hat{u}_m - \frac{1}{2}a_1\hat{\theta}_m}\right]\right\} \tag{5.10b}$$

Next we nondimensionlize Equations (5.10a) and (5.10b) to obtain

$$\mathbf{F}_e = \frac{\epsilon_0 b}{2d\theta_{cr}\theta_m} V^2 \left[\frac{1}{1-u_m-\beta\theta_m} - \frac{1}{1-u_m-\alpha\theta_m} \right] \tag{5.11a}$$

$$\mathbf{M}_e = \frac{\epsilon_0 b}{2\theta_{cr}^2\theta_m^2} V^2 \left\{ \frac{\beta\theta_m}{1-u_m-\beta\theta_m} - \frac{\alpha\theta_m}{1-u_m-\alpha\theta_m} + \ln\left[\frac{1-u_m-\beta\theta_m}{1-u_m-\alpha\theta_m} \right] \right\} \tag{5.11b}$$

where

$$\alpha = \frac{a_1}{a}, \qquad \beta = \frac{a_2}{a}, \qquad \theta_{cr} = \frac{2d}{a}, \qquad \theta = \frac{\hat{\theta}}{\theta_{cr}}, \qquad u = \frac{\hat{u}}{d}. \tag{5.12}$$

The expressions for the electrostatic force and moment have a removable singularity at $\theta_m = 0$. To avoid computational overflows, we take the limits of Equations (5.11a) and (5.11b) and obtain

$$\mathbf{F}_e = \frac{\epsilon_0 b V^2}{2d\theta_{cr}} \frac{\beta-\alpha}{(1-u_m)^2} \tag{5.13a}$$

$$\mathbf{M}_e = \frac{\epsilon_0 b V^2}{4\theta_{cr}^2} \frac{\beta^2-\alpha^2}{(1-u_m)^2} \tag{5.13b}$$

5.3 Reduced-Order Model

To generate a compact model of the device under electrostatic excitations, we develop a reduced-order model that describes the statics and dynamics of the micromirror. We treat the micromirror as a rigid plate and write the Lagrangian of the system as

$$\mathcal{L} = T_b + T_m - U_b - U_m - U_e \tag{5.14}$$

where (T_b, U_b) and (T_m, U_m) are the kinetic and potential energies of the two suspension beams and the micromirror plate, respectively. The system kinetic energy can be expressed as

$$\begin{aligned} T_b &= \frac{1}{2} I_{b_{zz}} \int_0^{2l} \hat{\theta}_\tau^2 \, dz + \frac{1}{2} m \int_0^{2l} \hat{u}_\tau^2 \, dz \\ T_m &= \frac{1}{2} I_{m_{zz}} \hat{\theta}_{m\tau}^2 + \frac{1}{2} M \hat{u}_{m\tau}^2 \end{aligned} \tag{5.15}$$

where $I_{b_{zz}} = \frac{1}{12}\rho hw(h^2+w^2)$ is the mass moment of inertia of the suspension beams per unit length around the z-axis, $I_{m_{zz}} = \frac{1}{12}\rho ahL_m(h^2+a^2)$ is the mass moment of inertia of the mirror around the z-axis, $m = \rho wh$ is the mass of the beam per unit length, and $M = \rho hL_m a$ is the mass of the plate. The subscripts τ and z denote partial derivatives of the variables $\hat{u}$ and $\hat{\theta}$; that is ($\square_\tau = \frac{\partial \square}{\partial \tau}, \square_{z\tau} = \frac{\partial^2 \square}{\partial z \partial \tau}, \ldots$).

The potential energies U_b and U_m can be expressed as

$$\begin{aligned} U_b &= \frac{1}{2}GJ_b \int_0^{2l} \hat{\theta}_z^2 \, dz + \frac{1}{2}EI_{b_y} \int_0^{2l} \hat{u}_{zz}^2 \, dz \\ U_m &= -Mg\hat{u}_m \end{aligned} \tag{5.16}$$

where $J_b = \frac{16w^4}{3}\left[1 - \frac{192(w/h)}{\pi^5}\sum_{n=0}^{\infty}\frac{1}{(2n+1)^5}\tanh\frac{(2n+1)^5}{2(w/h)}\right]$ is the polar moment of inertia of the suspension beams that accounts for cross-sectional warping effects, and $I_{b_y} = \frac{1}{12}wh^3$ is the area moment of inertia of the suspension beams around the y-axis. Next, we substitute Equations (5.8), (5.15), and (5.16) into Equation (5.14) and nondimensionalize the time τ and space z independent variables and obtain

$$\begin{aligned} \mathcal{L} = &\int_0^1 \theta_t^2 \, d\xi + \gamma_1 \int_0^1 u_t^2 d\xi - \int_0^1 \theta_\xi^2 \, d\xi - \gamma_2 \int_0^1 u_{\xi\xi}^2 \, d\xi \\ &+ \gamma_3\theta_{mt}^2 + \gamma_4 u_{mt}^2 + \gamma_5 u_m + \frac{\gamma_6}{\theta_m}\ln\left[\frac{1-u_m-\alpha\theta_m}{1-u_m-\beta\theta_m}\right] \end{aligned} \tag{5.17}$$

where

$$\begin{aligned} &\xi = \frac{z}{2l}, && \tau = \frac{t}{T}, && \gamma_1 = \frac{12d^2}{\theta_{cr}^2(h^2+w^2)}, \\ &\gamma_2 = \frac{Eh^3wd^2}{48GJ_bl^2\theta_{cr}^2}, && \gamma_3 = \frac{aL_m(h^2+a^2)}{2lw(h^2+w^2)}, && \gamma_4 = \frac{6L_mad^2}{wl(h^2+w^2)\theta_{cr}^2}, \\ &\gamma_5 = \frac{4\rho haL_mgdl}{GJ_b\theta_{cr}^2}, && \gamma_6 = \frac{2\epsilon_0 bV^2l}{GJ_b\theta_{cr}^3}. \end{aligned}$$

are dimensionless quantities and

$$T^2 = \frac{\rho whl^2(h^2+w^2)}{3GJ_b}$$

is a time scale. To generate the reduced-order model, we carry out a Galerkin expansion of the rotation θ and deflection u in the Lagrangian. To this end, we assume that the temporal

and spatial variations of the rotation and deflection can be separated and written in the form

$$\begin{aligned} \theta(\xi,t) &= \sum_{i=1}^{\infty} p_i(t)\psi_i(\xi) \\ u(\xi,t) &= \sum_{i=1}^{\infty} q_i(t)\varphi_i(\xi) \end{aligned} \tag{5.18}$$

where the p_i and q_i are the generalized coordinates corresponding to the basis sets ψ_i and φ_i of the rotation angle θ and the deflection u, respectively. We choose them to be the orthonormal eigenfunctions of the free torsional vibrations of a clamped-clamped beam and the bending vibrations of a clamped-clamped beam with a concentrated mass at its middle. The basis set used to represent θ is given by the following eigenvalue problem:

$$\frac{d^2\psi}{d\xi^2} + \frac{I_{b_z}\omega^2}{GJ_b}\psi = 0, \qquad \psi(0) = 0, \qquad \psi(1) = 0. \tag{5.19}$$

Hence,

$$\psi_i(\xi) = \sqrt{2}\sin(i\pi\xi), \qquad i = 1, 2, 3, \ldots \tag{5.20}$$

The basis set used to represent u is derived from the free transverse vibrations of a clamped-clamped beam with a concentrated mass at the middle of the beam; that is,

$$\begin{aligned} &\frac{d^4\varphi_1}{d\xi^4} - k^4\varphi_1 = 0, && \frac{d^4\varphi_2}{d\xi^4} - k^4\varphi_2 = 0, \\ &\varphi_1(0) = 0, && \varphi_1'(0) = 0, \\ &\varphi_2(1) = 0, && \varphi_2'(1) = 0, \\ &\varphi_1(\tfrac{1}{2}) = \varphi_2(\tfrac{1}{2}), && \varphi_1'(\tfrac{1}{2}) = \varphi_2'(\tfrac{1}{2}), \\ &\varphi_1''(\tfrac{1}{2}) = \varphi_2''(\tfrac{1}{2}), && \varphi_1'''(\tfrac{1}{2}) + m_r k^4\varphi_1(\tfrac{1}{2}) = \varphi_2'''(\tfrac{1}{2}). \end{aligned} \tag{5.21}$$

where $k^4 = (\rho w h \omega^2)/(EI_{b_z})$ and $m_r = M/(2\rho whl)$ is the mass ratio. The solution of Equations (5.21) can be expressed as

$$\varphi_i(\xi) = \begin{cases} \varphi_{i1}(\xi) = C_1\sin k_i\xi + C_2\cos k_i\xi + C_3\cosh k_i\xi + C_4\sinh k_i\xi & \xi \le \frac{1}{2}, \\ \varphi_{i2}(\xi) = C_5\sin k_i\xi + C_6\cos k_i\xi + C_7\cosh k_i\xi + C_8\sinh k_i\xi & \xi > \frac{1}{2}. \end{cases} \qquad i = 1, 2, \ldots \tag{5.22}$$

where $(C_1, C_2, \ldots, C_8)$ are constants. Substituting Equation (5.22) into Equation (5.21) yields eight homogeneous algebraic equations in the unknown constants. Setting the determinant of these equations equal to zero yields the characteristic equation

$$\begin{aligned} 2(1-\cos k\cosh k) + m_r k[&\sin k\cosh k\cosh^2\frac{k}{2} - \cos k\sinh k\cos^2\frac{k}{2} \\ &+ \cos k\cosh k(\sin\frac{k}{2}\cosh\frac{k}{2} - \cos\frac{k}{2}\sinh\frac{k}{2}) \\ &+ \cos k\sinh k(\cos\frac{k}{2}\cosh\frac{k}{2} - \sin\frac{k}{2}\sinh\frac{k}{2}) \\ &- \sin k\cosh k(\cos\frac{k}{2}\cosh\frac{k}{2} + \sin\frac{k}{2}\sinh\frac{k}{2}) \\ &+ \sin k\sinh k(\sin\frac{k}{2}\cosh\frac{k}{2} + \cos\frac{k}{2}\sinh\frac{k}{2}) \\ &- \sin k\sinh k(\cos\frac{k}{2}\sin\frac{k}{2} + \cosh\frac{k}{2}\sinh\frac{k}{2}) \\ &+ \cos\frac{k}{2}\sinh\frac{k}{2} - \sin\frac{k}{2}\cosh\frac{k}{2}] = 0 \end{aligned} \tag{5.23}$$

The eigenfunction are normalized according to

$$\int_0^1 \varphi_i(\xi)\varphi_j(\xi) = \delta_{ij} \tag{5.24}$$

where δ is the Kronecker delta. For the basis sets, we have

$$\int_0^1 \psi_i'\psi_j'\, d\xi = \Lambda_{ij}\delta_{ij}, \qquad \int_0^1 \varphi_i''\varphi_j''\, d\xi = \Upsilon_{ij}\delta_{ij} \tag{5.25}$$

Having defined the basis sets $\psi_i(\xi)$ and $\varphi_i(\xi)$, we substitute Equations (5.18) and (5.25) into Equation (5.17) and obtain

$$\begin{aligned} \mathcal{L} = \sum_{i=1}^{\infty}\Big\{\dot{p}_i^2 + \gamma_1\dot{q}_i^2 - \gamma_2 q_i^2\Upsilon_{ii} - p_i^2\Lambda_{ii} + \gamma_5 q_i\varphi_i(\tfrac{1}{2})\Big\} + \sum_{i=1}^{\infty}\sum_{j=1}^{\infty}\Big\{\gamma_3\dot{p}_i\dot{p}_j\psi_i(\tfrac{1}{2})\psi_j(\tfrac{1}{2}) \\ + \gamma_4\dot{q}_i\dot{q}_j\varphi_i(\tfrac{1}{2})\varphi_j(\tfrac{1}{2})\Big\} + \frac{\gamma_6}{\sum_{i=1}^{\infty} p_i\psi_i(\tfrac{1}{2})}\ln\Big[\frac{1-\sum_{i=1}^{\infty}(q_i\varphi_i(\tfrac{1}{2}) + \alpha p_i\psi_i(\tfrac{1}{2}))}{1-\sum_{i=1}^{\infty}(q_i\varphi_i(\tfrac{1}{2}) + \beta p_i\psi_i(\tfrac{1}{2}))}\Big] \end{aligned} \tag{5.26}$$

Then, using Euler-Lagrange equations, the equations of motion can be expressed as

$$\ddot{p}_i + \gamma_3 \sum_{j=1}^{\infty} \ddot{p}_j \psi_i(\tfrac{1}{2})\psi_j(\tfrac{1}{2}) + p_i \Lambda_{ii} = \frac{\gamma_6 \psi_j(\frac{1}{2})}{2\sum_{j=1}^{\infty} p_j \psi_j(\frac{1}{2})} \Bigg\{ \frac{\beta}{1 - \sum_{j=1}^{\infty}(q_j \varphi_j(\frac{1}{2}) + \beta p_j \psi_j(\frac{1}{2}))} - \frac{\alpha}{1 - \sum_{j=1}^{\infty}(q_j \varphi_j(\frac{1}{2}) + \alpha p_j \psi_j(\frac{1}{2}))} + \frac{1}{2\sum_{j=1}^{\infty} p_j \psi_j(\frac{1}{2})} \ln\Bigg[\frac{1 - \sum_{j=1}^{\infty}(q_j \varphi_j(\frac{1}{2}) + \beta p_j \psi_j(\frac{1}{2}))}{1 - \sum_{j=1}^{\infty}(q_j \varphi_j(\frac{1}{2}) + \alpha p_j \psi_j(\frac{1}{2}))} \Bigg] \Bigg\} \tag{5.27}$$

$$\gamma_1 \ddot{q}_i + \gamma_4 \sum_{j=1}^{\infty} \ddot{q}_j \varphi_i(\tfrac{1}{2})\varphi_j(\tfrac{1}{2}) + \gamma_2 q_i \Upsilon_{ii} - \tfrac{1}{2}\gamma_5 \varphi_i(\tfrac{1}{2}) = \frac{\gamma_6 \varphi_i(\frac{1}{2})}{2\sum_{j=1}^{\infty} p_j \psi_j(\frac{1}{2})} \Bigg[\frac{1}{1 - \sum_{j=1}^{\infty}(q_j \varphi_j(\frac{1}{2}) + \beta p_j \psi_j(\frac{1}{2}))} - \frac{1}{1 - \sum_{j=1}^{\infty}(q_j \varphi_j(\frac{1}{2}) + \alpha p_j \psi_j(\frac{1}{2}))} \Bigg] \tag{5.28}$$

We can truncate the basis sets up to n and m basis functions for the torsion and deflection and rewrite Equations (5.27) and (5.28) in the following matrix form:

$$\begin{pmatrix} 1 + \gamma_3 \psi_1(\frac{1}{2})\psi_1(\frac{1}{2}) & \gamma_3 \psi_1(\frac{1}{2})\psi_2(\frac{1}{2}) & \dots & \gamma_3 \psi_1(\frac{1}{2})\psi_n(\frac{1}{2}) \\ \gamma_3 \psi_1(\frac{1}{2})\psi_2(\frac{1}{2}) & 1 + \gamma_3 \psi_2(\frac{1}{2})\psi_2(\frac{1}{2}) & \dots & \gamma_3 \psi_2(\frac{1}{2})\psi_n(\frac{1}{2}) \\ \vdots & \gamma_3 \psi_2(\frac{1}{2})\psi_{n-1}(\frac{1}{2}) & \ddots & \vdots \\ \gamma_3 \psi_1(\frac{1}{2})\psi_n(\frac{1}{2}) & \gamma_3 \psi_2(\frac{1}{2})\psi_n(\frac{1}{2}) & \dots & 1 + \gamma_3 \psi_n(\frac{1}{2})\psi_n(\frac{1}{2}) \end{pmatrix} \begin{pmatrix} \ddot{p}_1 \\ \ddot{p}_2 \\ \vdots \\ \ddot{p}_n \end{pmatrix} + \begin{pmatrix} \Lambda_{11} & \dots & 0 & 0 \\ \vdots & \Lambda_{22} & 0 & 0 \\ 0 & 0 & \ddots & \vdots \\ 0 & 0 & \dots & \Lambda_{nn} \end{pmatrix} \begin{pmatrix} p_1 \\ p_2 \\ \vdots \\ p_n \end{pmatrix} = \frac{1}{2}\gamma_6 F_p \begin{pmatrix} \psi_1(\frac{1}{2}) \\ \psi_2(\frac{1}{2}) \\ \vdots \\ \psi_n(\frac{1}{2}) \end{pmatrix} \tag{5.29}$$

$$\begin{pmatrix} \gamma_1+\gamma_4\varphi_1(\frac{1}{2})\varphi_1(\frac{1}{2}) & \gamma_4\varphi_1(\frac{1}{2})\varphi_2(\frac{1}{2}) & \dots & \gamma_4\varphi_1(\frac{1}{2})\varphi_m(\frac{1}{2}) \\ \gamma_4\varphi_1(\frac{1}{2})\varphi_2(\frac{1}{2}) & \gamma_1+\gamma_4\varphi_2(\frac{1}{2})\varphi_2(\frac{1}{2}) & \dots & \gamma_4\varphi_2(\frac{1}{2})\varphi_m(\frac{1}{2}) \\ \vdots & \gamma_4\varphi_2(\frac{1}{2})\varphi_{m-1}(\frac{1}{2}) & \ddots & \vdots \\ \gamma_4\varphi_1(\frac{1}{2})\varphi_m(\frac{1}{2}) & \gamma_4\varphi_2(\frac{1}{2})\varphi_m(\frac{1}{2}) & \dots & \gamma_1+\gamma_4\varphi_m(\frac{1}{2})\varphi_m(\frac{1}{2}) \end{pmatrix} \begin{pmatrix} \ddot{q}_1 \\ \ddot{q}_2 \\ \vdots \\ \ddot{q}_m \end{pmatrix} + \gamma_2 \begin{pmatrix} \Upsilon_{11} & \dots & 0 & 0 \\ \vdots & \Upsilon_{22} & 0 & 0 \\ 0 & 0 & \ddots & \vdots \\ 0 & 0 & \dots & \Upsilon_{mm} \end{pmatrix} \begin{pmatrix} q_1 \\ q_2 \\ \vdots \\ q_m \end{pmatrix} = (\frac{\gamma_6}{2}F_q + \frac{\gamma_5}{2}) \begin{pmatrix} \varphi_1(\frac{1}{2}) \\ \varphi_2(\frac{1}{2}) \\ \vdots \\ \varphi_m(\frac{1}{2}) \end{pmatrix} \tag{5.30}$$

where

$$F_p = \frac{1}{\sum_{j=1}^{n} p_j\psi_j(\frac{1}{2})}\Bigg\{\frac{\beta}{1-\sum_{j=1}^{m} q_j\varphi_j(\frac{1}{2})-\beta\sum_{j=1}^{n} p_j\psi_j(\frac{1}{2})} - \frac{\alpha}{1-\sum_{j=1}^{m} q_j\varphi_j(\frac{1}{2})-\alpha\sum_{j=1}^{n} p_j\psi_j(\frac{1}{2})} + \frac{1}{\sum_{j=1}^{n} p_j\psi_j(\frac{1}{2})}\ln\Bigg[\frac{1-\sum_{j=1}^{m} q_j\varphi_j(\frac{1}{2})-\beta\sum_{j=1}^{n} p_j\psi_j(\frac{1}{2})}{1-\sum_{j=1}^{m} q_j\varphi_j(\frac{1}{2})-\alpha\sum_{j=1}^{n} p_j\psi_j(\frac{1}{2})}\Bigg]\Bigg\}$$

$$F_q = \frac{1}{\sum_{j=1}^{n} p_j\psi_j(\frac{1}{2})}\Bigg[\frac{1}{1-\sum_{j=1}^{m} q_j\varphi_j(\frac{1}{2})-\beta\sum_{j=1}^{n} p_j\psi_j(\frac{1}{2})} - \frac{1}{1-\sum_{j=1}^{m} q_j\varphi_j(\frac{1}{2})-\alpha\sum_{j=1}^{n} p_j\psi_j(\frac{1}{2})}\Bigg]$$

Chapter 6

Static Response of Torsional Micromirrors

Using Euler-Bernoulli beam theory, we derive two equations that are solved numerically for the exact equilibrium position of the mirror. We use the resulting equations to validate the reduced-order model. We show that the static response obtained using the reduced-order model agrees with available experimental data. Based on the reduced-order model, we derive an expression to determine the pull-in parameters of the mirror. We find that the pull-in parameters obtained using this expression are in excellent agreement with the experimental data.

6.1 Exact Static Solution

In the absence of time variations, the Lagrangian, Equation (5.17), reduces to

$$\mathcal{L}_s = -2\int_0^{1/2} \theta_\xi^2 \, d\xi - 2\gamma_2 \int_0^{1/2} u_{\xi\xi}^2 \, d\xi + \gamma_5 u_m + \frac{\gamma_6}{\theta_m} \ln\left[\frac{1-u_m-\alpha\theta_m}{1-u_m-\beta\theta_m}\right] \tag{6.1}$$

To develop an expression for the exact static solution, we follow the Euler-Bernoulli beam

theory. The deflection and torsion of the beam satisfy the following problems:

$$\frac{d^4u}{d\xi^4}=0, \qquad u(0)=0, \qquad \frac{du}{d\xi}(0)=0, \qquad u\left(\frac{1}{2}\right)=u_m, \qquad \frac{du}{d\xi}\left(\frac{1}{2}\right)=\frac{l}{d}\Theta_m. \tag{6.2}$$

$$\frac{d^2\theta}{d\xi^2}=0, \qquad \theta(0)=0, \qquad \theta\left(\frac{1}{2}\right)=\theta_m. \tag{6.3}$$

where Θ_m is the slope at the end of the beam. Solving Equations (6.2) and (6.3) for $u(\xi)$ and $\theta(\xi)$, respectively, we obtain

$$u(\xi)=8\left(\frac{l}{d}\Theta_m-2u_md\right)\xi^3+8\left(3u_m-\frac{l}{d}\Theta_m\right)\xi^2 \tag{6.4}$$

$$\theta(\xi)=2\theta_m\xi \tag{6.5}$$

Substituting Equations (6.4) and (6.5) into Equation (6.1) yields

$$\mathcal{L}_s=-4\theta_m^2-\gamma_2(192u_m^2-192\frac{l}{d}u_m\Theta_m+64\frac{l^2}{d^2}\Theta_m^2)+\gamma_5u_m+\frac{\gamma_6}{\theta_m}\ln\left[\frac{1-u_m-\alpha\theta_m}{1-u_m-\beta\theta_m}\right] \tag{6.6}$$

In our case, the plate is assumed to be rigid, symmetric about the y-axis, and subjected to symmetric electrostatic forces. As a result, the plate does not rotate around the y-axis; that is, $\Theta_m=0$. Consequently, the expression for the total strain energy reduces to

$$\mathcal{L}_s=-4\theta_m^2-192\gamma_2u_m^2+\gamma_5u_m+\frac{\gamma_6}{\theta_m}\ln\left[\frac{1-u_m-\alpha\theta_m}{1-u_m-\beta\theta_m}\right] \tag{6.7}$$

For static equilibrium, the Lagrangian $\mathcal{L}_s$ exhibits a local extremum. Therefore, the derivatives of the total energy with respect to the two degrees of freedom u_m and θ_m vanish. Hence,

$$\mathcal{F}=\begin{bmatrix}\frac{\partial\mathcal{L}_s}{\partial u_m}\\ \frac{\partial\mathcal{L}_s}{\partial\theta_m}\end{bmatrix}=\begin{bmatrix}\mathbf{F}_e+Mg-\frac{24EI_{b_y}u_m}{l^3}\\ \mathbf{M}_e-\frac{2GJ_b\theta_m}{l}\end{bmatrix}=0 \tag{6.8}$$

where $\mathbf{M}_e$ and $\mathbf{F}_e$ are given by Equations (5.11a) and (5.11b). For a given voltage V, Equations (6.8) are solved numerically for the mirror deflection u_m and rotation angle θ_m. The results are then substituted into Equations (6.4) and (6.5) to obtain the static equilibrium of the suspension beams.

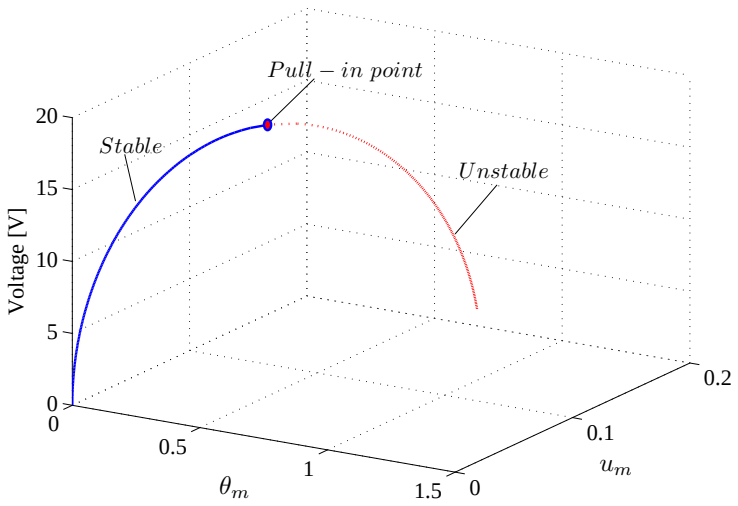

Figure 6.1: Variation of the equilibria with the driving voltage V.

6.2 Static Pull-in

For a given voltage V, solving Equations (6.8) yields two equilibrium states as shown in Fig. 6.1. The smaller equilibrium position is stable, whereas the larger equilibrium position is unstable. When V is gradually increased, the stable equilibrium increases slowly, and the unstable equilibrium decreases. At a certain voltage, they collide and disappear in a saddle-node bifurcation. As V is increased further no equilibrium solutions exist. This causes the mirror to abruptly collapse to the nearest of the fixed electrodes. This phenomenon is known as pull-in or snap down. At pull-in the applied voltage V, the rotation angle θ, and the deflection u are referred to as pull-in voltage V_p, pull-in angle θ_p, and pull-in deflection u_p, respectively. The pull-in parameters are usually used to define a safe operation regime, where the micromirror can smoothly and continuously deflect to a certain equilibrium position. Moreover, V_p gives an estimate of the voltage required to achieve the maximum deflection state. Therefore, V_p is always kept as low as possible to minimize the voltage requirement.

Many researchers addressed the problem of pull-in [63–67, 70, 76]. They developed methods and derived expressions to determine the pull-in parameters. An approach developed by [76]

utilizes the fact that the applied voltage V has a local maximum at pull-in, see Fig. 6.1. Therefore, to determine the pull in parameters, one can maximize the vector function $\mathcal{F}$ defined by Equation (6.8) using implicit function optimization techniques. The local maximum of $\mathcal{F}$ is satisfied when

$$|\nabla\mathcal{F}| = \begin{vmatrix} \frac{\partial^2 U_T}{\partial u^2} & \frac{\partial^2 U_T}{\partial u \partial \theta} \\ \frac{\partial^2 U_T}{\partial \theta \partial u} & \frac{\partial^2 U_T}{\partial \theta^2} \end{vmatrix} = 0 \tag{6.9}$$

Solving Equations (6.8) and (6.9) simultaneously, one can determine the pull-in parameters. This step is very critical in the micromirror design procedure because it allows the designer to optimize the micromirror dimensions and hence obtain a proper choice of the pull-in parameters.

There is a significant amount of research on the parameters affecting pull-in. In general, there are only three main nondimensional parameters that affect the pull-in state. The first two are related to the electrodes dimensions and positions with respect to the mirror, namely α and β, and the third is the ratio of the effective bending to the effective torsional stiffness, which we define as

$$\kappa = \frac{3EI_{b_y}a^2}{GJ_b l^2} \tag{6.10}$$

As κ is increased, the effective bending resistance increases, and therefore the micromirror tends to have greater resistance to bending motions and the pull-in voltage increases. The effects of the electrode geometric parameters α, the location of the inner side of the electrodes, and β, the location of the outer side of the electrodes, are shown in Figs. 6.2 and 6.3 for $\kappa = 110$ and $\kappa = 4$, respectively.

As β is increased for $\kappa = 110$, Fig. 6.2, the pull-in rotation angle θ_p, deflection u_p, and voltage V_p decrease. This is due to the fact that the larger β is, for a fixed α, the larger the electrostatic energy is relative to the mechanical restoring force, which results in faster pull-in. As α is increased, for a fixed β, the size of the electrode is decreased and the pull-in voltage is increased as shown in Fig. 6.2 (c). Whereas the electrostatic energy depends linearly on the area of the electrode, it depends quadratically on the voltage. As a result, increasing the voltage to account for the decrease in the area of the electrode leads to a faster increase in

the electrostatic energy to the extent it dominates the mechanical restoring force and hence leads to a lower pull-in rotation angle and deflection, Figs. 6.2 (a) and (b). Furthermore, increasing α moves the center of the electrode away from the mirror rotation axis. As a result, the proportion of the electrostatic moment to the electrostatic force increases. This leads to a relatively smaller drop in the pull-in rotation angle Fig. 6.2 (a) than the drop in the deflection Fig. 6.2 (b).

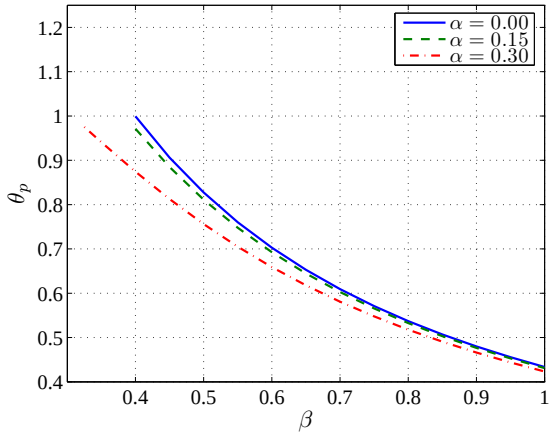

(a) Pull-in rotation angle.

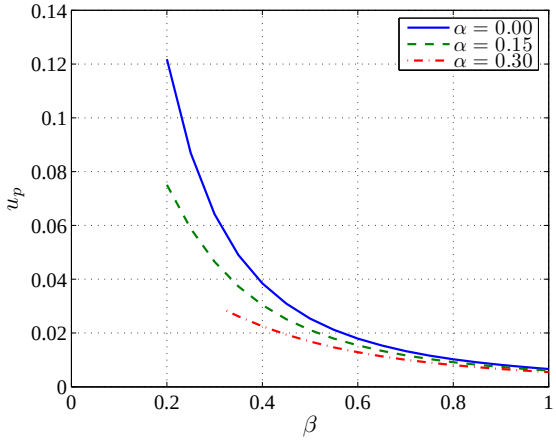

(b) Pull-in deflection.

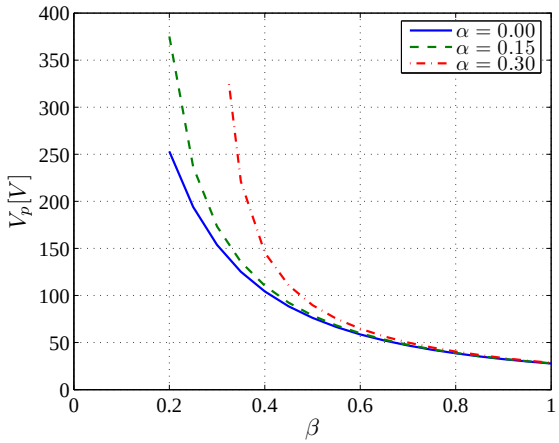

(c) Pull-in voltage.

Figure 6.2: Variation of the pull-in parameters with the electrode size and position α and β when $\kappa = 110$.

For $\kappa = 4$, the bending and torsional stiffnesses are of the same order of magnitude and the rotation angle and deflection are also of the same order of magnitude, as shown in Fig. 6.3. The larger deflection in this case, compared to $\kappa = 110$, makes the overall gap between the electrode and the mirror larger for the same rotation angle θ. As a result the electrostatic force dominates the mechanical restoring force, resulting in an increase in the pull-in voltage V_p, the rotation angle θ_p, and pull-in deflection u_p.

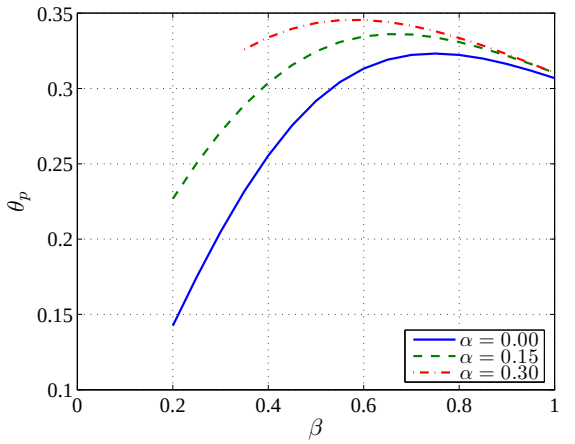

(a) Pull-in rotation angle.

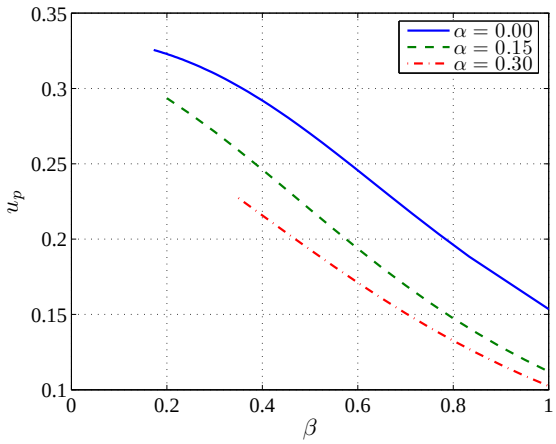

(b) Pull-in deflection.

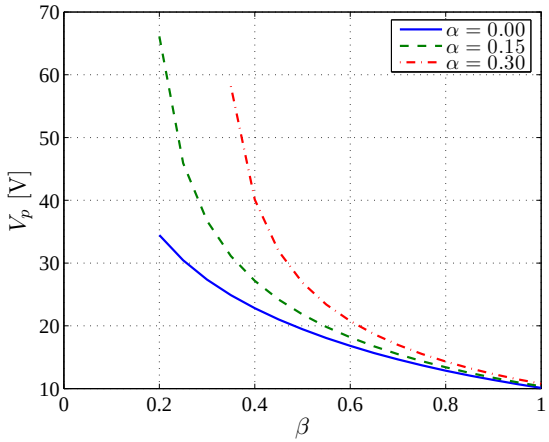

(c) Pull-in voltage.

Figure 6.3: Variation of the pull-in parameters with the electrode size and position α and β when $\kappa = 4$.

As β is increased, the area of the electrode increases and the pull-in voltage V_p and deflection θ_p decrease. On the other hand, as α and β are increased, the center of the electrode moves away from the axis of rotation, leading to an increase in the proportion of the electrostatic moment to the electrostatic force. As a result, for the same deflection u, the rotation angle θ increases.

Since many micromirror applications require accurate torsional motions and no deflections, these findings are interesting. For example, digital projection devices (the Digital Light Processor) and microoptical switching devices suffer significant degradation in performance due to undesirable deflection motions. Therefore, an efficient micromirror design minimizes the mirror deflection. Although a large value of κ can minimize bending motions, it significantly increases the pull-in voltage V_p, see Fig. 6.2(c) and Fig. 6.3(c). This is a significant disadvantage. These complex parameter interactions require thorough optimization analysis.

6.3 Validation of the Reduced-Order Model

In this section, we validate the proposed reduced-order model by comparing its results to the exact static solution and to available experiments. We start by setting the time derivatives in Equations (5.29) and (5.30) equal to zero and obtaining

$$\begin{pmatrix} \Lambda_{11}p_1 \\ \Lambda_{22}p_2 \\ \vdots \\ \Lambda_{nn}p_n \end{pmatrix} = \frac{1}{2}\gamma_6 F_p \begin{pmatrix} \psi_1(\frac{1}{2}) \\ \psi_2(\frac{1}{2}) \\ \vdots \\ \psi_n(\frac{1}{2}) \end{pmatrix} \tag{6.11}$$

$$\begin{pmatrix} \Upsilon_{11}q_1 \\ \Upsilon_{22}q_2 \\ \vdots \\ \Upsilon_{mm}q_m \end{pmatrix} = \frac{1}{2\gamma_2}(\gamma_6 F_q + \gamma_5) \begin{pmatrix} \varphi_1(\frac{1}{2}) \\ \varphi_2(\frac{1}{2}) \\ \vdots \\ \varphi_m(\frac{1}{2}) \end{pmatrix} \tag{6.12}$$

We increase the number of spatial modes (n,m) gradually and solve Equations (6.11) and (6.12) for $(p_1, p_2, \ldots, p_n)$ and $(q_1, q_2, \ldots, q_m)$ until the solution converges. Unless otherwise stated, the parameters of the mirror and electrodes used in the numerical simulations are shown in Table 6.1. The spatial mode shapes are obtained from Equations (5.20) and (5.22), where we choose only the odd mode shapes since the even mode shapes do not contribute to the resulting equilibrium position. Figures 6.4 and 6.5 show convergence of the equilibrium solutions obtained using the reduced-order model to the exact solution obtained using Equations (6.8). The results of the reduced-order model converge to the exact stable and unstable branches using 9 torsional modes and 3 bending modes ($n = 9, m = 3$).

Table 6.1: Numerical values for the parameters of the micromirror and electrodes.

Properties	
Modulus of elasticity, $E[GPa]$	170
Modulus of elasticity, $G[GPa]$	66
Density, $\rho[kg/m^3]$	2330
Dielectric constant of air, $\epsilon_0[F/m]$	8.85×10^{-12}
Dimensions	
Mirror width, $a[\mu m]$	100
Mirror length, $L_m[\mu m]$	100
Beam length, $l[\mu m]$	65
Beam width, $w[\mu m]$	1.55
Beam thickness, $h[\mu m]$	1.50
Electrode length, $b[\mu m]$	100
Electrode parameter, α	0.06
Electrode parameter, β	0.84
Gap height, $d[\mu m]$	2.75

Figure 6.6 shows the equilibrium rotation angle θ and deflection u of one of the suspension beams obtained when a voltage $V = 10$ V is applied to one of the electrodes. There is good agreement between the results obtained with the reduced-order model and the exact solution, Equations (6.4) and (6.5).

The pull-in parameters for the reduced-order model can be determined using a methodology similar to that used for the exact solution. Let us first define

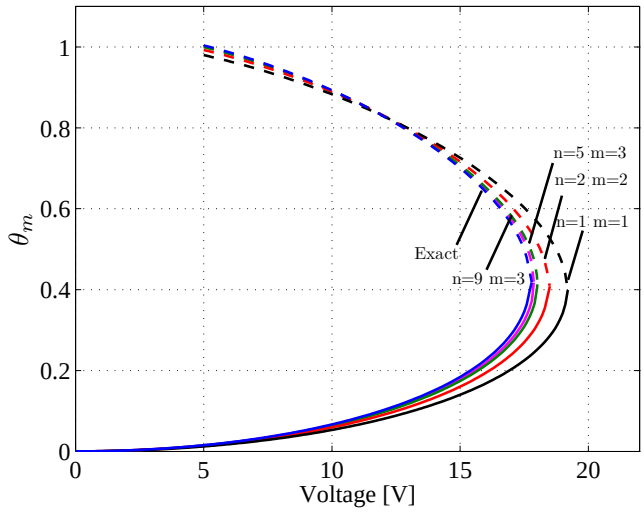

Figure 6.4: Comparison of the mirror rotation angle θ_m obtained from the reduced-order model to the exact solution.

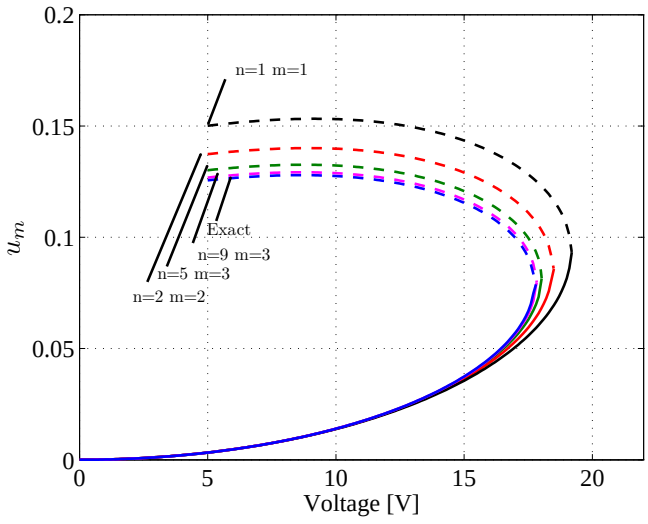

Figure 6.5: Comparison of the mirror deflection u_m obtained from the reduced-order model to the exact solution.

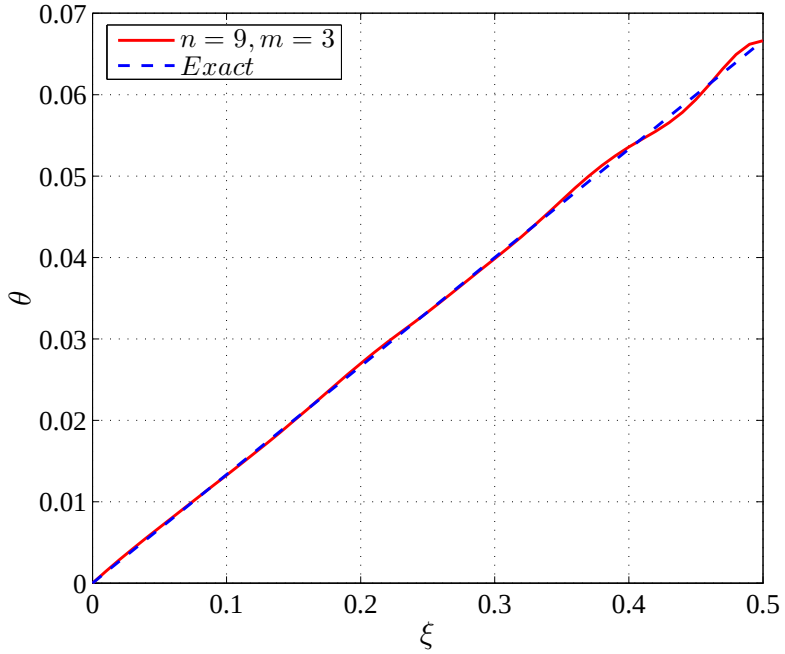

(a) Rotation angle.

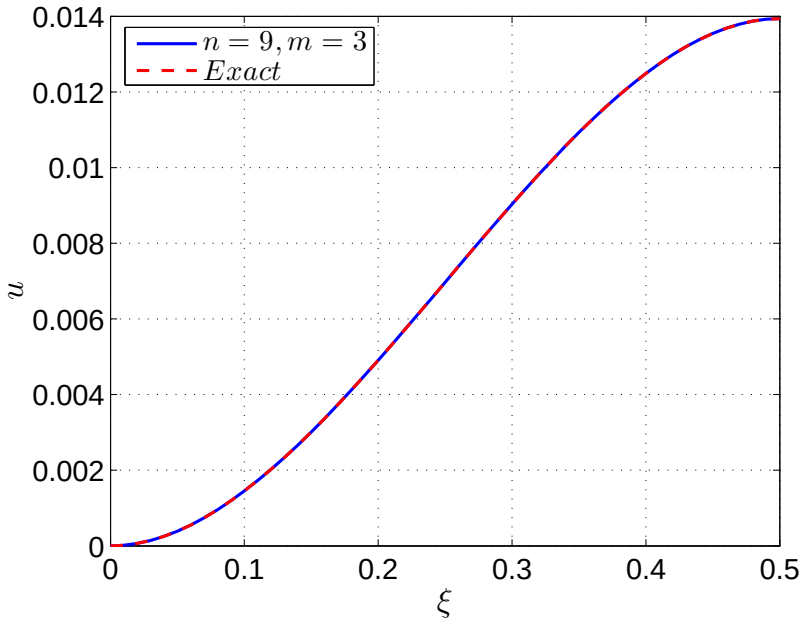

(b) Deflection.

Figure 6.6: Comparison between the static deformation of one of the suspension beams obtained with the reduced-order model and the exact static solution for $V = 10$ V.

$$\mathcal{P} = \begin{pmatrix} \mathcal{P}_1 \\ \mathcal{P}_2 \\ \vdots \\ \vdots \\ \vdots \\ \mathcal{P}_{n+m} \end{pmatrix} = \begin{pmatrix} \Lambda_{11} p_1 \\ \vdots \\ \Lambda_{nn} p_n \\ \Upsilon_{11} q_1 \\ \vdots \\ \Upsilon_{mm} q_m \end{pmatrix} - \begin{pmatrix} \frac{\gamma_6}{2} F_p \psi_1(\frac{1}{2}) \\ \vdots \\ \frac{\gamma_6}{2} F_p \psi_n(\frac{1}{2}) \\ \frac{1}{2\gamma_2}(\gamma_6 F_q + \gamma_5)\varphi_1(\frac{1}{2}) \\ \vdots \\ \frac{1}{2\gamma_2}(\gamma_6 F_q + \gamma_5)\varphi_m(\frac{1}{2}) \end{pmatrix} \tag{6.13}$$

Because the voltage V has a local maximum at pull-in, we let

$$|\nabla \mathcal{P}| = \begin{vmatrix} \frac{\partial \mathcal{P}_1}{\partial p_1} & \cdots & \frac{\partial \mathcal{P}_1}{\partial p_n} & \frac{\partial \mathcal{P}_1}{\partial q_1} & \cdots & \frac{\partial \mathcal{P}_1}{\partial q_m} \\ \frac{\partial \mathcal{P}_2}{\partial p_1} & \cdots & \frac{\partial \mathcal{P}_2}{\partial p_n} & \frac{\partial \mathcal{P}_2}{\partial q_1} & \cdots & \frac{\partial \mathcal{P}_2}{\partial q_m} \\ \vdots & \vdots & \vdots & \vdots & \vdots & \vdots \\ \vdots & \vdots & \vdots & \vdots & \vdots & \vdots \\ \vdots & \vdots & \vdots & \vdots & \vdots & \vdots \\ \frac{\partial \mathcal{P}_{n+m}}{\partial p_1} & \cdots & \frac{\partial \mathcal{P}_{n+m}}{\partial p_n} & \frac{\partial \mathcal{P}_{n+m}}{\partial q_1} & \cdots & \frac{\partial \mathcal{P}_{n+m}}{\partial q_m} \end{vmatrix} = 0 \tag{6.14}$$

Equation (6.14) is solved simultaneously with Equations (6.11) and (6.12) for the pull in voltage V_p and the pull-in generalized coordinates $(p_{p1}, p_{p2}, ..., p_{pn}, q_{p1}, q_{p2}..., q_{pn})$. These coordinates are then used to evaluate the pull-in rotation angle and deflection as

$$\begin{aligned} \theta_p &= \sum_{i=1}^{n} p_{pi} \psi_i(\tfrac{1}{2}) \\ u_p &= \sum_{i=1}^{m} q_{pi} \varphi_i(\tfrac{1}{2}) \end{aligned} \tag{6.15}$$

In Table 6.2, We compare the pull-in parameters obtained using the reduced-order model to those obtained using the exact model, Equations (6.8) and (6.9).

Table 6.2: Pull-in parameters obtained using the exact solution and the reduced-order model.

	V_p	θ_p	u_p
Exact solution	17.74	0.418593	0.0797966
Reduced order model	17.83	0.420137	0.0790955
% error	0.5%	0.36%	0.87%

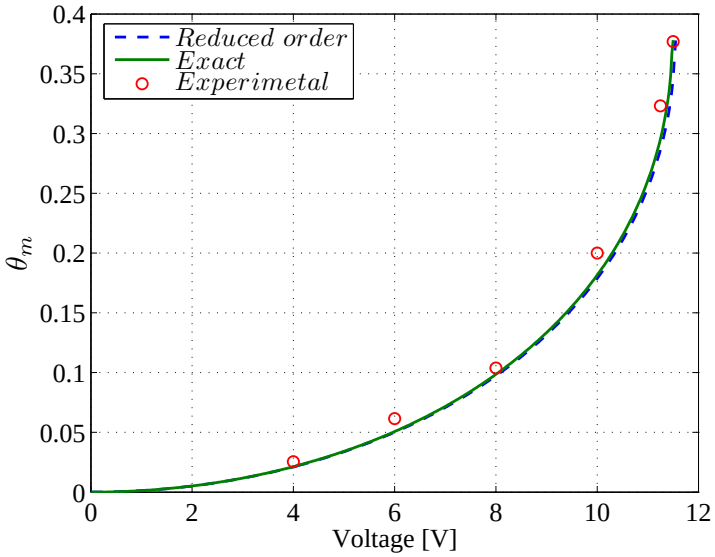

Figure 6.7: Variation of the mirror rotation angle with the driving voltage V.

Table 6.3: Numerical values for the parameters of the micromirror and electrodes used in the experiment of Degani et al. [65]

Properties	
Modulus of elasticity, $E[GPa]$	131
Modulus of elasticity, $G[GPa]$	73
Density, $\rho[kg/m^3]$	2330
Dielectric constant of air, $\epsilon_0[F/m]$	8.85×10^{-12}
Dimensions	
Mirror width, $a[\mu m]$	700
Mirror length, $L_m[\mu m]$	1300
Beam length, $l[\mu m]$	400
Beam width, $w[\mu m]$	31
Beam thickness, $h[\mu m]$	14
Electrode length, $b[\mu m]$	1300
Electrode parameter, α	0.614
Electrode parameter, β	0.975
Gap height, $d[\mu m]$	4.55

Figure 6.7 shows a comparison among the exact solution, the reduced-order model, and experimental results obtained by Degani et al. [65]. The parameters of the mirror used in the experiment are listed in Table 6.3. A comparison among the pull-in parameters is also shown in Table 6.4.

It is worth mentioning that, for the static analysis, the reduced-order model does not simplify the problem. It is much easier to determine the static behavior using the exact solution. However, the accuracy of the reduced-order model in determining the static position of the micromirror as well as the suspension beams validates the model.

Table 6.4: Pull-in parameters obtained using the exact approach, the reduced-order model (n = 9, m = 3), and experimentally by Degani et al. [65]

	V_p	θ_p	u_p
Exact solution	11.49	0.379211	0.0213189
Reduced order model	11.55	0.378462	0.0219582
Experimental results	11.50	0.385	N/A

Chapter 7

Natural Frequencies and Mode Shapes of Torsional Micromirrors

This chapter deals with finding the natural frequencies and mode shapes of the micromirror for voltage values ranging from zero to pull-in. We define the linear eigenvalue problem and solve for the natural frequencies and the associated mode shapes. We show that the natural frequencies of the higher modes are two orders of magnitude larger than the first two natural frequencies. Further, at zero voltage, the eigenfunctions associated with the lowest two modes are the first torsion and bending modes of the suspension beams. Based on these results, we propose treating the mirror as a lumped mass attached to two springs representing the suspension beams. We compare the first two eigenfrequencies obtained using the lumped-mass model to those obtained using the reduced-order model and find excellent agreement over the whole voltage range.

7.1 Eigenvalue Problem

In this section, we study the dynamics of the micromirror shown in Fig. 5.1 around its equilibrium position. We let

$$\begin{aligned} p_i &= p_{is} + p_{id} \qquad i = 1, 2, \ldots, n \\ q_i &= q_{is} + q_{id} \qquad i = 1, 2, \ldots, m \end{aligned} \tag{7.1}$$

where the subscript s denotes the static part of the response, and the subscript d denotes the dynamic part. To obtain the linear eigenvalue problem, we linearize the governing equations around the static equilibrium position $(p_{1s}, p_{2s}, \ldots, p_{ns}, q_{1s}, q_{2s}, \ldots, q_{ms})$. To this end, we substitute Equations (7.1) into Equations (5.29) and (5.30), drop the higher-order terms, use Equations (6.11) and (6.12), and obtain

$$\mathbb{M}\,\ddot{\mathbf{X}} + \mathbb{K}\,\mathbf{X} = \mathbb{F}\,\mathbf{X} \tag{7.2}$$

where

$$\mathbb{M} = \begin{pmatrix} 1+\gamma_3\psi_1(\frac{1}{2})\psi_1(\frac{1}{2}) & \ldots & \gamma_3\psi_1(\frac{1}{2})\psi_n(\frac{1}{2}) & 0 & \ldots & 0 \\ \vdots & \ddots & \vdots & 0 & \ldots & 0 \\ \gamma_3\psi_1(\frac{1}{2})\psi_n(\frac{1}{2}) & \ldots & 1+\gamma_3\psi_n(\frac{1}{2})\psi_n(\frac{1}{2}) & 0 & \ldots & 0 \\ 0 & \ldots & 0 & \gamma_1+\gamma_4\varphi_1(\frac{1}{2})\varphi_1(\frac{1}{2}) & \ldots & \gamma_4\varphi_1(\frac{1}{2})\varphi_m(\frac{1}{2}) \\ 0 & \ldots & 0 & \vdots & \ddots & \vdots \\ 0 & \ldots & 0 & \gamma_4\varphi_1(\frac{1}{2})\varphi_m(\frac{1}{2}) & \ldots & \gamma_1+\gamma_4\varphi_m(\frac{1}{2})\varphi_m(\frac{1}{2}) \end{pmatrix}$$

$$\mathbb{X} = \begin{pmatrix} p_{1d} \\ \vdots \\ p_{nd} \\ q_{1d} \\ \vdots \\ q_{md} \end{pmatrix} \qquad \mathbb{K} = \begin{pmatrix} \Lambda_{11} & 0 & 0 & 0 & \ldots & 0 \\ 0 & \ddots & 0 & 0 & \ldots & 0 \\ 0 & \ldots & \Lambda_{nn} & 0 & \ldots & 0 \\ 0 & \ldots & 0 & \gamma_2\Upsilon_{11} & 0 & 0 \\ 0 & \ldots & 0 & 0 & \ddots & 0 \\ 0 & \ldots & 0 & 0 & \ldots & \gamma_2\Upsilon_{mm} \end{pmatrix}$$

$$\mathbb{F} = \frac{\gamma_6}{2} \left(\begin{array}{cccccc} \frac{\partial F_p}{\partial p_{1d}}\psi_1(\frac{1}{2}) & \dots & \frac{\partial F_p}{\partial p_{nd}}\psi_1(\frac{1}{2}) & \frac{\partial F_p}{\partial q_{1d}}\psi_1(\frac{1}{2}) & \dots & \frac{\partial F_p}{\partial q_{md}}\psi_1(\frac{1}{2}) \\ \vdots & \dots & \vdots & \vdots & \dots & \vdots \\ \frac{\partial F_p}{\partial p_{1d}}\psi_n(\frac{1}{2}) & \dots & \frac{\partial F_p}{\partial p_{nd}}\psi_n(\frac{1}{2}) & \frac{\partial F_p}{\partial q_{1d}}\psi_n(\frac{1}{2}) & \dots & \frac{\partial F_p}{\partial q_{md}}\psi_n(\frac{1}{2}) \\ \frac{\partial F_q}{\partial p_{1d}}\varphi_1(\frac{1}{2}) & \dots & \frac{\partial F_q}{\partial p_{nd}}\varphi_1(\frac{1}{2}) & \frac{\partial F_q}{\partial q_{1d}}\varphi_1(\frac{1}{2}) & \dots & \frac{\partial F_q}{\partial q_{md}}\varphi_1(\frac{1}{2}) \\ \vdots & \dots & \vdots & \vdots & \dots & \vdots \\ \frac{\partial F_q}{\partial p_{1d}}\varphi_m(\frac{1}{2}) & \dots & \frac{\partial F_q}{\partial p_{nd}}\varphi_m(\frac{1}{2}) & \frac{\partial F_q}{\partial q_{1d}}\varphi_m(\frac{1}{2}) & \dots & \frac{\partial F_q}{\partial q_{md}}\varphi_m(\frac{1}{2}) \end{array} \right) \Bigg|_{p_i=p_{is}, q_i=q_{is}}$$

Next, we assume that the solution has the form

$$\mathbb{X} = \mathbb{A}_i e^{i\omega_i t} \tag{7.3}$$

Substituting Equation (7.3) into Equation (7.2), we obtain

$$(\mathbb{K} - \mathbb{F} - \mathbb{M}\ \omega_i^2)\mathbb{A}_i = 0 \tag{7.4}$$

For a nontrivial solution, we set

$$|\mathbb{K} - \mathbb{F} - \mathbb{M}\ \omega_i^2| = 0 \tag{7.5}$$

The characteristic equation (7.5) is solved numerically for the eigenfrequencies ω_i corresponding to the static configuration $(p_{1s}, p_{2s}, \dots, p_{ns}, q_{1s}\ , q_{2s}, \dots, p_{ms})$. They are then substituted into Equation (7.4) to obtain the corresponding eigenvectors $\mathbb{A}_i$.

7.1.1 Natural Frequencies

We solved Equation (7.5) numerically for the natural frequencies for voltage values ranging from zero to pull-in V_p. To determine the number of spatial mode shapes necessary for convergence, we gradually increased the number of modes (n, m) until the addition of new mode shapes did not contribute within a specified tolerance to the resulting eigenfrequencies over the whole voltage range. In our case, the solution converged when the number of torsional modes $n = 8$ and the number of bending modes $m = 3$.

At zero voltage $\gamma_6 = 0$, and the eigenvalue problem uncouples into two parts corresponding to torsion and bending. Solution of the uncoupled eigenvalue problems reveals that the lowest eigenvalue is associated with torsion, the next two eigenvalues are associated with bending, the fourth, fifth, and sixth are associated with torsion, the seventh is associated with bending, etc. For all other voltages, the solution of Equation (7.5) shows that these modes maintain their relative ordering. Figures. 7.1-7.3 show the first five natural frequencies as well as the convergence results of the first two frequencies. As the applied voltage is increased, the first and second natural frequencies decrease sharply, reflecting the system approach to pull-in. However, the third, fourth, and fifth frequencies do not change appreciably. At the pull-in voltage, the first natural frequency ω_1 passes through zero, which indicates a dynamic instability.

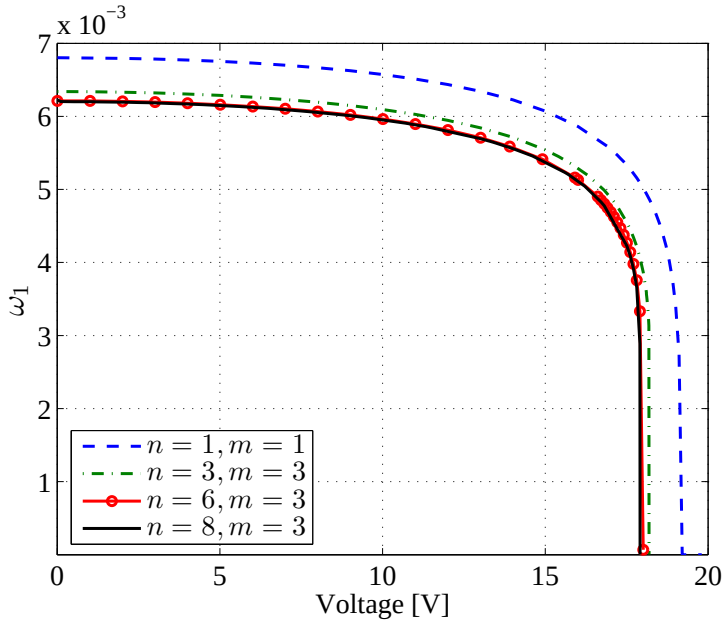

Figure 7.1: First nondimensional natural frequency ω_1.

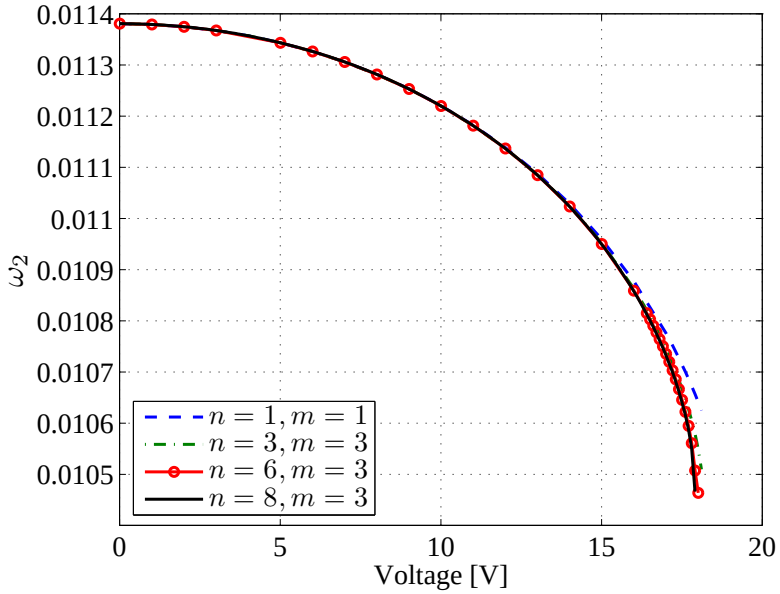

Figure 7.2: Second nondimensional natural frequency ω_2.

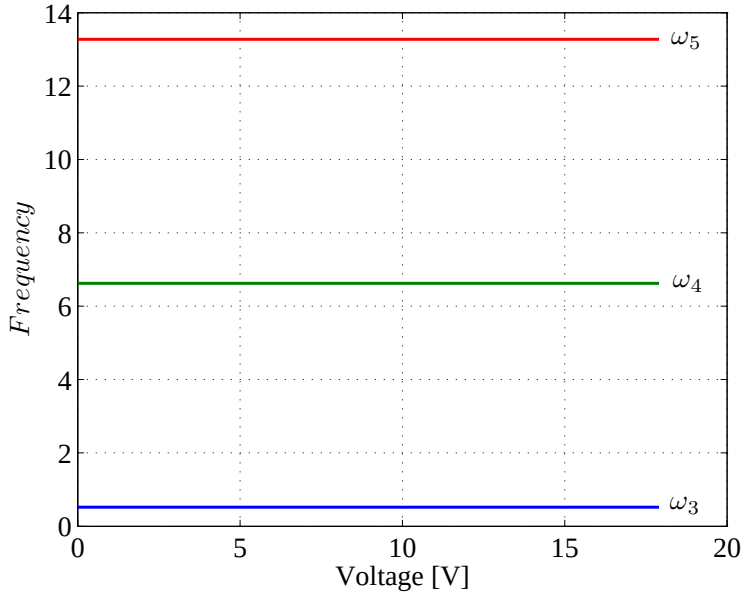

Figure 7.3: Third, fourth, and fifth nondimensional natural frequencies ω_3, ω_4, and ω_5. Here, $n = 8$ and $m = 3$

7.1.2 Mode Shapes

We use Equation (7.4) to calculate the eigenvectors $\mathbb{A}_i$ corresponding to the eigenfrequencies ω_i . The resulting eigenfunction is determined using the following relation:

$$\Psi_i = D_i \begin{pmatrix} \psi_1 & \psi_2 & \dots & \psi_n & \varphi_1 & \varphi_2 & \dots & \varphi_m \end{pmatrix} \begin{pmatrix} A_{i1} \\ A_{i2} \\ A_{i3} \\ \vdots \\ \vdots \\ A_{i(n+m)} \end{pmatrix} \tag{7.6}$$

where the A_{i1} through $A_{i(n+m)}$ are the elements of the eigenvector $\mathbb{A}_i$ and D_i is an arbitrary constant that is determined using the following normalization:

$$\int_0^1 \Psi_i^2 \, d\xi = 1 \qquad i = 1, 2, \dots, n+m. \tag{7.7}$$

Next, we show the evolution of the first four eigenfunctions as the voltage V is increased. Due to symmetry, we only show the eigenfunctions of the left suspension beam. Figure 7.4 shows the evolution of the first eigenfunction Ψ_1. At zero voltage, the eigenfunction Ψ_1 is purely torsional. As the voltage V is increased, coupling between the torsion and bending starts, and the eigenfunction develops a bending component, which starts to grow. This coupling is due to the electrostatic field and is more pronounced for higher voltages. This coupling transfers energy from torsion, in torsion dominant modes, to bending and vice versa.

Similarly, as shown in Fig. 7.5, at zero voltage the eigenfunction Ψ_2 is purely bending. However, as the voltage is increased, coupling between bending and torsion appears and increases gradually, resulting in the appearance and growth of a torsion component of this eigenfunction. Figures 7.6 and 7.7 show the third and fourth eigenfunctions Ψ_3 and Ψ_4, respectively. We note that as the voltage is increased all the way to pull-in, the eigenfunctions remain unchanged and no coupling occurs between torsion and bending.

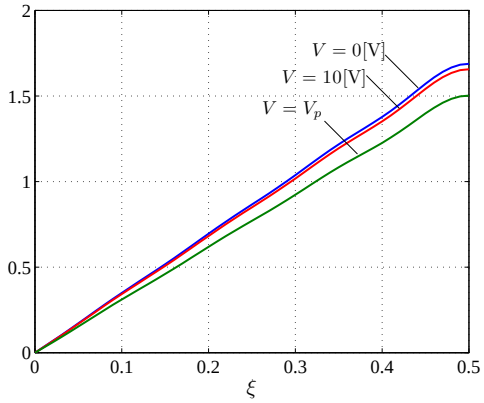

(a) Torsion.

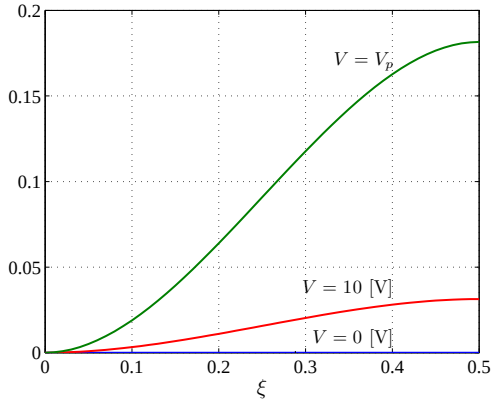

(b) Bending.

Figure 7.4: Evolution of the first eigenfunction Ψ_1 with voltage.

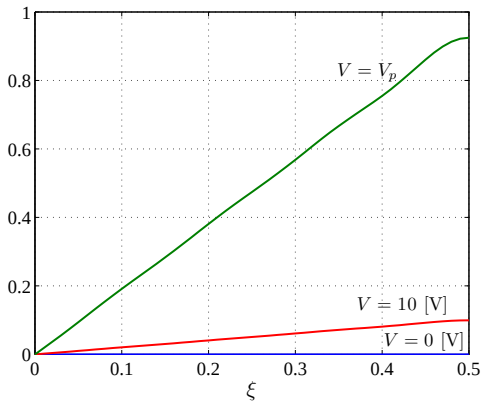

(a) Torsion.

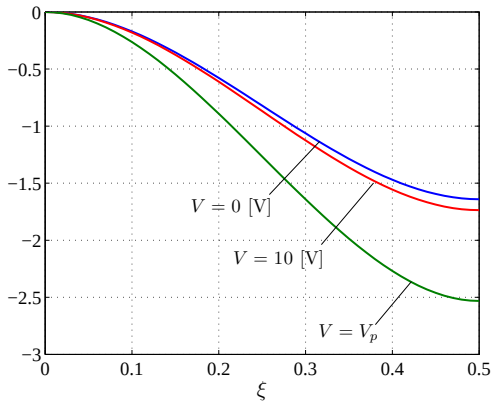

(b) Bending.

Figure 7.5: Evolution of the second eigenfunction Ψ_2 with voltage.

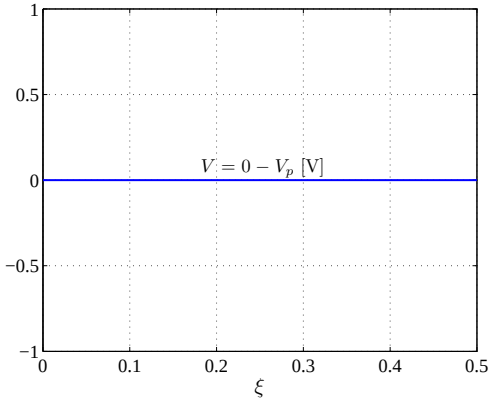

(a) Torsion.

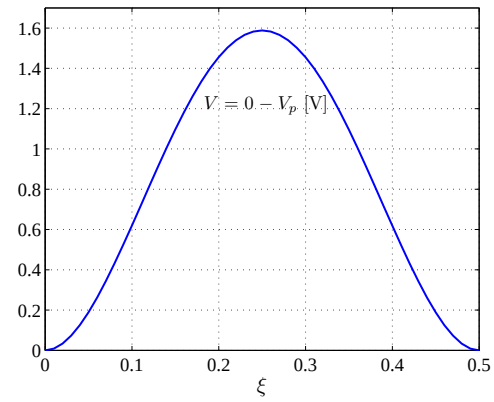

(b) Bending.

Figure 7.6: Evolution of the third eigenfunction Ψ_3 with voltage.

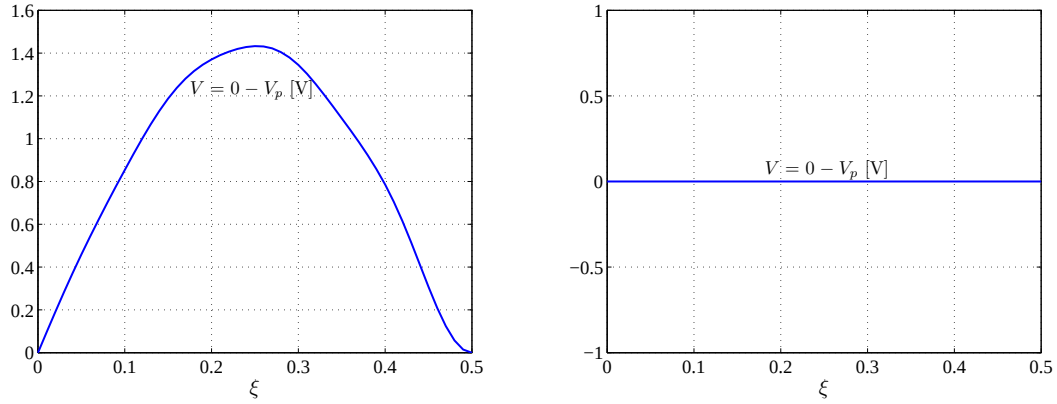

(a) Torsion. (b) Bending.

Figure 7.7: Evolution of the fourth eigenfunction Ψ_4 with voltage.

7.2 Lumped-Mass Model

The eigenvalue problem indicates that the natural frequencies of the higher modes are two orders of magnitude larger than the first two natural frequencies. Further, at zero voltage, the eigenfunctions associated with the lowest two modes are the first torsion and bending modes of the suspension beams. Unless the micromirror is excited at extremely high frequencies, the higher modes are not expected to either capture or transfer energy to the lower frequency modes [88]. Therefore, one can safely assume that, under normal operating conditions, the mirror will respond only in the first two modes. This is a critical finding because it implies that one can treat the micromirror as a lumped mass attached to two springs representing the suspension beams, see Fig. 7.8. The first spring is a torsional spring with stiffness $k_{11} = \frac{2GJ_p}{l}$, and the second is a bending spring with stiffness $k_{22} = \frac{24EI_{b_y}}{l^3}$. The equations of motion for the mirror can therefore be reduced to

$$\begin{bmatrix} m_{11} & 0 \\ 0 & m_{22} \end{bmatrix} \begin{pmatrix} \ddot{\theta} \\ \ddot{u} \end{pmatrix} + \begin{bmatrix} \mu_1 & 0 \\ 0 & \mu_2 \end{bmatrix} \begin{pmatrix} \dot{\theta} \\ \dot{u} \end{pmatrix} + \begin{bmatrix} k_{11} & 0 \\ 0 & k_{22} \end{bmatrix} \begin{pmatrix} \theta \\ u \end{pmatrix} = \begin{pmatrix} \frac{\mathbf{M}_e}{\theta_{cr}} \\ \frac{\mathbf{F}_e + Mg}{d} \end{pmatrix} \tag{7.8}$$

where

$$m_{11} = \frac{I_{m_{zz}}}{T^2} \qquad m_{22} = \frac{M}{T^2} \qquad \mu_1 = 2\zeta_1\sqrt{k_{11}m_{11}} \qquad \mu_2 = 2\zeta_2\sqrt{k_{22}m_{22}}$$

Here, ζ_1 and ζ_2 are the linear modal damping ratios associated with torsion and bending, respectively. Figure 7.9 shows a comparison between the first two natural frequencies obtained using the reduced-order model and those obtained using the lumped-mass model. The figure shows good agreement between the lumped-mass model and the results obtained using the reduced-order model.

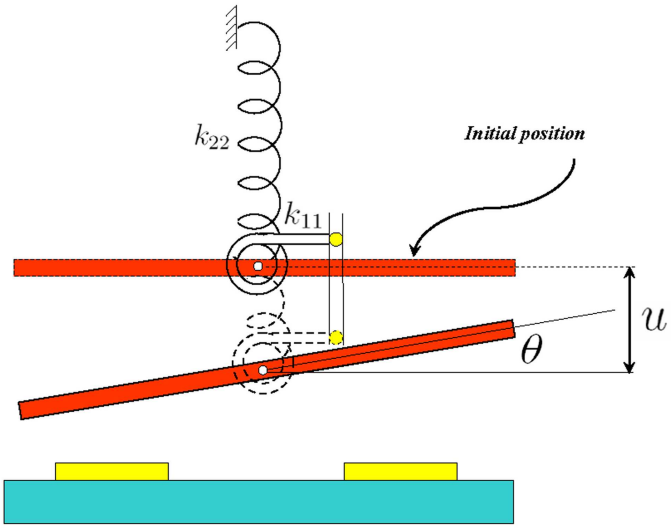

Figure 7.8: Schematic of a lumped-mass model of the micromirror.

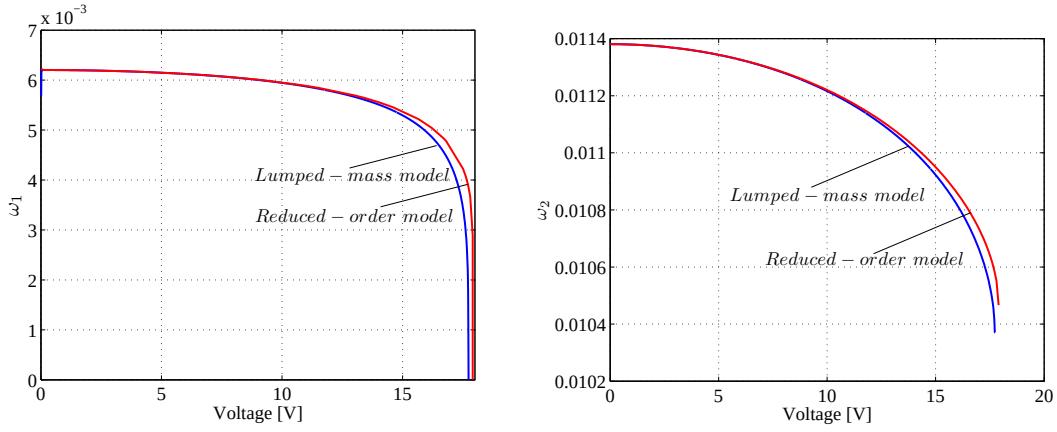

(a) First natural frequency.

(b) Second natural frequency.

Figure 7.9: Comparison between the first two natural frequencies obtained using the lumped-mass model and the reduced-order model.

7.3 Sensitivity of the Natural Frequencies to the Electrode Dimensions

To examine the sensitivity of the first two natural frequencies of the micromirror to changes in the electrode size and position, we plot ω_1 and ω_2 for three values of $\alpha = 0$, 0.15, and 0.3 (Fig. 7.10), as well as three values of $\beta = 0.70$, 0.85, and 1 (Fig. 7.11).

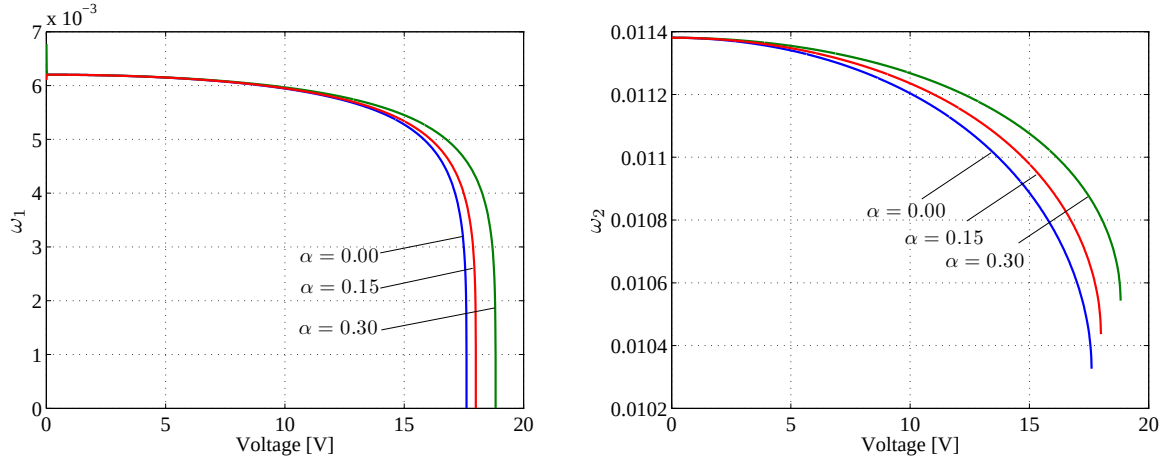

(a) First natural frequency.

(b) Second natural frequency.

Figure 7.10: The first and second natural frequencies for $\alpha = 0, 0.15$, and 0.3.

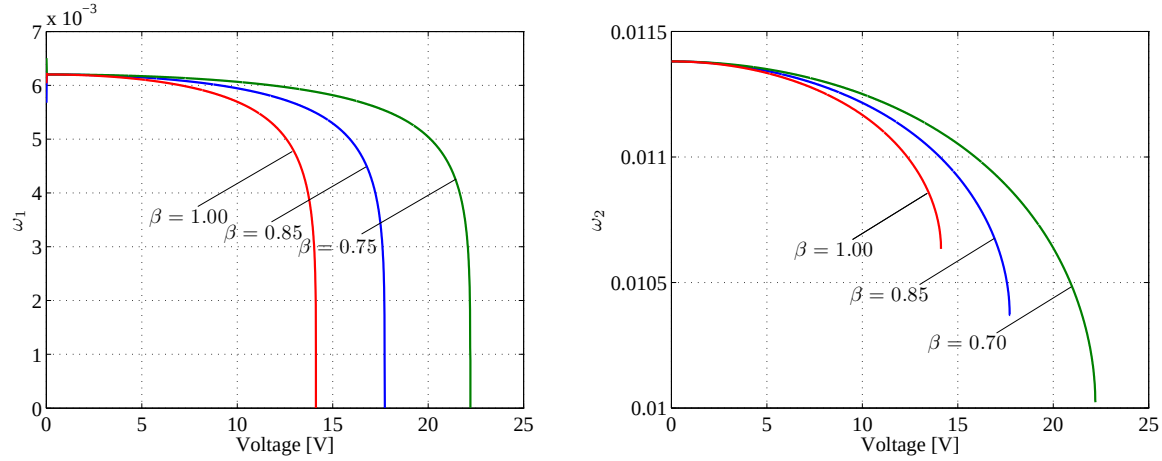

(a) First natural frequency.

(b) Second natural frequency.

Figure 7.11: The first and second natural frequencies for $\beta = 0.7, 0.85$, and 1.

The results show that changing the electrode size, whether through changing α or β, changes the balance between the electrostatic energy and the mechanical energy stored in the suspension beams. Decreasing α or increasing β increases the electrode size and hence increases the negative linear stiffness associated with the electrostatic force and moment. This, in turn, causes the first two natural frequencies to drop faster to pull-in as shown in Figs. 7.10 and 7.11.

It can also be seen from Fig. 7.10 that the second natural frequency is more sensitive to changes in α than the first natural frequency. This stems from the fact that the second natural frequency is associated with bending, as a result it responds to changes in the electrode size. On the other hand, the first natural frequency responds to changes in both the electrode size and center with respect to the axis of rotation. Decreasing α increases the electrode size but decreases the distance from the electrode center to the axis of rotation and hence the moment arm. Therefore, it significantly impacts the electrostatic force but has minimal effect on the electrostatic moment.

On the other hand changing β, which defines the position of the outer side of the electrode, has a significant impact on both of the first and second natural frequencies. This results from the fact that increasing β increases both of the size of the electrode and the moment arm and therefore significantly affects the electrostatic force and moment.

Chapter 8

Response of Torsional Micromirrors to Primary Resonance Excitations Away from Internal Resonances

For light scanning applications, torsional micromirrors or microscanners are excited at their natural frequencies to realize large steady-state scanning angles. Usually, a bias DC voltage is also applied to scan around a desired nonzero tilt angle. As a result, a deep understanding of the mirrors response to a combination of DC and AC primary resonance excitations is necessary. Towards that end, we use the method of multiple scales to obtain a second-order nonlinear approximation of the mirror steady-state response. We find that the response of the mirror exhibits a softening-type behavior that increases as the magnitude of the DC component increases. For the given mirror dimensions and electrode parameters, we identify a region of two-to-one internal resonance between the first two modes. The response of the mirror in that region is treated in details in Chapter 9.

8.1 Primary Resonance Excitation of the First Mode

In this section, we analyze the response of the micromirror to electric excitations consisting of a DC component V_{dc} and an AC component $V_{ac}\cos(\Omega t)$, where Ω is approximately equal to the natural frequency ω_1 of the first mode corresponding to V_{dc}. This analysis is aimed at providing a better understanding of the nonlinear steady-state response of torsional micromirrors used for scanning applications.

We start by expressing the response in the form

$$\begin{aligned} \theta &= \theta_s + \theta_\delta \\ u &= u_s + u_\delta \end{aligned} \tag{8.1}$$

where the subscript s denotes the static part, and the subscript δ denotes the dynamic part. Substituting Equations (8.1) into Equation (7.8), noting that u_s and θ_s satisfy Equations (6.8), and expanding the electrostatic force and moment in Taylor series keeping only terms up to third order in θ_δ and u_δ, we obtain

$$\begin{aligned} m_{11}\ddot{\theta}_\delta + \mu_1\dot{\theta}_\delta + k_{11}\theta_\delta = \Gamma_1 V^2(\alpha_{11}&+\alpha_{12}\theta_\delta + \alpha_{13}u_\delta + \alpha_{14}\theta_\delta u_\delta + \alpha_{15}\theta_\delta^2 + \alpha_{16}u_\delta^2 + \alpha_{17}\theta_\delta u_\delta^2 \\ &+\alpha_{18}\theta_d^2 u_\delta + \alpha_{19}\theta_\delta^3 + \alpha_{110}u_\delta^3) \\ m_{22}\ddot{u}_\delta + \mu_2\dot{u}_\delta + k_{22}u_\delta = \Gamma_2 V^2(\alpha_{21}&+\alpha_{22}\theta_\delta + \alpha_{23}u_\delta + \alpha_{24}\theta_\delta u_\delta + \alpha_{25}\theta_\delta^2 + \alpha_{26}u_\delta^2 + \alpha_{27}\theta_\delta u_\delta^2 \\ &+\alpha_{28}\theta_\delta^2 u_\delta + \alpha_{29}\theta_\delta^3 + \alpha_{210}u_\delta^3) \end{aligned} \tag{8.2}$$

where

$$\Gamma_1 = \frac{\epsilon b}{2\theta_{cr}^3}, \qquad \Gamma_2 = \frac{\epsilon b}{2d^2\theta_{cr}}. \tag{8.3}$$

and the α_{ij} are the coefficients resulting from the Taylor series expansions. We scale the dependent variables such that the effect of the nonlinearity balances the effects of the damping and AC excitation. In other words, we let

$$V = V_{dc} + \varepsilon^3 V_{ac}\cos(\Omega t), \qquad \mu_1 = \varepsilon^2\mu_1, \qquad \mu_2 = \varepsilon^2\mu_2, \qquad \Omega = \omega_1 + \varepsilon^2\sigma. \tag{8.4}$$

where ε is a small nondimensional bookkeeping parameter and σ is a detuning parameter. The time dependence t is expanded in terms of multiple time scales [86] as

$$\begin{aligned}\frac{d}{dt} =& D_0 + \varepsilon D_1 + \varepsilon^2 D_2 + \dots \\ \frac{d^2}{dt^2} =& D_0^2 + 2\varepsilon D_0 D_1 + \varepsilon^2 D_1 + 2\varepsilon^2 D_0 D_2 + \dots\end{aligned} \tag{8.5}$$

where $t = \varepsilon^n T_n$ and $D_n = \frac{\partial}{\partial T_n}$. We seek a solution of Equations (8.2) in the form

$$\begin{aligned}\theta_\delta &= \varepsilon\theta_0(T_0, T_1, T_2) + \varepsilon^2\theta_1(T_0, T_1, T_2) + \varepsilon^3\theta_2(T_0, T_1, T_2) + \dots \\ u_\delta &= \varepsilon u_0(T_0, T_1, T_2) + \varepsilon^2 u_1(T_0, T_1, T_2) + \varepsilon^3 u_2(T_0, T_1, T_2) + \dots\end{aligned} \tag{8.6}$$

Substituting Equations (8.4)-(8.6) into Equations (8.2) and equating coefficients of like powers of ε, we obtain

$\underline{O(\varepsilon):}$

$$\begin{aligned} m_{11}D_0^2\theta_0 + (k_{11} - V_{dc}^2\Gamma_1\alpha_{12})\theta_0 - V_{dc}^2\Gamma_1\alpha_{13}u_0 = 0 \\ m_{22}D_0^2 u_0 + (k_{22} - V_{dc}^2\Gamma_2\alpha_{23})u_0 - V_{dc}^2\Gamma_2\alpha_{22}\theta_0 = 0\end{aligned} \tag{8.7a}$$

$\underline{O(\varepsilon^2):}$

$$\begin{aligned} m_{11}D_0^2\theta_1 + (k_{11} - V_{dc}^2\Gamma_1\alpha_{12})\theta_1 - V_{dc}^2\Gamma_1\alpha_{13}u_1 = -2m_{11}D_0D_1\theta_0 \\ + V_{dc}^2\Gamma_1(\alpha_{15}\theta_0^2 + \alpha_{14}\theta_0u_0 + \alpha_{16}u_0^2) \\ m_{22}D_0^2u_1 + (k_{22} - V_{dc}^2\Gamma_2\alpha_{23})u_1 - V_{dc}^2\Gamma_2\alpha_{22}\theta_1 = -2m_{22}D_0D_1u_0 \\ + V_{dc}^2\Gamma_2(\alpha_{25}\theta_0^2 + \alpha_{24}\theta_0u_0 + \alpha_{26}u_0^2)\end{aligned} \tag{8.7b}$$

$\underline{O(\varepsilon^3):}$

$$
\begin{aligned}
m_{11}D_0^2\theta_2 + \left(k_{11} - V_{dc}^2\Gamma_1\alpha_{12}\right)\theta_2 - V_{dc}^2\Gamma_1\alpha_{13}u_2 &= -\mu_1 D_0\theta_0 - m_{11}(2D_0D_1\theta_1 - D_1^2\theta_0 - 2D_0D_2\theta_0) \\
&+ V_{dc}V_{ac}\alpha_{11}\Gamma_1\left(e^{-iT_0\varepsilon^2\sigma - iT_0\omega_1} + e^{iT_0\varepsilon^2\sigma + iT_0\omega_1}\right) + V_{dc}^2\Gamma_1(\alpha_{19}\theta_0^3 + 2\alpha_{15}\theta_0\theta_1 \\
&+ \alpha_{18}\theta_0^2u_0 + \alpha_{14}\theta_1u_0 + \alpha_{17}\theta_0u_0^2 + \alpha_{110}u_0^3 + \alpha_{14}\theta_0u_1 + 2\alpha_{16}u_0u_1) \\
m_{22}D_0^2u_2 + \left(k_{22} - V_{dc}^2\Gamma_2\alpha_{23}\right)u_2 - V_{dc}^2\Gamma_2\alpha_{22}\theta_2 &= -\mu_2 D_0u_0 - m_{22}(2D_0D_1u_1 - D_1^2u_0 - 2D_0D_2\theta_0) \\
&+ V_{dc}V_{ac}\alpha_{21}\Gamma_1\left(e^{-iT_0\varepsilon^2\sigma - iT_0\omega_1} + e^{iT_0\varepsilon^2\sigma + iT_0\omega_1}\right) + V_{dc}^2\Gamma_2(\alpha_{29}\theta_0^3 + 2\alpha_{25}\theta_0\theta_1 \\
&+ \alpha_{28}\theta_0^2u_0 + \alpha_{24}\theta_1u_0 + \alpha_{27}\theta_0u_0^2 + \alpha_{210}u_0^3 + \alpha_{24}\theta_0u_1 + 2\alpha_{26}u_0u_1))
\end{aligned}
\tag{8.7c}
$$

Equations (8.7a) constitute a system of two linearly coupled differential equations with constant coefficients. Their solution can be written as

$$
\begin{bmatrix} \theta_0 \\ u_0 \end{bmatrix} = \begin{bmatrix} 1 \\ k_1 \end{bmatrix} A_1(T_1, T_2)e^{i\omega_1 T_0} + \begin{bmatrix} 1 \\ k_2 \end{bmatrix} A_2(T_1, T_2)e^{i\omega_2 T_0} + cc \tag{8.8}
$$

where cc stands for the complex conjugate of the preceding term. The eigenfrequencies ω_1 and ω_2 are obtained from the solution of the following characteristic equation

$$
\mathcal{D}(\omega) = \omega^4 + B\omega^2 + C = 0 \tag{8.9}
$$

where

$$
\begin{aligned}
B &= \frac{1}{m_{11}m_{22}}\left[V_{dc}^2(\Gamma_1\alpha_{12}m_{22} + \Gamma_2\alpha_{23}m_{11}) - k_{11}m_{22} - k_{22}m_{11}\right], \\
C &= \frac{1}{m_{11}m_{22}}\left[V_{dc}^4\Gamma_1\Gamma_2(\alpha_{23}\alpha_{12} - \alpha_{13}\alpha_{22}) - V_{dc}^2(k_{11}\Gamma_2\alpha_{23} + k_{22}\Gamma_1\alpha_{12}) + k_{11}k_{22}\right].
\end{aligned}
$$

and

$$
k_n = \frac{\alpha_{22}\Gamma_2V_{dc}^2}{k_{22} - V_{dc}^2\alpha_{23}\Gamma_2 - m_{22}\omega_n^2}, \qquad n = 1, 2.
$$

Substituting Equation (8.8) into Equation (8.7b) yields

$$
\begin{aligned}
m_{11}D_0^2\theta_1 + (k_{11} - V_{dc}^2\Gamma_1\alpha_{12})\theta_1 - V_{dc}^2\Gamma_1\alpha_{13}u_1 &= -2im_{11}\omega_1 D_1 A_1 e^{i\omega_1 T_0} - 2im_{22}\omega_2 D_1 A_2 e^{i\omega_2 T_0} \\
&\quad + b_{11}A_1^2(T_1,T_2)e^{2i\omega_1 T_0} + b_{12}A_2^2(T_1,T_2)e^{2i\omega_2 T_0} \\
&\quad + b_{13}A_1(T_1,T_2)A_2(T_1,T_2)e^{i(\omega_1+\omega_2)T_0} \\
&\quad + b_{14}A_1(T_1,T_2)\bar{A}_2(T_1,T_2)e^{i(\omega_1-\omega_2)T_0} \\
&\quad + b_{151}A_1(T_1,T_2)\bar{A}_1(T_1,T_2) \\
&\quad + b_{152}A_2(T_1,T_2)\bar{A}_2(T_1,T_2) + cc \\
m_{22}D_0^2 u_1 + (k_{22} - V_{dc}^2\Gamma_2\alpha_{23})u_1 - V_{dc}^2\Gamma_2\alpha_{22}\theta_1 &= -2im_{11}k_1\omega_1 D_1 A_1 e^{i\omega_1 T_0} - 2im_{22}\omega_2 k_2 D_1 A_2 e^{i\omega_2 T_0} \\
&\quad + b_{21}A_1^2(T_1,T_2)e^{2i\omega_1 T_0} + b_{22}A_2^2(T_1,T_2)e^{2i\omega_2 T_0} \\
&\quad + b_{23}A_1(T_1,T_2)A_2(T_1,T_2)e^{i(\omega_1+\omega_2)T_0} \\
&\quad + b_{24}A_1(T_1,T_2)\bar{A}_2(T_1,T_2)e^{i(\omega_1-\omega_2)T_0} \\
&\quad + b_{251}A_1(T_1,T_2)\bar{A}_1(T_1,T_2) \\
&\quad + b_{252}A_2(T_1,T_2)\bar{A}_2(T_1,T_2) + cc
\end{aligned}
\tag{8.10}
$$

where $\bar{A}_n$ is the complex conjugate of A_n and

$$
\begin{aligned}
b_{n1} &= V_{dc}^2\Gamma_n(k_1\alpha_{n4} + \alpha_{n5} + k_1^2\alpha_{n6}), \\
b_{n2} &= V_{dc}^2\Gamma_n(k_2\alpha_{n4} + \alpha_{n5} + k_2^2\alpha_{n6}), \\
b_{n3} &= V_{dc}^2\Gamma_n((k_1+k_2)\alpha_{n4} + 2\alpha_{n5} + 2k_1k_2\alpha_{n6}), \\
b_{n4} &= b_{n3}, \qquad b_{15n} = 2b_{1n}, \qquad b_{25n} = 2b_{2n}, \qquad n = 1, 2.
\end{aligned}
\tag{8.11}
$$

The forcing terms proportional to $e^{\pm i\omega_1 T_0}$ and $e^{\pm i\omega_2 T_0}$ will produce secular terms in θ_1 and u_1. To eliminate these secular terms and hence determine the solvability conditions, we seek a particular solution free of secular terms in the form

$$
\theta_1 = P_1 e^{i\omega_1 T_0} + P_2 e^{i\omega_2 T_0}, \qquad u_1 = Q_1 e^{i\omega_1 T_0} + Q_2 e^{i\omega_2 T_0} \tag{8.12}
$$

Substituting Equations (8.12) into Equations (8.10) and equating the coefficients of each of

$e^{i\omega_1 T_0}$ and $e^{i\omega_2 T_0}$ on both sides of the equations, we obtain

$$\begin{aligned}
\begin{bmatrix} \Delta_1(\omega_1) & -\alpha_{13}\Gamma_1 V_{dc}^2 \\ -\alpha_{22}\Gamma_2 V_{dc}^2 & \Delta_2(\omega_1) \end{bmatrix} \begin{pmatrix} P_1 \\ Q_1 \end{pmatrix} &= \begin{bmatrix} -2im_{11}\omega_1 D_1 A_1 \\ -2im_{11}k_1\omega_1 D_1 A_1 \end{bmatrix} \\
\begin{bmatrix} \Delta_1(\omega_2) & -\alpha_{13}\Gamma_1 V_{dc}^2 \\ -\alpha_{22}\Gamma_2 V_{dc}^2 & \Delta_2(\omega_2) \end{bmatrix} \begin{pmatrix} P_2 \\ Q_2 \end{pmatrix} &= \begin{bmatrix} -2im_{22}\omega_2 D_1 A_2 \\ -2im_{22}k_2\omega_2 D_1 A_2 \end{bmatrix}
\end{aligned} \tag{8.13}$$

where

$$\Delta_1(\omega) = k_{11} - \alpha_{12}V_{dc}^2 - m_{11}\omega^2, \qquad \Delta_2(\omega) = k_{22} - \alpha_{23}V_{dc}^2 - m_{22}\omega^2. \tag{8.14}$$

Because each set of Equations (8.13) constitutes a system of two inhomogeneous algebraic equations whose homogeneous parts have a nontrivial solution according to Equation (8.8), their solvability conditions can be written as

$$\begin{aligned}
\begin{vmatrix} \Delta_1(\omega_1) & -2im_{11}\omega_1 D_1 A_1 \\ -\alpha_{22}\Gamma_2 V_{dc}^2 & -2im_{11}k_1\omega_1 D_1 A_1 \end{vmatrix} &= 0 \\
\begin{vmatrix} \Delta_1(\omega_2) & -2im_{22}\omega_2 D_1 A_2 \\ -\alpha_{22}\Gamma_2 V_{dc}^2 & -2im_{22}k_2\omega_2 D_1 A_2 \end{vmatrix} &= 0
\end{aligned} \tag{8.15}$$

These two conditions lead to

$$D_1 A_1 = 0 \Longrightarrow A_1 = A_1(T_2), \qquad D_1 A_2 = 0 \Longrightarrow A_2 = A_2(T_2). \tag{8.16}$$

Then the particular solution of Equation (8.10) can be written as

$$\begin{aligned}
\theta_1 =& c_{11}A_1^2(T_2)e^{2i\omega_1 T_0} + c_{12}A_2^2(T_2)e^{2i\omega_2 T_0} + c_{13}A_1(T_2)A_2(T_2)e^{i(\omega_1+\omega_2)T_0} \\
&+ c_{14}A_1(T_2)\bar{A}_2(T_1)e^{i(\omega_1-\omega_2)T_0} + c_{151}A_1(T_2)\bar{A}_1(T_2) + c_{152}A_2(T_2)\bar{A}_2(T_2) + cc \\
u_1 =& c_{21}A_1^2(T_2)e^{2i\omega_1 T_0} + c_{22}A_2^2(T_2)e^{2i\omega_2 T_0} + c_{23}A_1(T_2)A_2(T_2)e^{i(\omega_1+\omega_2)T_0} \\
&+ c_{24}A_1(T_2)\bar{A}_2(T_1)e^{i(\omega_1-\omega_2)T_0} + c_{251}A_1(T_2)\bar{A}_1(T_2) + c_{252}A_2(T_2)\bar{A}_2(T_2) + cc
\end{aligned} \tag{8.17}$$

where

$$
\begin{aligned}
c_{1n} &= \frac{b_{n2}[\mathcal{D}(2\omega_n) + \Delta_1(2\omega_n)\Delta_2(2\omega_n)] + b_{n1}\Delta_2(2\omega_n)\Gamma_2\alpha_{22}V_{dc}^2}{V_{dc}^2\alpha_{22}\Gamma_2\mathcal{D}(2\omega_n)},\\
c_{2n} &= \frac{b_{n1}\Gamma_2\alpha_{22}V_{dc}^2 + b_{n2}\Delta_1(2\omega_n)}{\mathcal{D}(2\omega_n)},\\
c_{13} &= \frac{b_{23}\mathcal{D}(\omega_1+\omega_2) + \Delta_2(\omega_1+\omega_2)(\Gamma_2\alpha_{22}b_{13}V_{dc}^2 + b_{23}\Delta_1(\omega_1+\omega_2)^2)}{V_{dc}^2\alpha_{22}\Gamma_2\mathcal{D}(\omega_1+\omega_2)},\\
c_{14} &= \frac{b_{24}\mathcal{D}(\omega_1-\omega_2) + \Delta_2(\omega_1-\omega_2)(\Gamma_2\alpha_{22}b_{14}V_{dc}^2 + b_{24}\Delta_1(\omega_1-\omega_2)^2)}{V_{dc}^2\alpha_{22}\Gamma_2\mathcal{D}(\omega_1-\omega_2)},\\
c_{23} &= \frac{\Gamma_2\alpha_{22}b_{13}V_{dc}^2 + b_{23}\Delta_1(\omega_1+\omega_2)^2}{\mathcal{D}(\omega_1+\omega_2)},\\
c_{24} &= \frac{\Gamma_2\alpha_{22}b_{14}V_{dc}^2 + b_{24}\Delta_1(\omega_1-\omega_2)^2}{\mathcal{D}(\omega_1-\omega_2)},\\
c_{15n} &= \frac{b_{15n}\Delta_2(0) + \alpha_{13}\Gamma_1V_{dc}^2b_{25n}}{\mathcal{D}(0)},\\
c_{25n} &= -\frac{b_{15n}\Delta_1(0) - \alpha_{22}\Gamma_2V_{dc}^2b_{15n}}{\mathcal{D}(0)}, \qquad n=1,2.
\end{aligned}
\tag{8.18}
$$

In a similar fashion, we substitute Equations (8.8), (8.16), and (8.17) into Equation (8.7c), eliminate the terms that produce secular terms by enforcing the solvability conditions, and obtain the following two first-order-ordinary-differential equations for A_1 and A_2:

$$
\begin{aligned}
2i\omega_1\Lambda_{11}D_2A_1 &= i\omega_1\Lambda_{12}A_1 + \Lambda_{13}V_{ac}e^{i\sigma T_2} + \Lambda_{14}A_1^2\bar{A}_1 + \Lambda_{15}A_1A_2\bar{A}_2\\
2i\omega_2\Lambda_{21}D_2A_2 &= i\omega_2\Lambda_{22}A_2 + \Lambda_{24}A_2^2\bar{A}_2 + \Lambda_{25}A_2A_1\bar{A}_1
\end{aligned}
\tag{8.19}
$$

where

$$
\begin{aligned}
&\Lambda_{n1} = k_nm_{22}\Delta_1(\omega_n) - \alpha_{22}\Gamma_2m_{11}V_{dc}^2, && \Lambda_{n2} = k_n\mu_2\Delta_1(\omega_n) - \alpha_{22}\Gamma_2\mu_1V_{dc}^2,\\
&\Lambda_{n3} = V_{dc}(\Gamma_2\alpha_{21}\Delta_1(\omega_n) - \alpha_{22}\alpha_{11}\Gamma_1\Gamma_2V_{dc}^2),\\
&\Lambda_{14} = -V_{dc}^2(\Delta_1(\omega_1)Z_2 - \Gamma_2\alpha_{22}V_{dc}^2Z_1), && \Lambda_{24} = -V_{dc}^2(\Delta_1(\omega_1)\tilde{Z}_2 - \Gamma_2\alpha_{22}V_{dc}^2\tilde{Z}_1),\\
&\Lambda_{15} = -V_{dc}^2(\Delta_1(\omega_1)Y_2 - \Gamma_2\alpha_{22}V_{dc}^2Y_1), && \Lambda_{25} = -V_{dc}^2(\Delta_1(\omega_1)\tilde{Y}_2 - \Gamma_2\alpha_{22}V_{dc}^2\tilde{Y}_1).
\end{aligned}
\tag{8.20}
$$

and

$$
\begin{aligned}
Z_n &= \Gamma_n[2c_{151}(\alpha_{n4}+2\alpha_{n5})+2c_{251}(\alpha_{n4}+2k_1\alpha_{n6})+3(k_1^3\alpha_{n10}+k_1^2\alpha_{n7}+k_1\alpha_{n8}+\alpha_{n9})],\\
\tilde{Z}_n &= \Gamma_n[2c_{152}(\alpha_{n4}+2\alpha_{n5})+2c_{252}(\alpha_{n4}+2k_2\alpha_{n6})+3(k_2^3\alpha_{n10}+k_2^2\alpha_{n7}+k_2\alpha_{n8}+\alpha_{n9})],\\
Y_n &= \Gamma_n[\alpha_{n4}(c_{23}+2c_{152}+2c_{151}k_1+k_2c_{13})+\alpha_{n5}(2c_{22}+4c_{152})+\alpha_{n6}(2c_{23}k_2+4c_{252}k_1)\\
&\quad +\alpha_{n7}(2k_2^2+4k_2k_1)+\alpha_{n8}(4k_2+2k_1)+6\alpha_{n9}+\alpha_{n10}(6k_2^2k_1)],\\
\tilde{Y}_n &= \Gamma_n[\alpha_{n4}(c_{23}+2c_{251}+2c_{151}k_2+k_1c_{13})+\alpha_{n5}(2c_{13}+4c_{151})+\alpha_{n6}(2c_{23}k_1+4c_{251}k_2)\\
&\quad +\alpha_{n7}(2k_2^1+4k_1k_2)+\alpha_{n8}(4k_1+2k_2)+6\alpha_{n9}+\alpha_{n10}(6k_1^2k_2)], \qquad n=1,2.
\end{aligned}
\tag{8.21}
$$

We express A_1 and A_2 in the polar form

$$
A_n = \frac{1}{2}a_n e^{i\beta_n}, \qquad n=1,2. \tag{8.22}
$$

where a_n and β_n are real, then substitute Equations (8.22) into Equations (8.19), separate Equations (8.19) into real and imaginary parts and obtain the following four modulation equations:

$$
\begin{aligned}
2\omega_1\Lambda_{11}a_1' &= \omega_1\Lambda_{12}a_1 + 2\Lambda_{13}V_{ac}\sin(\gamma)\\
2\omega_1\Lambda_{11}a_1(\gamma'-\sigma a_1) &= -\frac{1}{4}(8\Lambda_{13}V_{ac}\cos(\gamma)+\Lambda_{14}a_1^3+\Lambda_{15}a_1a_2^2)\\
2\Lambda_{21}a_2' &= \Lambda_{22}a_2\\
2\omega_2\Lambda_{21}a_2\beta_2' &= -\frac{1}{4}(\Lambda_{24}a_1^3+\Lambda_{25}a_2a_1^2)
\end{aligned}
\tag{8.23}
$$

where the primes indicate derivatives with respect to T_2, and $\gamma = \sigma T_2 - \beta_1$.

We analyze the long-time dynamics of the micromirror by studying the equilibrium solutions of Equations (8.23). To realize clear images, the micromirror or the microscanner is designed to scan periodically. Therefore, we concentrate our analysis on the equilibrium solutions of the modulation equations and their stability. For positive modal damping $\Lambda_{22}/\Lambda_{21} < 0$, therefore a_2 goes to zero as T_2 goes to infinity and hence as t goes to infinity. As a result, Equations (8.23) reduce to

$$\begin{aligned} 2\omega_1\Lambda_{11}a_1' &= \omega_1\Lambda_{12}a_1 + 2\Lambda_{13}V_{ac}\sin(\gamma) \\ 2\omega_1\Lambda_{11}a_1(\gamma' - \sigma) &= -\frac{1}{4}(8\Lambda_{13}V_{ac}\cos(\gamma) + \Lambda_{14}a_1^3) \\ a_2 &= 0 \end{aligned} \tag{8.24}$$

We obtain the equilibrium solutions by setting the time derivatives equal to zero in Equations (8.24) and obtaining

$$\begin{aligned} -\frac{\omega_1\Lambda_{12}}{2\Lambda_{13}}a_1 &= V_{ac}\sin(\gamma) \\ \frac{\omega_1\Lambda_{11}\sigma}{\Lambda_{13}}a_1 - \frac{\Lambda_{14}}{8\Lambda_{13}}a_1^3 &= V_{ac}\cos(\gamma) \\ a_2 &= 0 \end{aligned} \tag{8.25}$$

Squaring and adding Equations (8.25) yields

$$\frac{\omega_1^2\Lambda_{12}^2}{4\Lambda_{13}^2}a_1^2 + \left[\frac{\omega_1\Lambda_{11}}{\Lambda_{13}}\sigma a_1 - \frac{\Lambda_{14}}{8\Lambda_{13}}a_1^3\right]^2 - V_{ac}^2 = 0 \tag{8.26}$$

Using Equation (8.26), one can analyze variation of the response amplitude with the frequency detuning parameter σ and the applied AC voltage V_{ac}.

8.2 Stability of the Equilibrium Solutions

The stability of the equilibrium solutions is determined by finding the eigenvalues of the Jacobian matrix of the modulation equations evaluated at this equilibrium solution. If all of the eigenvalues associated with the equilibrium solution have negative real parts then the solution is asymptotically stable. Otherwise, if one eigenvalue has a positive real part then, the solution is unstable. Following Nayfeh [89], we determine an analytical condition for the stability of the resulting equilibrium solutions. To this end, we let

$$a_1 = a_0 + a_d \qquad \gamma = \gamma_0 + \gamma_d \tag{8.27}$$

Substituting Equations (8.27) into Equations (8.24), expanding the result for small a_d and γ_d, noting that a_0 and γ_0 satisfy the right-hand sides of Equations (8.24), and keeping only linear terms in a_d and γ_d, we obtain

$$\begin{pmatrix} a_d' \\ \gamma_d' \end{pmatrix} = \begin{bmatrix} \frac{\Lambda_{12}}{2\Lambda_{11}} & \frac{\Lambda_{13}}{\omega_1\Lambda_{11}}\cos\gamma_0 \\ -\frac{\Lambda_{14}}{4\omega_1\Lambda_{11}}a_0 + \frac{\Lambda_{13}}{\omega_1\Lambda_{11}a_0^2}\cos\gamma_0 & \frac{\Lambda_{13}}{\omega_1\Lambda_{11}a_0}\sin\gamma_0 \end{bmatrix} \begin{pmatrix} a_d \\ \gamma_d \end{pmatrix} \tag{8.28}$$

Substituting for $\cos\gamma_0$ and $\sin\gamma_0$ using Equations (8.25), we obtain

$$\begin{pmatrix} a_d' \\ \gamma_d' \end{pmatrix} = \begin{bmatrix} \frac{\Lambda_{12}}{2\Lambda_{11}} & -a_0\left(\sigma + \frac{\Lambda_{14}}{8\omega_1\Lambda_{11}a_0^2}\right) \\ \frac{1}{a_0}\left(\sigma + \frac{3\Lambda_{14}}{8\omega_1\Lambda_{11}}a_0^2\right) & \frac{\Lambda_{12}}{2\Lambda_{11}} \end{bmatrix} \begin{pmatrix} a_d \\ \gamma_d \end{pmatrix} \tag{8.29}$$

The stability of an equilibrium solution depends on the eigenvalues of the coefficient matrix of Equation (8.30). For asymptotically stable solutions, the two eigenvalues must have negative real parts. These eigenvalues λ can be determined from

$$\begin{vmatrix} \frac{\Lambda_{12}}{2\Lambda_{11}} - \lambda & -a_0\left(\sigma + \frac{\Lambda_{14}}{8\omega_1\Lambda_{11}a_0^2}\right) \\ \frac{1}{a_0}\left(\sigma + \frac{3\Lambda_{14}}{8\omega_1\Lambda_{11}}a_0^2\right) & \frac{\Lambda_{12}}{2\Lambda_{11}} - \lambda \end{vmatrix} = 0 \tag{8.30}$$

Expanding the determinant yields

$$\lambda^2 - \frac{\Lambda_{12}}{\Lambda_{11}}\lambda + \frac{\Lambda_{12}^2}{4\Lambda_{11}^2} + \left(\sigma + \frac{\Lambda_{14}}{8\omega_1\Lambda_{11}a_0^2}\right)\left(\sigma + \frac{3\Lambda_{14}}{8\omega_1\Lambda_{11}}a_0^2\right) = 0 \tag{8.31}$$

Hence, an equilibrium solution is asymptotically stable when

$$\frac{\Lambda_{12}^2}{4\Lambda_{11}^2} + \left(\sigma + \frac{\Lambda_{14}}{8\omega_1\Lambda_{11}a_0^2}\right)\left(\sigma + \frac{3\Lambda_{14}}{8\omega_1\Lambda_{11}}a_0^2\right) > 0 \tag{8.32}$$

8.3 Numerical Results

Using Equations (8.26) and (8.32), we study variation of the first mode amplitude a_1 with the excitation frequency detuning parameter σ for different DC voltages V_{dc} and a fixed excitation amplitude $V_{ac} = 0.2$ V. Figure 8.1 illustrates that, as the DC voltage is increased, the

effective nonlinearity increases, and the curves bend towards the left, indicating a softening-type behavior. The softening nonlinearity results in multiple stable solutions at excitation frequencies very close but less than the natural frequency of the first mode. Operating the mirror in that region can cause abrupt jumps in the mirror response, thereby deteriorating the scanner performance. This softening nonlinearity of the mirror is also clear in Fig. 8.2, which indicates that the effective nonlinearity is always negative for all values of V_{dc} through pull-in. Figure 8.2 also shows that the effective nonlinearity is very small and hence has minimal effect on the response for small values of V_{dc}. However, as V_{dc} increases, the effective nonlinearity increases slightly initially and significantly near pull-in. In the vicinity of $V_{dc} = 13.2$ V, the effective nonlinearity has a discontinuity and the single-mode perturbation analysis fails to provide an accurate solution due to the existence of a two-to-one internal resonance between the first two modes ($\omega_2 \approx 2\omega_1$). The internal resonance is manifested by the presence of small divisor terms in the second-order expansion; it is treated in details in the next Chapter.

Figure 8.3 shows variation of the response amplitude a_1 with the frequency detuning parameter σ for different values of V_{ac} and a fixed value of the DC voltage $V_{dc} = 15$ V. As the AC voltage V_{ac} is increased, the response amplitude a_1 increases, and the frequency-response curves bend more towards the left, indicating an increased influence of the softening nonlinearity. This is also clear in Fig. 8.4 where we study the evolution of the response amplitude a_1 with the applied AC voltage V_{ac} for a DC voltage $V_{dc} = 15$ V and a detuning parameter $\sigma = -0.00025$. As V_{ac} is gradually increased, the response amplitude slowly increases until it reaches a critical value $V_{ac} \approx 0.33$ V. At this critical voltage, a saddle-node bifurcation occurs, at which a jump to the closest stable solution takes place with an accompanying sudden increase in a_1, after which a_1 continues to increase slowly. If the process is reversed, a_1 decreases slowly until a saddle-node bifurcation occurs at $V_{ac} \approx 0.21$ V, where a_1 jumps to the the closest stable solution, and the amplitude of the mirror response decreases suddenly. A further decrease in V_{ac} results in a gradual decrease in the response amplitude.

To examine the effect of the electrode parameters on the nonlinear behavior of the micromirror, we plot in Fig. 8.5 the effective nonlinearity for different electrode parameters α and

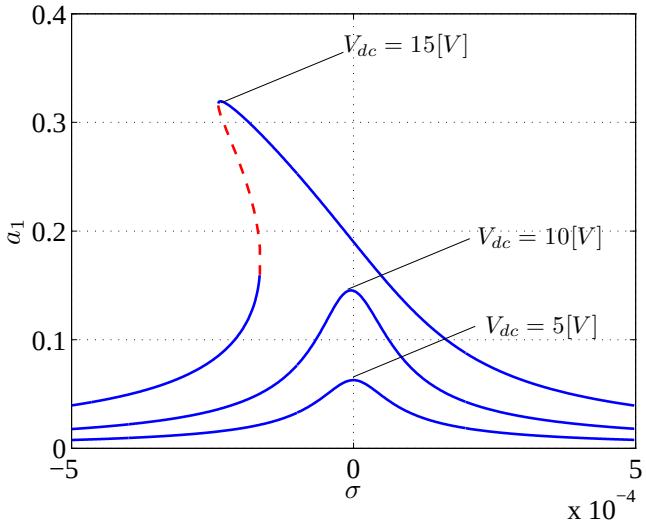

Figure 8.1: Frequency-response curves for $V_{ac} = 0.2$ V and a quality factor $Q = 50$. The dashed lines (- - -) represent unstable solutions.

β. In addition to the previously shown increase in the negative linear stiffness associated with the electrostatic force and moment, the effective nonlinear stiffness also increases, which results in a significant increase in the effective softening nonlinearity. In agreement with the

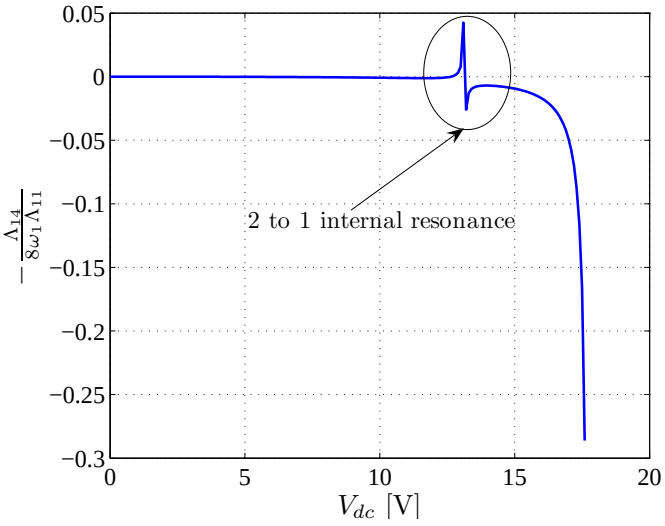

Figure 8.2: Magnitude of the effective nonlinearity associated with the first mode.

linear analysis, the softening effective nonlinearity is more sensitive to changes in β than to changes in α. This stems from two factors. First, the first natural frequency ω_1 is more sensitive to changes in β than to changes in α. Hence, Fig. 7.11 shows that when β is chang-

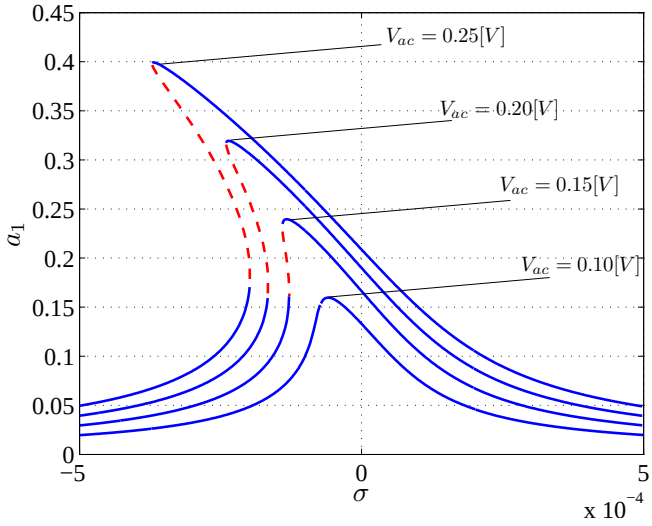

Figure 8.3: Frequency-response curves for $V_{dc} = 15$ V and $Q = 50$. The dashed lines (- - -) represent unstable solutions.

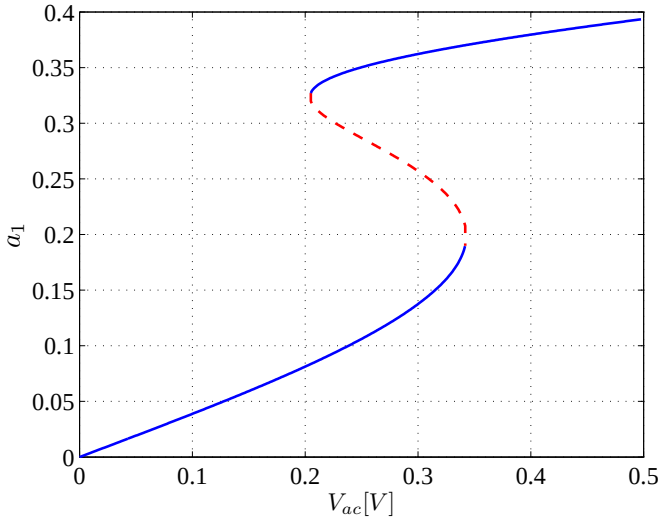

Figure 8.4: Force-response curve for $V_{dc} = 15$ V, $\sigma = -0.00025$, and $Q = 50$. The dashed lines (- - -) represent unstable solutions.

ed, the pull-in parameters change significantly by either causing the DC voltage to become really close to or far away from the pull-in voltage V_p. The other reason is that the moment arm associated with β is much larger than that associated with α.

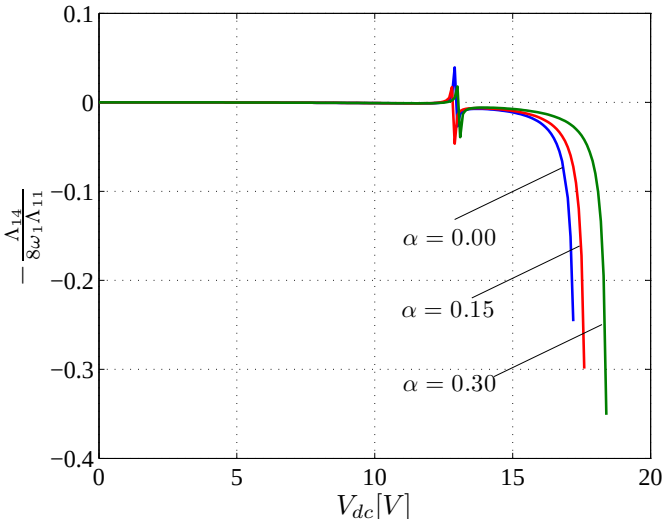

(a) Variation of α, $\beta = 0.85$.

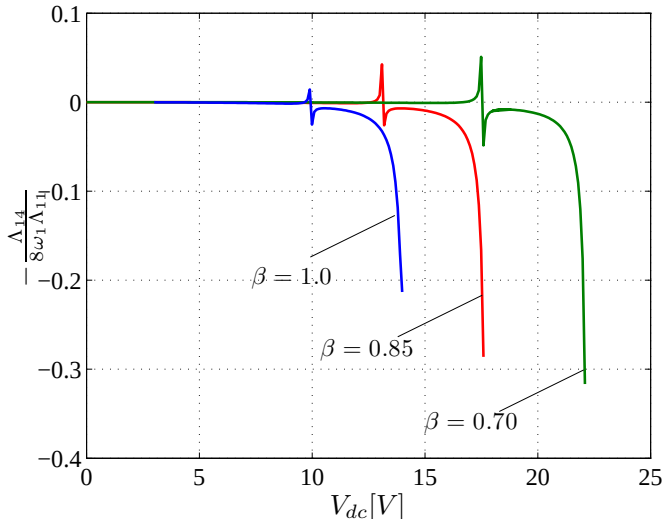

(b) Variation of β, $\alpha = 0.05$.

Figure 8.5: Sensitivity of the nonlinear response to changes in the electrodes dimensions α and β: $V_{ac} = 0.2$ V and $Q = 50$.

Chapter 9

Nonlinear Interactions in Torsional Micromirrors

In the previous chapter, we treated the general nonlinear response of the mirror to primary resonant excitations. We found that, due to the existence of small divisor terms in the second-order expansion, the effective nonlinearity is discontinuous at a certain DC voltage. This discontinuity occurs because of the nearness of the second-mode frequency to twice the first-mode frequency; that is, $\omega_2 \approx 2\omega_1$*. In this chapter, we use the method of multiple scales to obtain a second-order nonlinear analytical solution for the steady-state response of the mirror taking into account the two-to-one internal resonance. We first treat the case where the excitation frequency is near the first-mode frequency; that is,* $\Omega \approx \omega_1$*. Then we treat the case where the excitation frequency is near the second-mode frequency; that is,* $\Omega \approx \omega_2$*. We analyze the stability of the response and compare the analytical results to numerical solutions obtained by long-time integration of the equations of motion. We find that, due to the internal resonance, the mirror exhibits complex dynamic behavior. This behavior results in undesirable vibrations that can be detrimental to the mirror performance.*

9.1 Primary Resonance Excitation of the First Mode ($\Omega \approx \omega_1$)

The nonlinear solution obtained in the previous chapter does not account for modal interactions in the mirror response. In Fig. 9.1, we show variation of the first two natural frequencies of the mirror with the applied DC voltage V_{dc}. Clearly, the frequency of the second mode ω_2 is equal to twice the frequency of the first mode ω_1 at $V_{dc} \approx 13.2$ V. Hence, a two-to-one internal resonance might be activated between the two modes. Using the method of multiple scales, we determine a second-order nonlinear approximation that accounts for the internal resonance. To this end, we scale the parameters as follows:

$$V = V_{dc} + \varepsilon^2 V_{ac}\cos(\Omega t), \qquad \mu_1 = \varepsilon\mu_1, \qquad \mu_2 = \varepsilon\mu_2, \qquad \Omega = \omega_1 + \varepsilon\sigma_1, \qquad \omega_2 = 2\omega_1 + \varepsilon\sigma_2 \tag{9.1}$$

where ε is a small nondimensional bookkeeping parameter, and σ_1 and σ_2 are detuning parameters used to express the nearness of Ω to ω_1 and ω_2 to $2\omega_1$, respectively. Following steps similar to those used in the previous chapter, we obtain the following problems

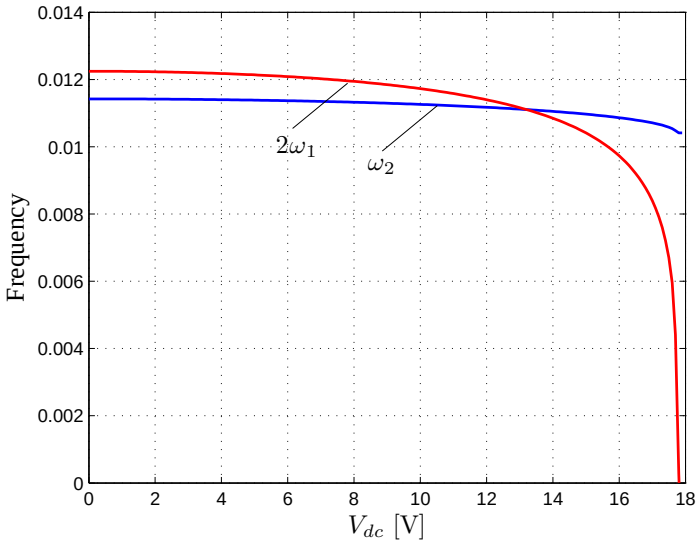

Figure 9.1: Variation of the mirror first two natural frequencies with V_{dc}.

$\underline{O(\varepsilon):}$

$$\begin{aligned} m_{11}D_0^2\theta_0 + (k_{11} - V_{dc}^2\Gamma_1\alpha_{12})\theta_0 - V_{dc}^2\Gamma_1\alpha_{13}u_0 = 0 \\ m_{22}D_0^2u_0 + (k_{22} - V_{dc}^2\Gamma_2\alpha_{23})u_0 - V_{dc}^2\Gamma_2\alpha_{22}\theta_0 = 0 \end{aligned} \tag{9.2a}$$

$\underline{O(\varepsilon^2):}$

$$\begin{aligned} m_{11}D_0^2\theta_1 + (k_{11} - V_{dc}^2\Gamma_1\alpha_{12})\theta_1 - V_{dc}^2\Gamma_1\alpha_{13}u_1 = -\mu_1 D_0\theta_0 - 2m_{11}D_0D_1\theta_0 \\ + V_{dc}^2\Gamma_1(\alpha_{15}\theta_0^2 + \alpha_{14}\theta_0u_0 + \alpha_{16}u_0^2) + V_{ac}V_{dc}\Gamma_1\alpha_{11}(e^{i\Omega T_0} + e^{-i\Omega T_0}) \\ m_{22}D_0^2u_1 + (k_{22} - V_{dc}^2\Gamma_2\alpha_{23})u_1 - V_{dc}^2\Gamma_2\alpha_{22}\theta_1 = -\mu_2 D_0u_0 - 2m_{22}D_0D_1u_0 \\ + V_{dc}^2\Gamma_2(\alpha_{25}\theta_0^2 + \alpha_{24}\theta_0u_0 + \alpha_{26}u_0^2) + V_{ac}V_{dc}\Gamma_2\alpha_{21}(e^{i\Omega T_0} + e^{-i\Omega T_0}) \end{aligned} \tag{9.2b}$$

$\underline{O(\varepsilon^3):}$

$$\begin{aligned} m_{11}D_0^2\theta_2 + \left(k_{11} - V_{dc}^2\Gamma_1\alpha_{12}\right)\theta_2 - V_{dc}^2\Gamma_1\alpha_{13}u_2 = -\mu_1(D_0\theta_1 + D_1\theta_0) - m_{11}(2D_0D_1\theta_1 + D_1^2\theta_0 \\ + 2D_0D_2\theta_0) + V_{dc}V_{ac}\Gamma_1(\alpha_{12}\theta_0 + \alpha_{13}u_0)\left(e^{i\Omega T_0} + e^{-i\Omega T_0}\right) + V_{dc}^2\Gamma_1(\alpha_{19}\theta_0^3 + 2\alpha_{15}\theta_0\theta_1 \\ + \alpha_{18}\theta_0^2u_0 + \alpha_{14}\theta_1u_0 + \alpha_{17}\theta_0u_0^2 + \alpha_{110}u_0^3 + \alpha_{14}\theta_0u_1 + 2\alpha_{16}u_0u_1) \\ m_{22}D_0^2u_2 + \left(k_{22} - V_{dc}^2\Gamma_2\alpha_{23}\right)u_2 - V_{dc}^2\Gamma_2\alpha_{22}\theta_2 = -\mu_2(D_0u_0 + D_1u_0) - m_{22}(2D_0D_1u_1 + D_1^2u_0 \\ + 2D_0D_2u_0) + V_{dc}V_{ac}\Gamma_2(\alpha_{22}\theta_0 + \alpha_{23}u_0)\left(e^{i\Omega T_0} + e^{-i\Omega T_0}\right) + V_{dc}^2\Gamma_2(\alpha_{29}\theta_0^3 + 2\alpha_{25}\theta_0\theta_1 \\ + \alpha_{28}\theta_0^2u_0 + \alpha_{24}\theta_1u_0 + \alpha_{27}\theta_0u_0^2 + \alpha_{210}u_0^3 + \alpha_{24}\theta_0u_1 + 2\alpha_{26}u_0u_1) \end{aligned} \tag{9.2c}$$

The solution of Equation (9.2a) is given in Equation (8.8). Substituting Equation (8.8) into Equation (9.2b) yields

$$
\begin{aligned}
m_{11}D_0^2\theta_1 + (k_{11} - V_{dc}^2\Gamma_1\alpha_{12})\theta_1 - V_{dc}^2\Gamma_1\alpha_{13}u_1 = &-i\mu_1(A_1\omega_1 e^{i\omega_1 T_0} + A_2\omega_2 e^{i\omega_2 T_0}) \\
&- 2im_{11}\omega_1 e^{i\omega_1 T_0} D_1 A_1 - 2im_{22}\omega_2 e^{i\omega_2 T_0} D_1 A_2 \\
&+ b_{11}A_1^2(T_1,T_2)e^{2i\omega_1 T_0} + b_{12}A_2^2(T_1,T_2)e^{2i\omega_2 T_0} \\
&+ b_{13}A_1(T_1,T_2)A_2(T_1,T_2)e^{i(\omega_1+\omega_2)T_0} \\
&+ b_{14}A_1(T_1,T_2)\bar{A}_2(T_1,T_2)e^{i(\omega_1-\omega_2)T_0} \\
&+ b_{151}A_1(T_1,T_2)\bar{A}_1(T_1,T_2) \\
&+ b_{152}A_2(T_1,T_2)\bar{A}_2(T_1,T_2) + \alpha_{11}V_{dc}V_{ac}e^{i\Omega T_0} + cc
\end{aligned}
\tag{9.3a}
$$

$$
\begin{aligned}
m_{22}D_0^2 u_1 + (k_{22} - V_{dc}^2\Gamma_2\alpha_{23})u_1 - V_{dc}^2\Gamma_2\alpha_{22}\theta_1 = &-i\mu_2(k_1 A_1\omega_1 e^{i\omega_1 T_0} + k_2 A_2\omega_2 e^{i\omega_2 T_0}) \\
&- 2im_{11}k_1\omega_1 e^{i\omega_1 T_0} D_1 A_1 - 2im_{22}\omega_2 k_2 e^{i\omega_2 T_0} D_1 A_2 \\
&+ b_{21}A_1^2(T_1,T_2)e^{2i\omega_1 T_0} + b_{22}A_2^2(T_1,T_2)e^{2i\omega_2 T_0} \\
&+ b_{23}A_1(T_1,T_2)A_2(T_1,T_2)e^{i(\omega_1+\omega_2)T_0} \\
&+ b_{24}A_1(T_1,T_2)\bar{A}_2(T_1,T_2)e^{i(\omega_1-\omega_2)T_0} \\
&+ b_{251}A_1(T_1,T_2)\bar{A}_1(T_1,T_2) \\
&+ b_{252}A_2(T_1,T_2)\bar{A}_2(T_1,T_2) + \alpha_{21}V_{dc}V_{ac}e^{i\Omega T_0} + cc
\end{aligned}
\tag{9.3b}
$$

where the coefficients b_{ij} are given in Equation (8.11). The terms proportional to $e^{\pm i\omega_1 T_0}$ and $e^{\pm i\omega_2 T_0}$ produce secular terms in θ_1 and u_1. Elimination of these terms on the right-hand side of Equations (9.3a) and 9.3b) yields the solvability conditions

$$
\begin{aligned}
2i\omega_1\Lambda_{11}D_1A_1 &= i\omega_1\Lambda_{12}A_1 + V_{ac}\Lambda_{13}e^{i\sigma_1 T_1} + \Lambda_{14}\bar{A}_1 A_2 e^{i\sigma_2 T_1} \\
2i\omega_2\Lambda_{21}D_1A_2 &= i\omega_2\Lambda_{22}A_2 + \Lambda_{24}A_1^2 e^{-i\sigma_2 T_1}
\end{aligned}
\tag{9.4}
$$

where Λ_{n1}, Λ_{n2}, and Λ_{13} are given in Equation (8.20) and

$$
\Lambda_{14} = 2\Lambda_{24} = b_{13}V_{dc}^2\Gamma_2\alpha_{22} - b_{23}\Delta_1(\omega_1)
$$

We substitute for D_1A_1 and D_1A_2 back into Equation (9.3a) and (9.3b). Then we write the complete nonsecular solution of the second-order equations as

$$\begin{aligned}\theta_1 =&B_1(T_1,T_2)e^{i\omega_1 T_0}+B_2(T_1,T_2)e^{i\omega_2 T_0}+c_{12}A_2^2e^{2i\omega_2 T_0}+c_{13}A_1A_2e^{i(\omega_1+\omega_2)T_0}\\&+c_{151}A_1\bar{A}_1+c_{152}A_2\bar{A}_2+cc\\ u_1 =&k_1B_1(T_1,T_2)e^{i\omega_1 T_0}+k_2B_2(T_1,T_2)e^{i\omega_2 T_0}+c_{22}A_2^2e^{2i\omega_2 T_0}+c_{23}A_1A_2e^{i(\omega_1+\omega_2)T_0}\\&+c_{251}A_1\bar{A}_1+c_{252}A_2\bar{A}_2+cc\end{aligned} \tag{9.5}$$

where cc stands for the complex-conjugate of the preceding terms. The first two terms in Equation (9.5) correspond to the homogeneous solution, whereas the remaining terms represent the particular solutions. The temporal functions B_1 and B_2 are defined at the next level, and the coefficients c_{n2}, c_{n3}, c_{n51}, and c_{n52} are given in Equation (8.18).

Substituting Equations (8.8) and (9.5) into Equation (9.2c), and eliminating the terms that lead to secular terms, we obtain

$$\begin{aligned}-2i\omega_1\Lambda_{11}(D_1B_1+D_2A_1)-\Lambda_{11}D_1^2A_1-\Lambda_{12}D_1A_1=&\,i\omega_1\Lambda_{12}B_1+\hat{\Lambda}_{13}V_{ac}A_2e^{i(\sigma_2-\sigma_1)T_1}\\&+\Lambda_{14}(A_2\bar{B}_1+B_2\bar{A}_1)e^{i\sigma_2T_1}+\hat{\Lambda}_{15}\bar{A}_1A_1^2+\hat{\Lambda}_{16}A_1A_2\bar{A}_2\\-2i\omega_2\Lambda_{21}(D_1B_2+D_2A_2)-\Lambda_{21}D_1^2A_2-\Lambda_{22}D_1A_2=&\,i\omega_2\Lambda_{22}B_2+\hat{\Lambda}_{23}V_{ac}A_1e^{i(\sigma_1-\sigma_2)T_1}\\&+\hat{\Lambda}_{25}\bar{A}_2A_2^2+\hat{\Lambda}_{26}A_1\bar{A}_1A_2\end{aligned} \tag{9.6}$$

where

$$\begin{aligned}&\hat{\Lambda}_{13}=V_{dc}\Gamma_2[\alpha_{22}\Delta_2(\omega_1)-k_2\Gamma_2\alpha_{23}\Delta_1(\omega_1)],\\&\hat{\Lambda}_{23}=V_{dc}\Gamma_2[\alpha_{22}\Delta_2(\omega_2))-k_1\Gamma_2\alpha_{23}\Delta_1(\omega_1)],\\&\hat{\Lambda}_{15}=-V_{dc}^2(\Delta_1(\omega_1)Z_2-\Gamma_2\alpha_{22}V_{dc}^2Z_1),\qquad \hat{\Lambda}_{25}=-V_{dc}^2(\Delta_1(\omega_1)\tilde{Z}_2-\Gamma_2\alpha_{22}V_{dc}^2\tilde{Z}_1),\\&\hat{\Lambda}_{16}=-V_{dc}^2(\Delta_1(\omega_1)Y_2-\Gamma_2\alpha_{22}V_{dc}^2Y_1),\qquad \hat{\Lambda}_{26}=-V_{dc}^2(\Delta_1(\omega_1)\tilde{Y}_2-\Gamma_2\alpha_{22}V_{dc}^2\tilde{Y}_1).\end{aligned}$$

and Z_n, $\tilde{Z}_n$, Y_n, and $\tilde{Y}_n$ are given in Equation (8.21).

Following Nayfeh [90], we choose the functions B_1 and B_2 so as to eliminate $D_1^2A_1$ and $D_1^2A_2$ from Equations (9.6), this will ensure that Equations (9.6) are derivable from a Lagrangian. These conditions lead to

$$D_1[2i\omega_1B_1+D_1A_1]=0,\qquad D_1[2i\omega_2B_2+D_1A_2]=0. \tag{9.7}$$

Integrating with respect to T_1, we get

$$[2i\omega_1 B_1 + D_1 A_1] = c_1(T_2), \qquad [2i\omega_2 B_2 + D_1 A_2] = c_2(T_2). \tag{9.8}$$

Note from Equations (9.4) that $D_1 A_1$ and $D_1 A_2$ are not functions of T_2. Therefore, it is necessary that $c_1(T_2) = c_2(T_2) = 0$, which yields

$$\begin{aligned} B_1 =& i\frac{\Lambda_{12}}{4\omega_1\Lambda_{11}}A_1 + V_{ac}\frac{\Lambda_{13}}{4\omega_1^2\Lambda_{11}}e^{i\sigma_1 T_1} + \frac{\Lambda_{14}}{4\omega_1^2\Lambda_{11}}\bar{A}_1 A_2 e^{i\sigma_2 T_1} \\ B_2 =& i\frac{\Lambda_{22}}{4\omega_2\Lambda_{21}}A_2 + \frac{\Lambda_{24}}{4\omega_2^2\Lambda_{21}}A_1^2 e^{-i\sigma_2 T_1} \end{aligned} \tag{9.9}$$

Substituting Equations (9.9) into Equations (9.6), we obtain

$$\begin{aligned} -2i\omega_1\Lambda_{11}D_2A_1 =& \frac{\Lambda_{12}^2}{4\Lambda_{11}}A_1 - iV_{ac}\frac{\Lambda_{12}\Lambda_{13}}{4\omega_1\Lambda_{11}}e^{i\sigma_1 T_1} + V_{ac}\left(\hat{\Lambda}_{13} + \frac{\Lambda_{13}\Lambda_{14}}{4\omega_1^2\Lambda_{11}}\right)A_2 e^{i(\sigma_2-\sigma_1)T_1} \\ &+ i\frac{\Lambda_{22}\Lambda_{24}}{2\omega_2\Lambda_{21}}A_2\bar{A}_1 e^{i\sigma_2 T_1} + \left(\hat{\Lambda}_{15} + \frac{\Lambda_{24}\Lambda_{14}}{4\omega_2^2\Lambda_{21}}\right)\bar{A}_1 A_1^2 + \left(\hat{\Lambda}_{16} + \frac{\Lambda_{14}^2}{4\omega_1^2\Lambda_{11}}\right)A_1 A_2\bar{A}_2 \end{aligned} \tag{9.10a}$$

$$\begin{aligned} -2i\omega_2\Lambda_{21}D_2A_2 =& \frac{\Lambda_{22}^2}{4\Lambda_{21}}A_2 - i\frac{\Lambda_{22}\Lambda_{24}}{4\omega_2\Lambda_{21}}A_1^2 e^{-i\sigma_2 T_1} + \hat{\Lambda}_{23}V_{ac}A_1 e^{i(\sigma_1-\sigma_2)T_1} + \hat{\Lambda}_{25}\bar{A}_2 A_2^2 \\ &+ \hat{\Lambda}_{26}A_1\bar{A}_1 A_2 \end{aligned} \tag{9.10b}$$

Since the above equations should be derivable from a Lagrangian and a virtual work term, the coefficient associated with $A_2\bar{A}_1$ in Equation (9.10a) is twice the coefficient associated with A_1^2 in Equation (9.10b). Similarly, the coefficient associated with $A_1 A_2\bar{A}_2$ in Equation (9.10a) is equal to the coefficient associated with $A_2 A_1\bar{A}_1$ in Equation (9.10b). To obtain the final solution to second-order, we reconstitute the solution using the following equation:

$$\frac{dA_n}{dt} = \varepsilon D_1 A_n + \varepsilon^2 D_2 A_n + ..., \qquad n = 1, 2. \tag{9.11}$$

We substitute Equations (9.4), (9.10a), (9.10b) into Equation (9.11), set $T_n = \varepsilon^n t$, then set ε equal to unity, and obtain the following reconstituted modulation equations:

$$\begin{aligned} -2i\omega_1\Lambda_{11}\frac{dA_1}{dt} =& (\mathcal{S}_{12} + i\bar{\mathcal{S}}_{12})A_1 + (\mathcal{S}_{13} + i\bar{\mathcal{S}}_{13})V_{ac}e^{i\sigma_1 t} + \mathcal{S}_{14}V_{ac}A_2 e^{i(\sigma_2-\sigma_1)t} \\ &+ (\mathcal{S}_{15} + i\bar{\mathcal{S}}_{15})A_2\bar{A}_1 e^{i\sigma_2 t} + \mathcal{S}_{16}\bar{A}_1 A_1^2 + \mathcal{S}_{17}A_1 A_2\bar{A}_2 \end{aligned} \tag{9.12a}$$

$$-2i\omega_2\Lambda_{21}\frac{dA_2}{dt} = (\mathcal{S}_{22}+i\bar{\mathcal{S}}_{22})A_2 + (\mathcal{S}_{25}+i\bar{\mathcal{S}}_{25})A_1^2 e^{-i\sigma_2 t} + \mathcal{S}_{24}V_{ac}A_1 e^{i(\sigma_1-\sigma_2)t} + \mathcal{S}_{26}\bar{A}_2A_2^2 + \mathcal{S}_{27}A_1\bar{A}_1A_2 \tag{9.12b}$$

where

$$\begin{aligned}
&\mathcal{S}_{n2} = \frac{\Lambda_{n2}^2}{4\Lambda_{n1}}, && \bar{\mathcal{S}}_{n2} = \Lambda_{n2}\omega_n,\\
&\mathcal{S}_{n3} = \Lambda_{n3}, && \bar{\mathcal{S}}_{n3} = -\frac{\Lambda_{n2}\Lambda_{n3}}{4\omega_n\Lambda_{n1}},\\
&\mathcal{S}_{14} = \left(\hat{\Lambda}_{13} + \frac{\Lambda_{13}\Lambda_{14}}{4\omega_1^2\Lambda_{11}}\right), && \mathcal{S}_{24} = \hat{\Lambda}_{23},\\
&\mathcal{S}_{15} = 2\mathcal{S}_{25} = 2\Lambda_{24}, && \bar{\mathcal{S}}_{15} = 2\bar{\mathcal{S}}_{25} = \frac{\Lambda_{22}\Lambda_{24}}{2\omega_2\Lambda_{21}},\\
&\mathcal{S}_{16} = \left(\hat{\Lambda}_{15} + \frac{\Lambda_{24}\Lambda_{14}}{4\omega_2^2\Lambda_{21}}\right), && \mathcal{S}_{26} = \hat{\Lambda}_{25},\\
&\mathcal{S}_{17} = \mathcal{S}_{27} = \left(\hat{\Lambda}_{16} + \frac{\Lambda_{14}^2}{4\omega_1^2\Lambda_{11}}\right), && n = 1, 2.
\end{aligned}$$

We illustrate the effect of neglecting the interaction between the two modes by showing variation of the effective nonlinearity coefficient $\mathcal{S}_{16}$ with V_{dc} in Fig. 9.2. Using a single-mode analysis results in a singularity at $V_{dc} \approx 13.2$ V. This value of the DC voltage corresponds to the two-to-one internal resonance between the first and second modes. As a result, neglecting this interaction yields a qualitatively and quantitatively erroneous solution, which might hide the actual dynamics of the mirror. It is also obvious that the effect of the singularity is not limited to a narrow region around $V_{dc} \approx 13.2$ V, but it extends over a wide range of the applied DC voltage. Therefore, avoiding the operation in that region limits the operation range of the microscanner. Next, we express the resulting modulation equations in terms of real variables by introducing Equation (8.22) into Equations (9.12a) and (9.12b), separating the real and imaginary parts and obtaining the following equations:

$$\begin{aligned}
\omega_1\Lambda_{11}\dot{a}_1 &= -\frac{1}{2}\bar{\mathcal{S}}_{12}a_1 - V_{ac}(\mathcal{S}_{13}\sin\gamma_1 + \bar{\mathcal{S}}_{13}\cos\gamma_1) + \frac{1}{2}\mathcal{S}_{14}V_{ac}a_2\sin(\gamma_1-\gamma_2)\\
&\quad - \frac{1}{4}a_1a_2(\mathcal{S}_{15}\sin\gamma_2 + \bar{\mathcal{S}}_{15}\cos\gamma_2)\\
\omega_1\Lambda_{11}a_1(\sigma_1-\dot{\gamma}_1) &= \frac{1}{2}\mathcal{S}_{12}a_1 + V_{ac}(\mathcal{S}_{13}\cos\gamma_1 + \bar{\mathcal{S}}_{13}\sin\gamma_1) - \frac{1}{2}V_{ac}\mathcal{S}_{14}a_2\cos(\gamma_1-\gamma_2)\\
&\quad + \frac{1}{4}a_1a_2(\mathcal{S}_{15}\cos\gamma_2 - \bar{\mathcal{S}}_{15}\sin\gamma_2) + \frac{1}{8}\mathcal{S}_{16}a_1^3 + \frac{1}{8}\mathcal{S}_{17}a_1a_2^2
\end{aligned} \tag{9.13a}$$

$$\omega_2\Lambda_{21}\dot{a}_2 = -\frac{1}{2}\bar{\mathcal{S}}_{22}a_2 - \frac{1}{2}\mathcal{S}_{24}V_{ac}a_1\sin(\gamma_1-\gamma_2) + \frac{1}{4}a_1^2(\mathcal{S}_{25}\sin\gamma_2 - \bar{\mathcal{S}}_{25}\cos\gamma_2)$$

$$\begin{aligned}\omega_2\Lambda_{21}a_2(\dot{\gamma}_2-\dot{\gamma}_1+2\sigma_1-\sigma_2) = {}& \frac{1}{2}\mathcal{S}_{22}a_2 + \frac{1}{2}V_{ac}\mathcal{S}_{24}a_1\cos(\gamma_1-\gamma_2) + \frac{1}{4}a_1^2(\mathcal{S}_{25}\cos\gamma_2 + \bar{\mathcal{S}}_{25}\sin\gamma_2)\\ & + \frac{1}{8}\mathcal{S}_{26}a_2^3 + \frac{1}{8}\mathcal{S}_{27}a_1^2a_2\end{aligned} \tag{9.13b}$$

where

$$\gamma_1 = \sigma_1 t - \beta_1, \qquad \gamma_2 = \sigma_2 t - 2\beta_1 + \beta_2.$$

The behavior of the mirror is characterized by the solution of the modulation equations. When the modulation equations have an equilibrium solution, the response of the mirror is periodic. On the other hand, when the modulation equations have a periodic solution, the response of the mirror is either periodic or quasiperiodic, depending on the frequency of the resulting limit cycle. If the frequency of the resulting limit cycle is commensurate with the excitation frequency, the response is periodic, otherwise it is quasiperiodic.

When the modulation equations have a quasiperiodic solution, the response of the mirror is quasiperiodic with higher number of independent frequencies. Finally, if the solution of

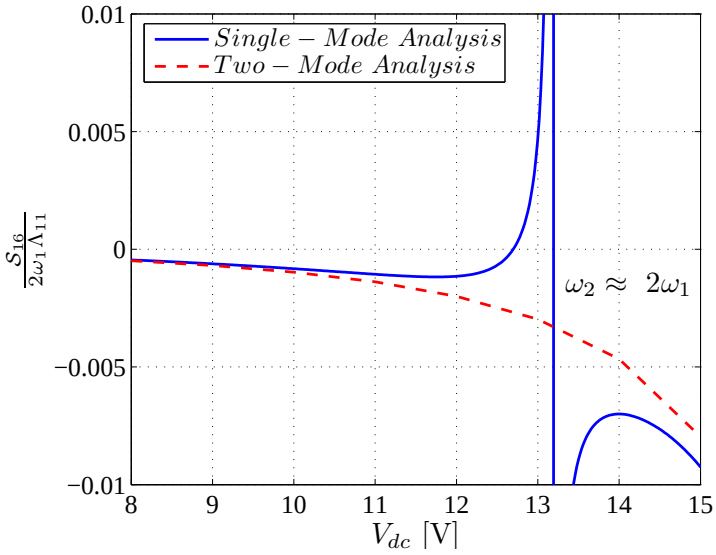

Figure 9.2: Variation of the effective nonlinearity coefficient $\mathcal{S}_{16}$ of the first mode with the applied voltage V_{dc}.

the modulation equations is chaotic, then the response of the microscanner is also chaotic. To analyze the periodic response of the mirror, we study the equilibrium solutions of Equations (9.13). These equilibrium solutions are obtained by setting the time derivatives in Equations (9.13) equal to zero and solving for the roots (a_1, a_2, γ_1, γ_2). As a control parameter is varied, the roots are found using a Newton-Raphson numerical technique. The stability of the equilibrium solutions is determined by finding the eigenvalues of the Jacobian matrix of the modulation equations evaluated at the root. If all of the eigenvalues associated with a given solution have negative real parts, it is asymptotically stable. Otherwise, if one or more eigenvalues have positive real parts, the solution is unstable.

Using Equation (8.22), we express the response of the mirror to second order as

$$\begin{aligned}\theta(t) = \theta_s &+ \left(1+\frac{\mathcal{S}_{11}}{\omega_1}\right)a_1\cos(\omega_1 t+\beta_1) + \left(1+\frac{\mathcal{S}_{21}}{\omega_2}\right)a_2\cos(\omega_2 t+\beta_2)\\ &+ \frac{\Lambda_{14}}{8\omega_1^2\Lambda_{11}}a_1a_2\cos[(\omega_1+\sigma_2)t+\beta_2-\beta_1] + \frac{1}{2}c_{12}a_1a_2\cos[(\omega_1+\omega_2)t+\beta_1+\beta_2]\\ &+ \frac{\Lambda_{24}}{8\omega_2^2\Lambda_{21}}a_1^2\cos[(\omega_2-\sigma_2)t+2\beta_1] + \frac{1}{2}c_{11}a_2^2\cos[2\omega_2 t+2\beta_2] + \frac{1}{2}c_{13}a_1^2 + \frac{1}{2}c_{14}a_1a_2\\ &+ V_{ac}\frac{\bar{\mathcal{S}}_{13}}{\Lambda_{12}\omega_1}\cos[(\omega_1+\sigma_1)t] + \ldots\end{aligned} \tag{9.14a}$$

$$\begin{aligned}u(t) = u_s &+ k_1\left(1+\frac{\mathcal{S}_{11}}{\omega_1}\right)a_1\cos(\omega_1 t+\beta_1) + k_2\left(1+\frac{\mathcal{S}_{21}}{\omega_2}\right)a_2\cos(\omega_2 t+\beta_2)\\ &+ k_1\frac{\Lambda_{14}}{8\omega_1^2\Lambda_{11}}a_1a_2\cos[(\omega_1+\sigma_2)t+\beta_2-\beta_1] + \frac{1}{2}c_{22}a_1a_2\cos[(\omega_1+\omega_2)t+\beta_1+\beta_2]\\ &+ k_2\frac{\Lambda_{24}}{8\omega_2^2\Lambda_{21}}a_1^2\cos[(\omega_2-\sigma_2)t+2\beta_1] + \frac{1}{2}c_{21}a_2^2\cos(2\omega_2 t+2\beta_2) + \frac{1}{2}c_{23}a_1^2 + \frac{1}{2}c_{24}a_1a_2\\ &+ k_1V_{ac}\frac{\bar{\mathcal{S}}_{13}}{\Lambda_{12}\omega_1}\cos[(\omega_1+\sigma_1)t] + \ldots\end{aligned} \tag{9.14b}$$

To validate the analytical solution, we integrate Equations (7.8) numerically to obtain the steady-state response of the mirror at the critical DC voltage $V_{dc} = 13.21$ V when the mirror is excited near primary resonance of the first mode ($\sigma_1 = -0.0002$) at $V_{ac} = 0.1$ V. We then compare the numerical results with those obtained analytically using Equations (9.14).

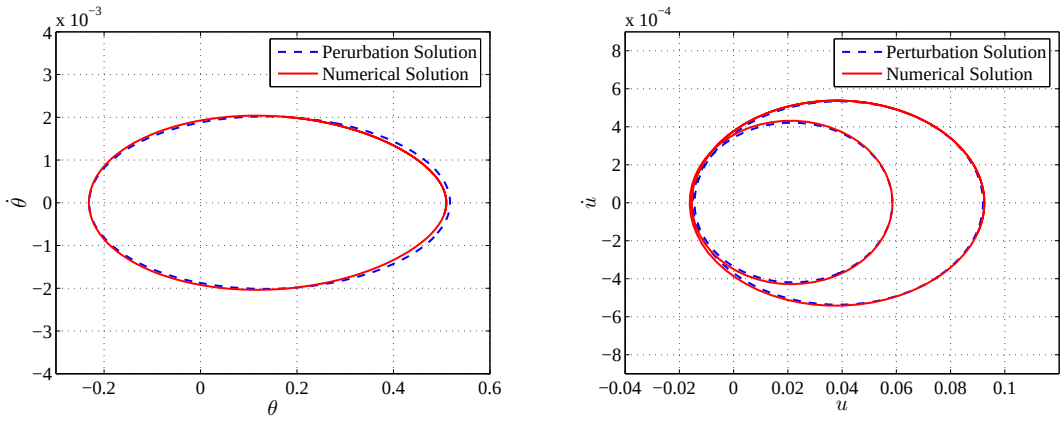

(a) (b)

Figure 9.3: Phase portrait of the mirror response at $V_{dc} = 13.21$ V when the mirror is excited near primary resonance of the first mode ($\sigma_1 = -0.0002$) at $V_{ac} = 0.1$ V.

The phase portraits of the steady-state response of the micromirror in Fig. 9.3 demonstrate excellent agreement between the numerical and analytical solutions.

We study variation of the amplitudes of the equilibrium solutions of Equations (9.13) (a_1, a_2) with the excitation frequency detuning parameter σ_1 for different values of V_{dc}. We fix the value of the AC voltage at $V_{ac} = 0.1$ V for all cases. To achieve large amplitudes, microscanners are usually designed to operate at very large quality factors, therefore we choose a quality factor $Q = 250$ for all cases. We denote stable equilibrium solutions by solid lines and unstable ones by dashed or dotted lines.

For $V_{dc} = 11$ V, most of the energy is trapped in the first mode, as shown in Fig. 9.4 (a) and (b). The influence of the second mode is extremely small, especially at $\sigma_1 = 0$, as evident from the time histories in Figs. 9.5 (a) and (b) . However, another small branch of solutions appears at $\sigma_1 \approx -0.00018$, which indicates that the internal resonance is close to being activated. As we discussed in the previous chapter, the frequency-response curve of the first mode is bent to the left, indicating a softening-type nonlinearity.

As V_{dc} is increased towards the critical value $V_{dc} \approx 13.2$ V, Figs. 9.4 (c) and (d), the frequency response curves bend more towards the left, indicating that the effective softening nonline-

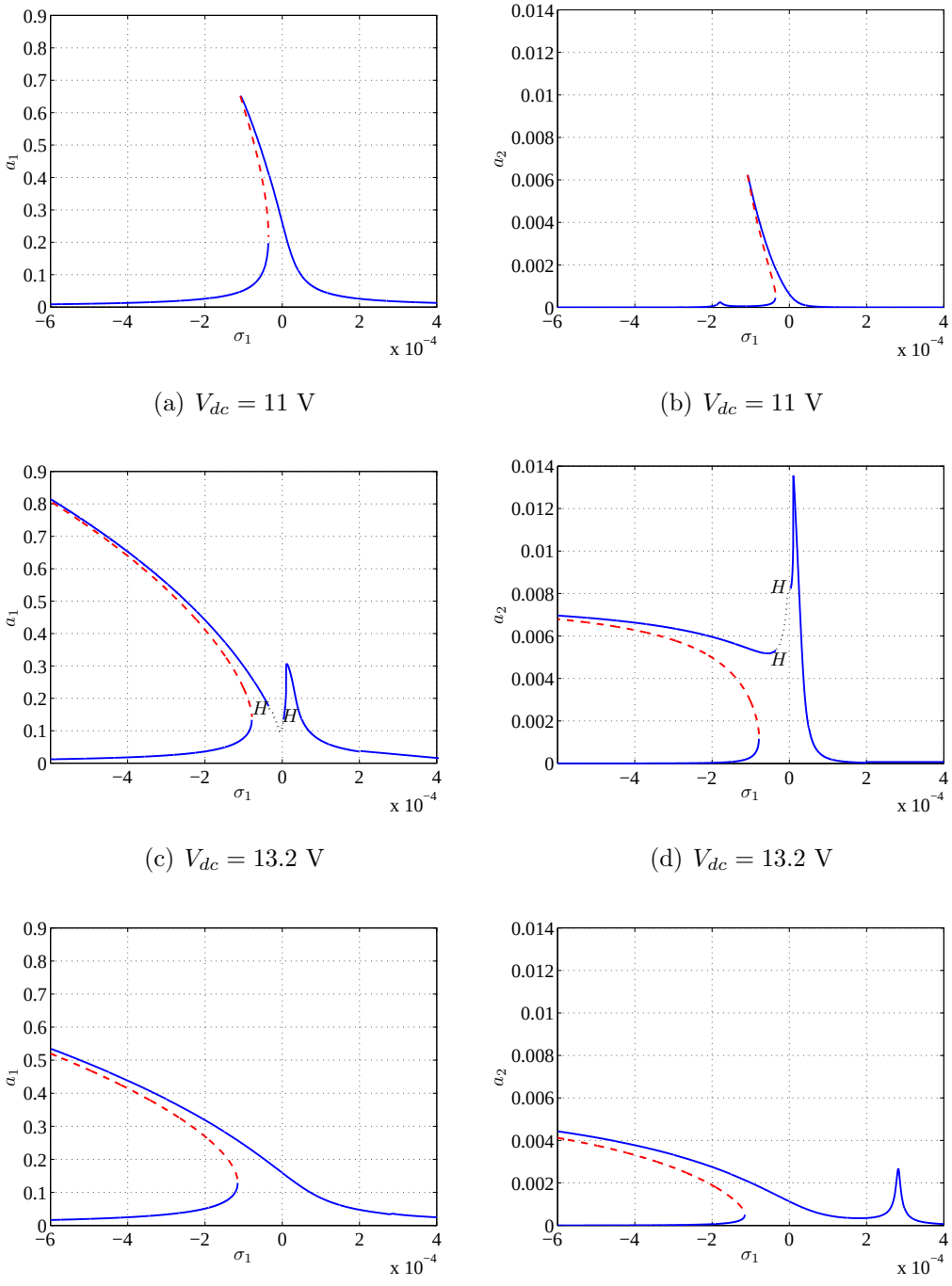

(a) $V_{dc} = 11$ V (b) $V_{dc} = 11$ V

(c) $V_{dc} = 13.2$ V (d) $V_{dc} = 13.2$ V

(e) $V_{dc} = 15$ V (f) $V_{dc} = 15$ V

Figure 9.4: Variation of the amplitudes of the first and second modes with the driving frequency detuning parameter σ_1 when the first mode is excited near primary resonance at $V_{ac} = 0.1$ V. The letter H is used to denote Hopf bifurcations.

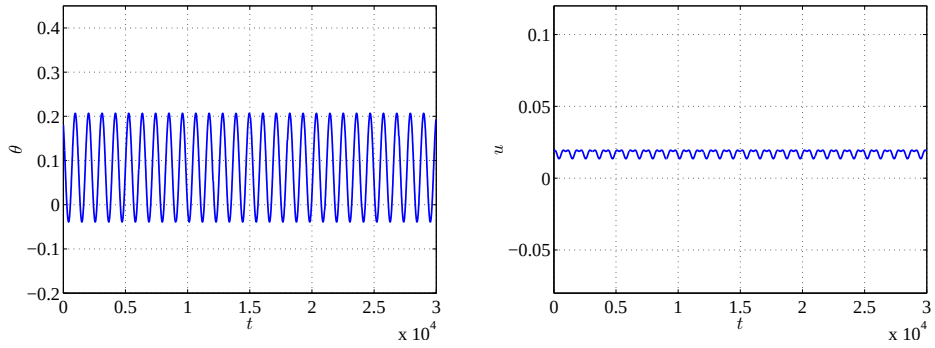

(a) $V_{dc} = 11$ V (b) $V_{dc} = 11$ V

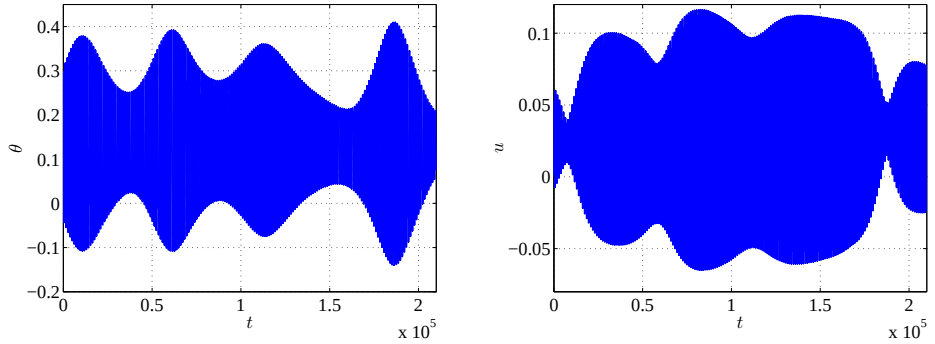

(c) $V_{dc} = 13.2$ V (d) $V_{dc} = 13.2$ V

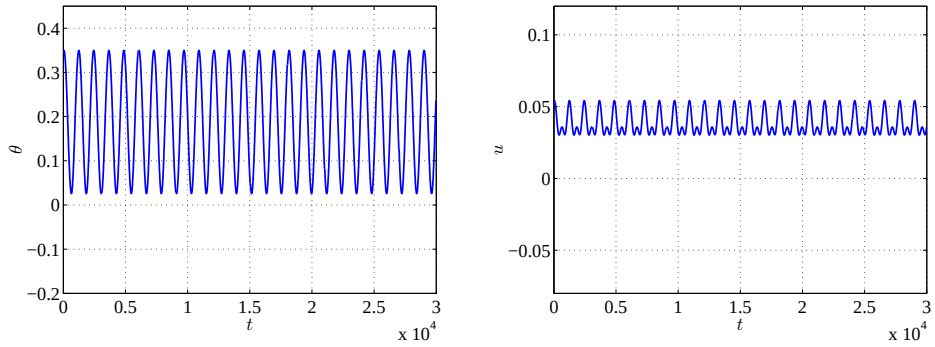

(e) $V_{dc} = 15$ V (f) $V_{dc} = 15$V

Figure 9.5: Long-time histories of the micromirror responses for $\sigma_1 = 0$ and $V_{ac} = 0.1$ V.

arity increases as V_{dc} increases. Moreover, the second branch of the two-mode solution becomes more significant and shifts towards $\sigma_1 = 0$. A region of dynamic solutions appears as a result of the equilibrium solutions of the modulation equations loosing stability via two

Hopf bifurcations. This region extends between $\sigma_1 = 0$ and $\sigma_1 = -0.00002$, resulting in an undesired quasiperiodic response of the scanner, as shown in Fig. 9.5 (c) and (d). This quasiperiodic behavior causes undesired fluctuations in the amplitude of the steady-state response of the scanner, which results in distorted images.

A further increase in V_{dc}, as shown in Figs. 9.4 (c) and (d), results in an increase in the bending of the frequency-response curves towards the left and a shift in the second branch of the solution towards the right and away from $\sigma_1 = 0$. The effect of the second mode becomes less important and it diminishes as V_{dc} is increased further. Figures. 9.5 (e) and (f) illustrate the periodic nature of the mirror response.

9.2 Primary Resonance Excitation of the Second Mode ($\Omega \approx \omega_2$)

In this case, we let $\Omega = \omega_2 + \varepsilon\sigma_1$ and follow steps similar to those used in the previous section and obtain the following modulation equations:

$$\begin{aligned}
\omega_1\Lambda_{11}\dot{a_1} &= -\frac{1}{2}\bar{\mathcal{S}}_{12}a_1 - \frac{1}{2}\mathcal{S}_{24}V_{ac}a_1\sin\gamma_1 - \frac{1}{4}a_1a_2(\mathcal{S}_{15}\sin\gamma_2 + \bar{\mathcal{S}}_{15}\cos\gamma_2)\\
\frac{1}{2}\omega_1\Lambda_{11}a_1(\sigma_1+\sigma_2-\dot{\gamma}_1) &= \frac{1}{2}\mathcal{S}_{12}a_1 + \frac{1}{2}\mathcal{S}_{24}V_{ac}a_1\cos\gamma_1 + \frac{1}{4}a_1a_2(\mathcal{S}_{15}\cos\gamma_2 - \bar{\mathcal{S}}_{15}\sin\gamma_2)\\
&\quad + \frac{1}{8}\mathcal{S}_{16}a_1^3 + \frac{1}{8}\mathcal{S}_{17}a_1a_2^2
\end{aligned} \tag{9.15a}$$

$$\begin{aligned}
\omega_2\Lambda_{21}\dot{a_2} &= -\frac{1}{2}\bar{\mathcal{S}}_{22}a_2 - V_{ac}(\mathcal{S}_{23}\sin\gamma_2 + \bar{\mathcal{S}}_{23}\cos\gamma_2) + \frac{1}{4}a_1^2(\mathcal{S}_{25}\sin\gamma_2 - \bar{\mathcal{S}}_{25}\cos\gamma_2)\\
\omega_2\Lambda_{21}a_2(\sigma_1-\dot{\gamma}_2) &= \frac{1}{2}\mathcal{S}_{22}a_2 - V_{ac}(\bar{\mathcal{S}}_{23}\sin\gamma_2 - \mathcal{S}_{23}\cos\gamma_2) + \frac{1}{4}a_1^2(\mathcal{S}_{25}\cos\gamma_2 + \bar{\mathcal{S}}_{25}\sin\gamma_2)\\
&\quad + \frac{1}{8}\mathcal{S}_{26}a_2^3 + \frac{1}{8}\mathcal{S}_{27}a_1^2a_2
\end{aligned} \tag{9.15b}$$

where

$$\gamma_1 = (\sigma_1 + \sigma_2)t - 2\beta_1, \qquad \gamma_2 = \sigma_1 t - \beta_2.$$

In the case of primary resonance near the second mode, the equilibrium solutions of the modulation equations are either a single-mode solution $(0, a_2)$, a two-mode solution (a_1, a_2), or both simultaneously. In Fig. 9.6, we study variation of the response amplitude with the driving frequency detuning parameter σ_1. For $V_{dc} = 11$ V, the energy is trapped in the second mode only, as shown in Fig. 9.6 (a) and (b). The solution of the modulation equations yields only the single-mode solution $(0, a_2)$. Therefore, the nonlinear interaction can be neglected and a single-mode perturbation solution is enough to accurately represent the dynamics of the mirror. The long-time history of the response shown in Fig. 9.7 illustrates that the second mode completely dominates the response of the mirror.

As V_{dc} approaches the critical values $V_{dc} = 13.2$ V, the single-mode solution looses stability via two pitchfork bifurcations at $\sigma_1 = -0.000073$ and $\sigma_1 = 0.000058$, Fig. 9.6(c) and (d). As a result, a two-peak branch of the two-mode solution appears in the frequency-response curves in the vicinity of $\sigma_1 = 0$. In this case, most of the system energy is transferred into the indirectly excited first mode, and it is obvious that a single-mode solution is not enough to represent the dynamics of the mirror. In Fig. 9.8, we show the long time-histories of the response for different values of σ_1. At $\sigma_1 = 0$, there is only one two-mode solution, where a_1 is much larger than a_2. The angular response of the mirror is periodic with the first mode frequency being the dominant frequency, Fig. 9.8 (a). However, due to the linear coupling, the bending response of the mirror is periodic with both frequencies appearing in the response, Fig. 9.8 (b). At $\sigma_1 = -0.0004$ both of the single-mode and two-mode solutions coexist. Therefore, torsional oscillations of the mirror can be large and dominated by the first-mode frequency, as shown in Fig. 9.8 (c), or very small and dominated by the second-mode frequency as shown in Fig. 9.8 (d).

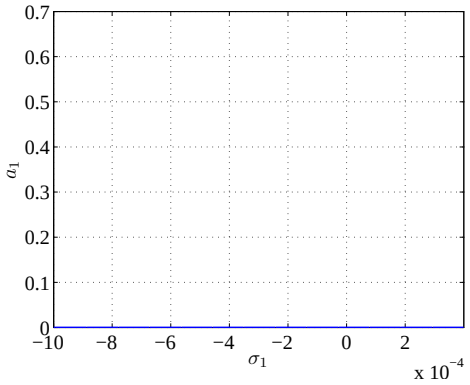

(a) $V_{dc} = 11$ V

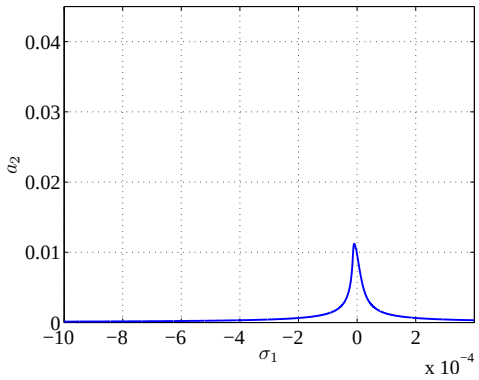

(b) $V_{dc} = 11$ V

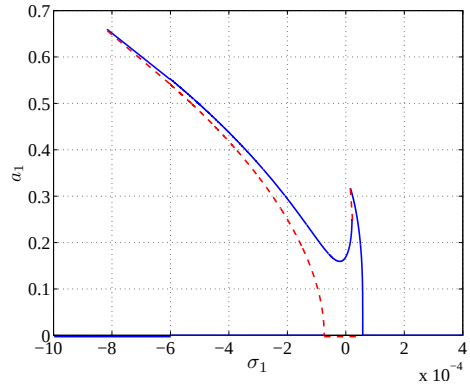

(c) $V_{dc} = 13.2$ V

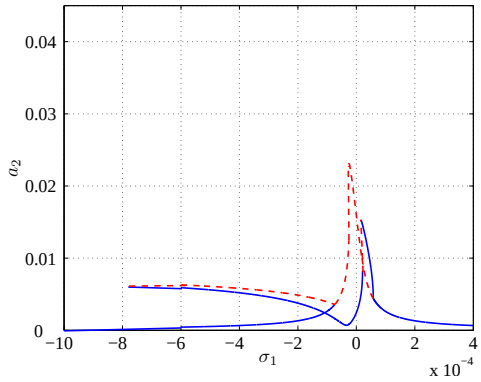

(d) $V_{dc} = 13.2$ V

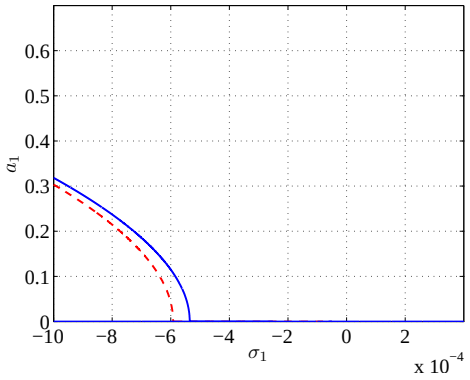

(e) $V_{dc} = 15$ V

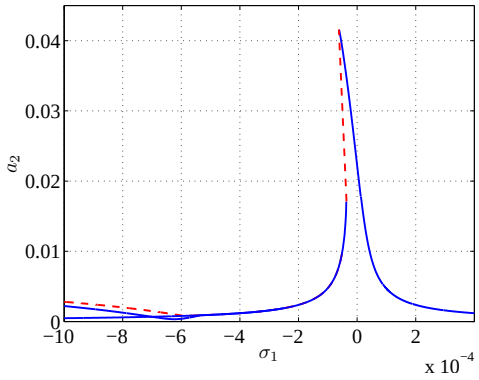

(f) $V_{dc} = 15$ V

Figure 9.6: Variation of the amplitudes of the first and second modes with the driving frequency detuning parameter σ_1 when the second mode is excited near primary resonance at $V_{ac} = 0.1$ V.

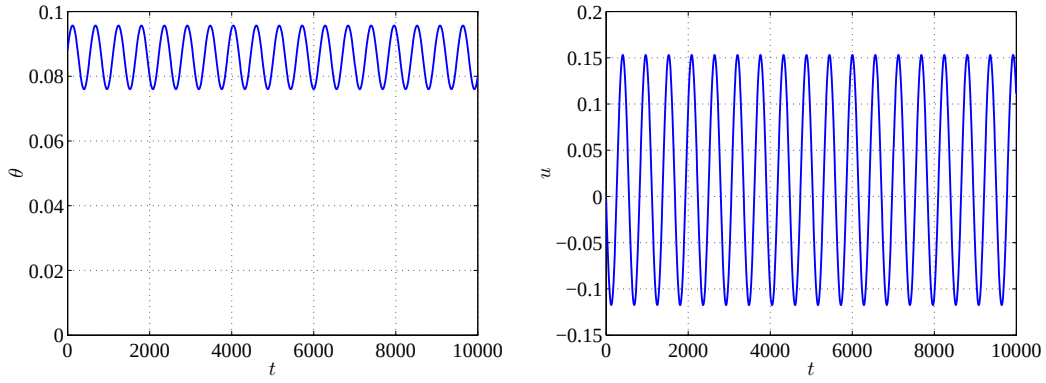

(a) $\sigma_1 = 0$ (b) $\sigma_1 = 0$

Figure 9.7: Long-time histories of the micromirror response for $V_{dc} = 11$ V and $V_{ac} = 0.1$ V.

As V_{dc} is increased beyond the critical-internal resonance value, we find that the two-mode solution shifts towards the left, as shown in Figs. 9.6 (e) and (f), where the single-mode solution looses stability via two pitchfork bifurcations at $\sigma_1 \approx -0.0006$ and $\sigma_1 \approx -0.00055$, respectively. Therefore, a two-mode solution is still necessary to represent the actual dynamics of the mirror. In Figs. 9.9 (a) and (b), we show long-time histories of the micromirror response at $\sigma_1 = 0$. At this value of σ_1, the second mode dominates both of the torsional and bending responses of the mirror, resulting in a very large bending response.

At $\sigma_1 = -0.0008$, both of the single-mode and two-mode solutions coexist. In Figs. 9.9 (b) and (c), we show the long-time histories of the two-mode solution. In this case, the torsional response of the mirror is very large and dominated by the first-mode frequency, whereas, due to linear coupling, both frequencies coexist in the bending response.

In Figs. 9.10 (a) and (b), we show variation of the response amplitudes with the driving AC excitation V_{ac} at the critical internal resonance voltage $V_{dc} = 13.2$ V. We excite the second mode near primary resonance at the detuning value $\sigma_1 = -0.00002$. For $V_{ac} \leq 0.008$ V only a single-mode trivial solution exists. As V_{ac} is increased, the single-mode trivial solution

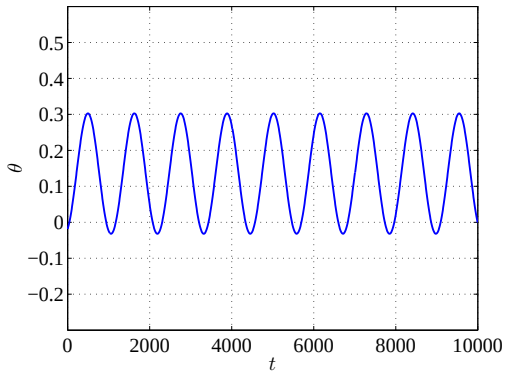

(a) $\sigma_1 = 0$

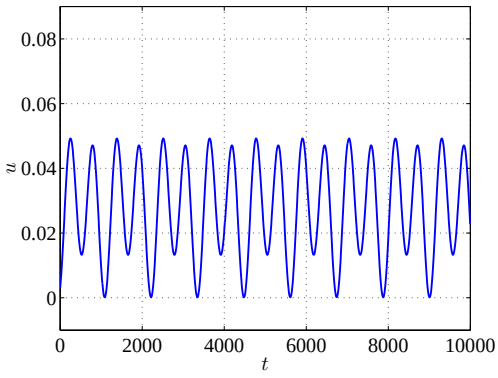

(b) $\sigma_1 = 0$

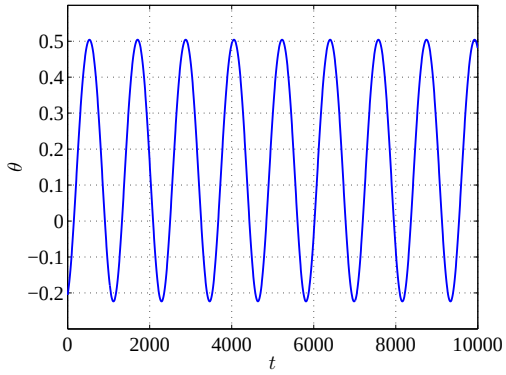

(c) $\sigma_1 = -0.0004$

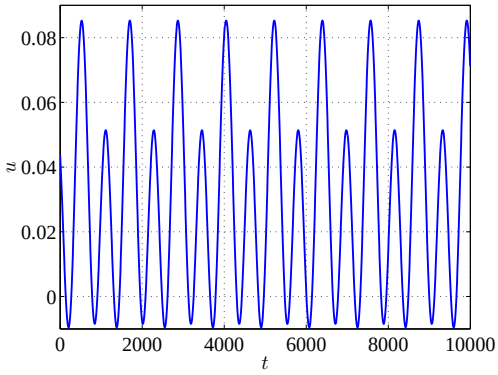

(d) $\sigma_1 = -0.0004$

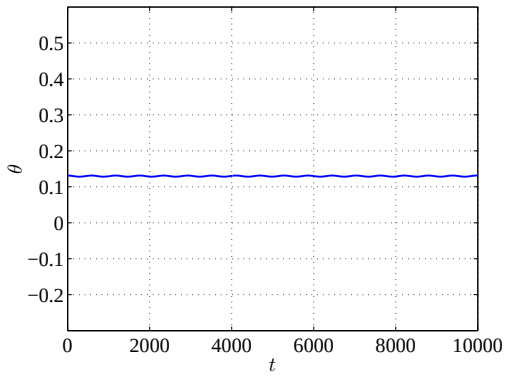

(e) $\sigma_1 = -0.0004$

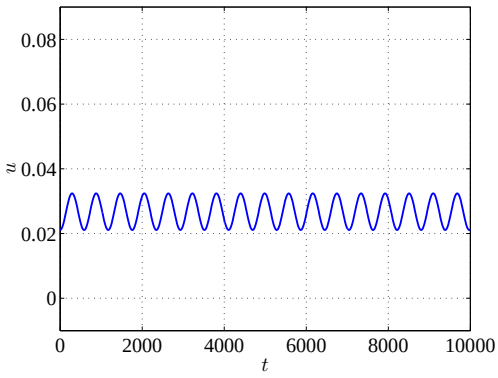

(f) $\sigma_1 = -0.0004$

Figure 9.8: Long-time histories of the micromirror response for $V_{dc} = 13.2$ V and $V_{ac} = 0.1$ V.

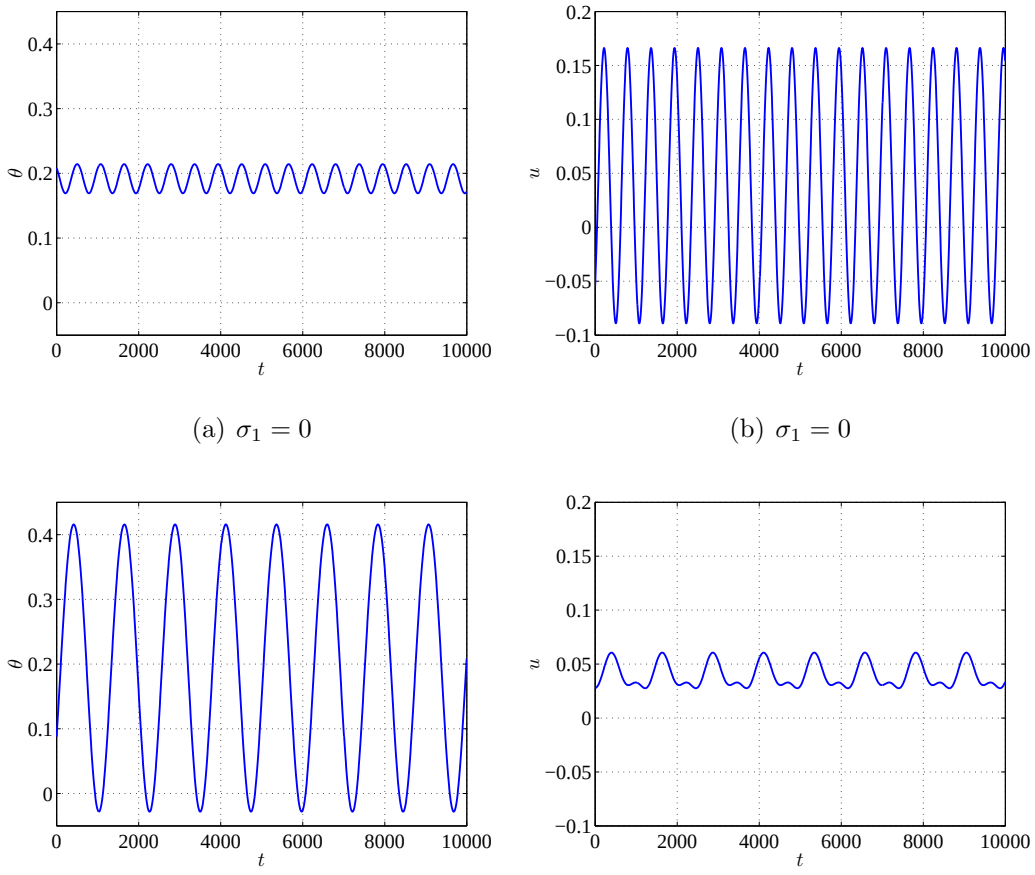

(a) $\sigma_1 = 0$ (b) $\sigma_1 = 0$

(c) $\sigma_1 = -0.0008$ (d) $\sigma_1 = -0.0008$

Figure 9.9: Long-time histories of the micromirror response for $V_{dc} = 15$ V and $V_{ac} = 0.1$ V.

looses stability through a subcritical pitchfork bifurcation at $V_{ac} \approx 0.011$ V. As a result, the response jumps to a larger stable two-mode solution. As V_{ac} is increased further, the amplitude of the first mode increases, while the amplitude of the second mode decreases slightly. Since, in our case, the quadratic and cubic nonlinearities are of the same order, no saturation occurs, and the amplitude of the second mode starts to increase again until we reach $V_{ac} \approx 0.315$ V. At this AC value, the stable two-mode solution experiences a saddle-node bifurcation, and the response jumps to the nearest stable branch, which in this case is another larger-amplitude two-mode solution. Increasing V_{ac} beyond this point results in a gradual decrease in the first-mode amplitude accompanied with a gradual increase in the

second-mode amplitude.

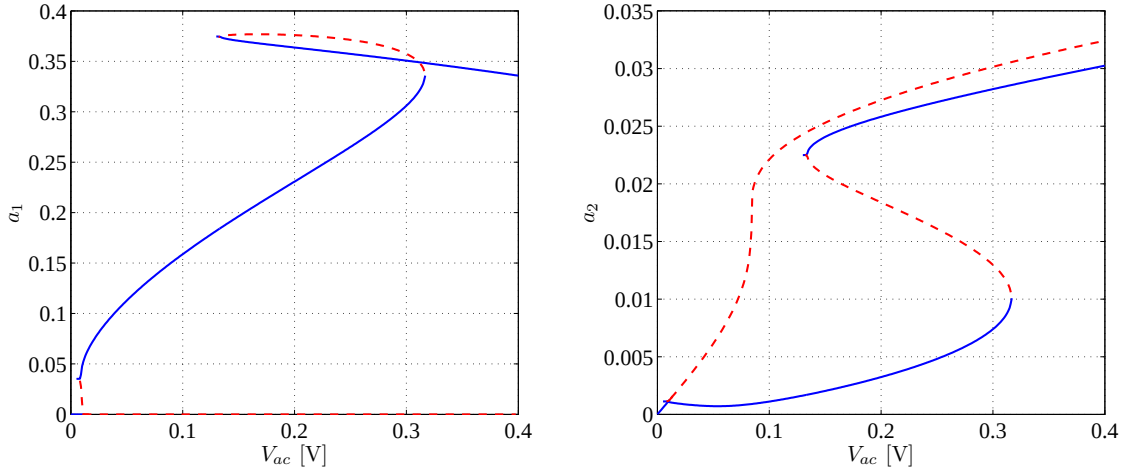

(a) (b)

Figure 9.10: Variation of the amplitudes of the first and second modes with the AC excitation voltage V_{ac} when the second mode is excited near primary resonance at a detuning value $\sigma_1 = -0.00002$ and $V_{dc} = 13.2$ V.

9.3 Redesign of Microscanners to Avoid Internal Resonances

The numerical simulations shown in Section 9.1 reveal that the internal resonance can cause serious degradation in the mirror performance. The quasiperiodic response of the scanner which may take place when the mirror is excited at primary resonance of the first mode, results in steady-state amplitude fluctuations that produce unclear images. On the other hand, when the mirror is excited near primary resonance of the second mode, as shown in Section 9.2, the second-mode amplitude does not saturate due to the considerable effects of the cubic nonlinearities, resulting in large undesirable bending oscillations.

Due to the aforementioned reasons, the designer should avoid the internal resonance. An

easy solution is to shorten the suspension beams to increase the second-mode frequency. This stems from the fact that the bending stiffness of the beams is inversely proportional to l^3. However, a decrease in l is also accompanied with an increase in the torsional stiffness of the suspension beams, which is inversely proportional to l. Hence, decreasing l results in a significant increase in the voltage required to realize a desired tilt angle. For example, to avoid the internal resonance, we decrease the length of the suspension beams from $l = 65\ \mu m$ to $l = 45\ \mu m$ keeping all other mirror parameters constant. Associated with this 30.7% decrease in the length of the suspension beams, the second-natural frequency increases significantly and is at least 40% larger than twice the natural frequency of the first mode over the whole voltage range, as shown in Fig. 9.11. However, as shown in Fig. 9.12, the pull-in voltage V_p increases by 27.3%, and the pull-in angle also increases by 12% . Although, the increase in the voltage is also associated with an increase in the tilt angle, the percentage by which the voltage changes is more than twice the percentage by which the tilt angle increases. Therefore, to achieve similar tilt angles larger voltage values are required.

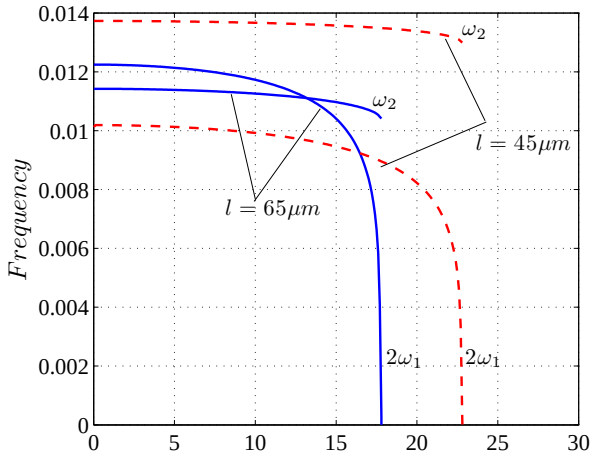

Figure 9.11: Variation of the first two natural frequencies of the mirror with the applied DC voltage. Solid lines denote suspension beams of length $l = 65\mu m$ and electrode parameters: $\alpha = 0.06$ and $\beta = 0.84$. Dashed lines denote beams of length $l = 45\mu m$ and electrode parameters: $\alpha = 0.06$ and $\beta = 0.84$.

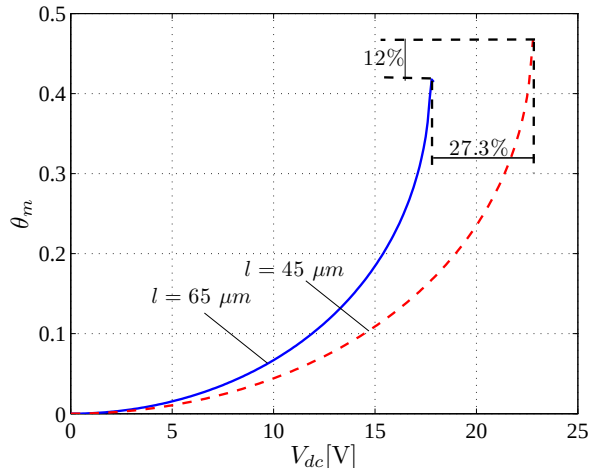

Figure 9.12: Variation of the stable equilibria of the mirror tilt angle θ_m with the applied DC voltage. Solid lines denote suspension beams of length $l = 65\mu m$ and electrode parameters: $\alpha = 0.06$ and $\beta = 0.84$. Dashed lines denote beams of dimensions $l = 45\mu m$ and electrode parameters: $\alpha = 0.06$ and $\beta = 0.84$.

Without significantly changing the natural frequencies, one can use the size and position of the electrodes to decrease the voltage required to obtain a desired tilt angle and hence produce a counter effect to shortening the suspension beams. In Chapters 5 and 6, we discussed the effects of the electrode parameters on the pull-in voltage and the natural frequencies of the mirror. We showed earlier that increasing β or α results in a significant decrease in the pull-in voltage V_p without significant effects on the corresponding natural frequencies. Therefore, in addition to shortening the beams from $l = 65\ \mu m$ to $l = 45\ \mu m$, we increase α from 0.06 to 0.20 and β from 0.84 to 1. Comparing Fig. 9.13 to Fig. 9.11 illustrates that, although the electrode parameters changed significantly, the same decrease in the length is associated with almost the same change in the natural frequencies, hence the second natural frequency increases significantly and is at least 40% larger than twice the natural frequency of the first mode over the whole voltage range. However, Fig. 9.14 demonstrates that increasing α and β results in a significant decrease in the pull-in voltage. Therefore, the pull-in voltage at $l = 45\ \mu m$ is now only 1.1% larger than that at $l = 65\ \mu m$

compared to 27.3% when the electrode parameters are kept constant.

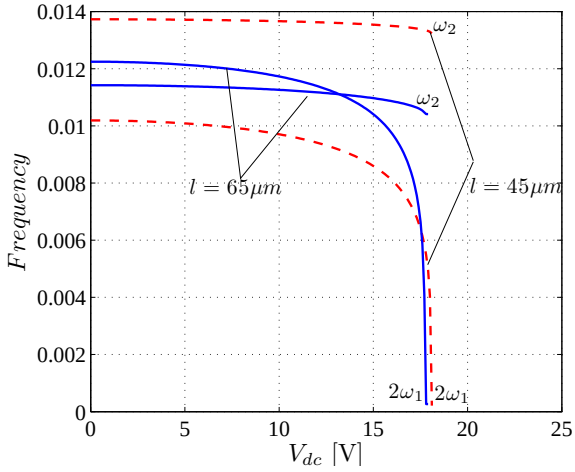

Figure 9.13: Variation of the first two natural frequencies of the mirror with the applied DC voltage. Solid lines denote suspension beams of length $l = 65\mu m$ and electrode parameters: $\alpha = 0.06$ and $\beta = 0.84$. Dashed lines denote beams of length $l = 45\mu m$ and electrode parameters: $\alpha = 0.2$ and $\beta = 1.0$.

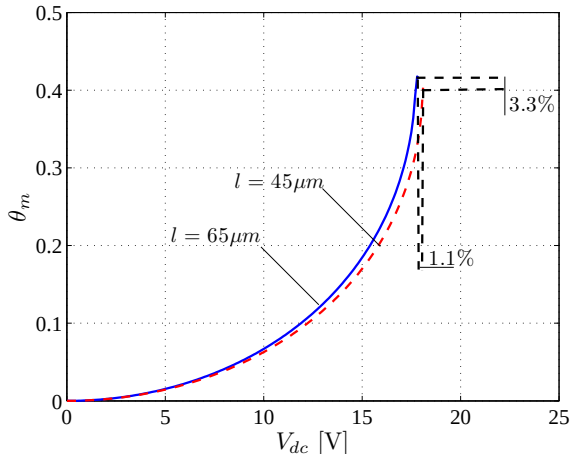

Figure 9.14: Variation of the stable equilibria of the mirror tilt angle θ_m with the applied DC voltage. Solid lines denote suspension beams of length $l = 65\mu m$ and electrode parameters: $\alpha = 0.06$, and $\beta = 0.84$. Dashed lines denote beams of length $l = 45\mu m$ and electrode parameters: $\alpha = 0.20$ and $\beta = 1.0$.

Chapter 10

Input-Shaping Control of Torsional Micromirrors

In this chapter, we develop a new technique for preshaping input commands to control torsional micromirrors. Since the electrostatic field is a nonlinear function of the states and the input voltage, the frequency of the mirror response to a step input depends on the input magnitude. As a result, traditional shaping techniques, which are based on linear theory, fail to provide good performance over the whole input range. The technique we provide combines the equations describing the static response of the mirror, a balance of energy argument, and an approximate nonlinear analytical solution of the mirror response to preshape the voltage commands. The shaped commands are then applied to drive the torsional micromirror to a desired tilt angle with zero residual vibrations. Using this approach, fast mirror switching operation with almost zero overshoot can be realized. This novel approach accounts for the energy of the significant higher modes and can be used to shape input commands applied to other nonlinear micro and macro systems.

10.1 Response of the Micromirror to Step Voltages

We start by seeking a first-order nonlinear analytical solution that describes the response of the mirror to step voltages. We show later that, since the electrostatic energy is a nonlinear function of the states, this analytical solution is an essential part of an effective shaper design. Using Equation (8.8), a first-order nonlinear solution can be written as

$$\begin{aligned} \theta(t) &= \theta_s + a_1\cos(\omega_1 t + \beta_1) + a_2\cos(\omega_2 t + \beta_2) + ... \\ u(t) &= u_s + k_1 a_1\cos(\omega_1 t + \beta_1) + k_2 a_2\cos(\omega_2 t + \beta_2) + ... \end{aligned} \tag{10.1}$$

where θ_s and u_s represent the static equilibrium position and are obtained using Equation (6.8); ω_1, ω_2, k_1, and k_2 are the natural frequencies and the associated eigenvectors which are obtained using Equation (8.9); and a_1, a_2, β_1, and β_2 are the amplitudes and phases of the response and are obtained using the following modulation equations:

$$\begin{aligned} 2\Lambda_{11}a_1' &= \Lambda_{12}a_1 \\ 2\omega_1\Lambda_{11}a_1\beta_1' &= -\frac{1}{4}(\Lambda_{14}a_1^3 + \Lambda_{15}a_1a_2^2) \\ 2\Lambda_{21}a_2' &= \Lambda_{22}a_2 \\ 2\omega_2\Lambda_{21}a_2\beta_2' &= -\frac{1}{4}(\Lambda_{24}a_2^3 + \Lambda_{25}a_2a_1^2) \end{aligned} \tag{10.2}$$

Equations (10.2) are obtained by setting V_{ac} equal to zero in Equations (8.23). The solution of Equations (10.2) can be written as

$$\begin{aligned} a_1 &= a_{11}e^{\frac{\Lambda_{12}}{2\Lambda_{11}}t}, \qquad a_2 = a_{22}e^{\frac{\Lambda_{22}}{2\Lambda_{21}}t}, \\ \beta_1 &= -\frac{1}{8\omega_1}\left(\frac{\Lambda_{14}a_{11}^2e^{\frac{\Lambda_{12}t}{\Lambda_{11}}}}{\Lambda_{12}} + \frac{\Lambda_{15}\Lambda_{21}a_{22}^2e^{\frac{\Lambda_{22}t}{\Lambda_{21}}}}{\Lambda_{11}\Lambda_{22}}\right) + \beta_{11}, \\ \beta_2 &= -\frac{1}{8\omega_1}\left(\frac{\Lambda_{24}a_{22}^2e^{\frac{\Lambda_{22}t}{\Lambda_{21}}}}{\Lambda_{22}} + \frac{\Lambda_{25}\Lambda_{11}a_{11}^2e^{\frac{\Lambda_{12}t}{\Lambda_{11}}}}{\Lambda_{21}\Lambda_{12}}\right) + \beta_{22}. \end{aligned} \tag{10.3}$$

where a_{11}, a_{22}, β_{11}, and β_{22} are constants that can be determined using initial conditions. For very large quality factors, $\Lambda_{12} = \Lambda_{22} \approx 0$, and the solution of Equations (10.2) reduces

to

$$\begin{aligned} a_1 &= a_{11}, \qquad & a_2 &= a_{22}, \\ \beta_1 &= -\frac{1}{8\omega_1\Lambda_{11}}(\Lambda_{14}a_{11}^2 + \Lambda_{15}a_{22}^2)t + \beta_{11}, \qquad & \beta_2 &= -\frac{1}{8\omega_2\Lambda_{21}}(\Lambda_{24}a_{11}^2 + \Lambda_{25}a_{22}^2)t + \beta_{22}. \end{aligned} \tag{10.4}$$

Equations (10.3) or Equations (10.4) are then substituted into Equations (10.1) to obtain a first-order nonlinear approximate solution, which describes the response of the micromirror to step voltages.

10.2 Controller Design

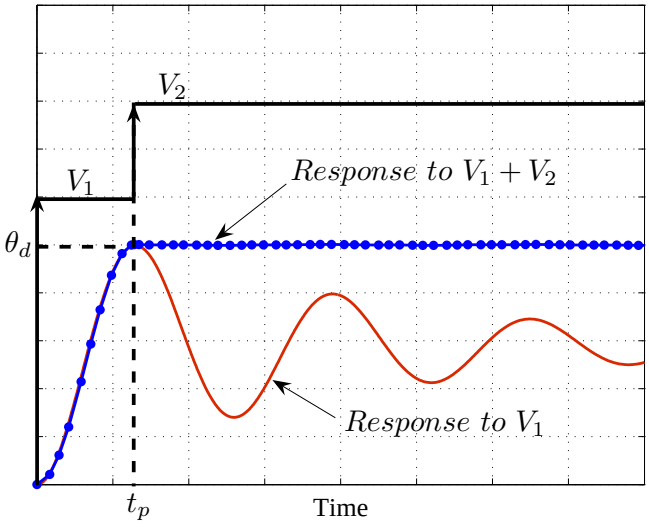

Figure 10.1: A schematic of input shaping.

In this section, we consider the problem of designing a shaper to drive the mirror to a desired tilt angle θ_d with zero vibrations. Figure 10.1 illustrates the application of two voltage impulses to obtain zero residual vibrations at the desired tilt angle. The first impulse is applied at $t = 0$ and has a magnitude V_1, computed such that the maximum overshoot of the response M_p is equal to θ_d. The time location of the second impulse is chosen at the

peak time $t = t_p$ where the velocity of the response $\dot{\theta}$ is equal to zero. The magnitude of the second impulse V_2 is applied such that the new equilibrium position is at θ_d. Ideally, if the magnitudes and locations of the impulses are chosen according to Fig. 10.1, the system is guaranteed to have zero residual vibrations at θ_d. We note that, although this shaper does not drive u to zero, it takes into account the effects of the deflection on the impulse magnitudes and locations of the shaped commands as we show later.

For linear systems, M_p and t_p are defined using simple analytical expressions [91]. Hence, they can be easily used to compute V_1 and V_2 that achieve a desired θ_d with zero residual vibrations. This idea forms the basis for the ZV and ZVD shapers' design. However, when systems exhibit a nonlinear behavior, the process is more complicated. The main reason is that, for nonlinear systems, the frequency varies with the equilibrium position. Therefore, there is no general analytical expression for M_p and t_p, thus necessitating alternate techniques to compute the shaper parameters.

To design a shaped command that takes the nonlinear effects into account, three parameters should be selected, namely, V_1, V_2, and t_p. The easiest unknown to obtain is the second impulse magnitude V_2. Knowing the desired tilt angle θ_d, which is the only input to our control algorithm, one can compute V_2 and the corresponding static deflection u_d using Equation (6.8).

Before explaining how to obtain the other two unknowns, we first provide a general expression for obtaining the peak time of the response to a general step DC voltage. The peak time t_p corresponding to the maximum tilt angle realized during the mirror response can be obtained by setting the time derivative of θ in Equation (10.1) equal to zero; that is,

$$\left.\frac{d\theta}{dt}\right|_{t_p} = 0. \tag{10.5}$$

The above equation is transcendental and is solved numerically for t_p. To obtain the fastest mirror response, we seek the solution described by the nonzero minimal peak time. Figure 10.2 demonstrates the region for which the multiple-scales solution is necessary to obtain more accurate values for t_p. We compute t_p for arbitrary step voltages over the mirror

operation regime. We compare values obtained from three types of solution to the equations in (7.8); a linear solution, a first-order nonlinear solution, and a numerical solution. Figure 10.2 illustrates that for $V_{dc} \leq 12.5$ V, the solution obtained by linearizing the equations of motion around the equilibria without considering the nonlinear effects is sufficient to realize very accurate values for t_p and hence the perturbation solution based on multiple scales is not necessary. However, for $V_{dc} \geq 12.5$ V through pull-in, the linear solution starts to deteriorate and the nonlinear solution is necessary to provide accurate values for t_p. It is worth mentioning that we also computed t_p using a second-order nonlinear approximation and found that it does not provide much improvement over the first-order approximation.

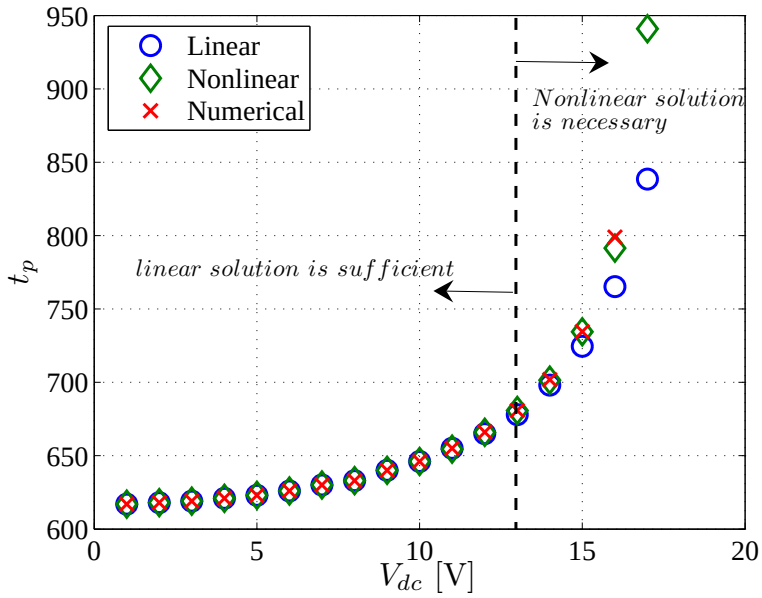

Figure 10.2: Variation of the peak time t_p with the input step voltage V_{dc}

In contrast with linear systems, it turns out that V_1 and t_p can not be obtained independently. The technique we provide combines balance of energy with the analytical approximate solution of Equations (10.1) and (10.5) in an iterative manner. To allow for better understanding of the technique, we first treat mirrors with very large quality factors where the damping is negligible. Then, we propose a technique that accounts for damping, and finally we generalize the technique for mirrors with multiple successive switching positions.

10.2.1 Input Shaping with Negligible Damping Effects

It is clear from Fig. 10.2 that the response frequency varies with the magnitude of the input voltage. Therefore, the time location of the second impulse t_p can not be obtained unless the magnitude of the first impulse V_1 is defined. We use an energy balance argument to obtain V_1. Since $\dot{\theta}$ is equal to zero at θ_d, we relate the total energy of the mirror at $t = t_p$ to the total energy at $t = 0$ using the following energy equation:

$$\frac{1}{2}k_{11}\theta_{cr}^2(\theta_d^2-\theta_0^2)+\frac{1}{2}k_{22}d^2(u^2-u_0^2)+\frac{1}{2}m_{22}d^2(\dot{u}^2-\dot{u}_0^2)-\frac{1}{2}m_{11}\theta_{cr}^2\dot{\theta}_0^2+\frac{1}{2}V_1^2(-C(t_p)+C(0))=0 \tag{10.6}$$

where C is the electrostatic capacitance and is given by Equation (5.5). If the mirror is operating from rest, θ_0, u_0, $\dot{\theta}_0$ are equal to zero at $t = 0$ and Equation (10.6) reduces to

$$\frac{1}{2}k_{11}\theta_{cr}^2\theta_d^2+\frac{1}{2}k_{22}d^2u^2+\frac{1}{2}m_{22}d^2\dot{u}^2+\frac{1}{2}V_1^2(-C(t_p)+C(0))=0. \tag{10.7}$$

We note that u in Equation (10.7) is not equal to u_d obtained using Equation (6.8). While u_d represents the equilibrium position corresponding to V_2, u is the magnitude of the deflection at t_p. Hence, $\dot{u}$ at t_p is not necessarily equal to zero. To obtain u and $\dot{u}$ at t_p, it is necessary to use the nonlinear approximate solution given by Equations (10.1), (10.4), and (10.5). However, this solution is not defined unless V_1 is obtained which in turn depends on u. This implies that V_1, u, and $\dot{u}$ should be obtained simultaneously. To this end, we employ the following iterative procedure:

1. Assume that u and $\dot{u}$ are equal to zero.
2. Solve Equation (10.7) for V_1.
3. Use the magnitude of the first impulse V_1 to obtain a first-order nonlinear approximate solution using Equations (10.1) and (10.4).
4. Use Equation (10.5) to obtain the peak time t_p.
5. Obtain new values for u and $\dot{u}$ at t_p using Equations (10.1) and (10.4).

6. Repeat the process until V_1, u and $\dot{u}$ converge.

Numerical simulations

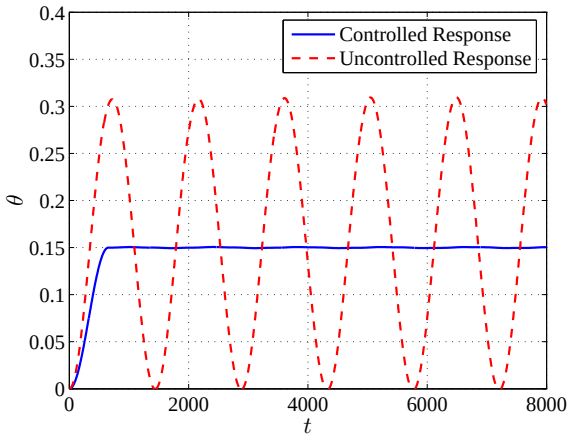

(a) Mirror Response

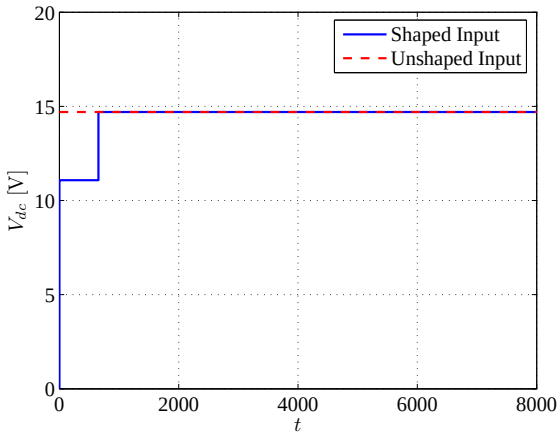

(b) Input Voltage

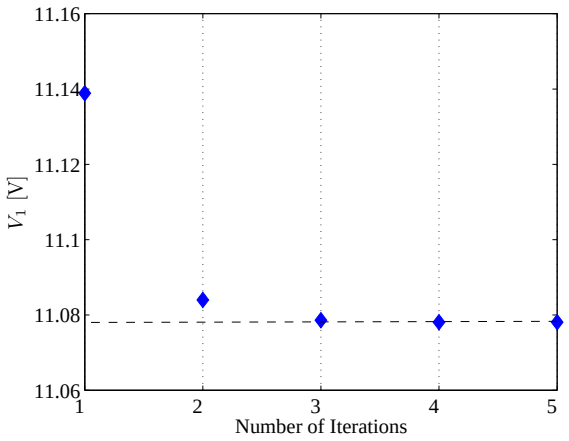

(c) Voltage Convergence

Figure 10.3: Response of the micromirror to shaped and unshaped voltages designed to drive the mirror to $\theta_d = 0.15$.

We first start by simulating two cases for mirrors without damping. These examples serve to illustrate the effectiveness and convergence of the procedure for very large quality factors. To avoid problems resulting form the two-to-one internal resonance, we choose a suspension

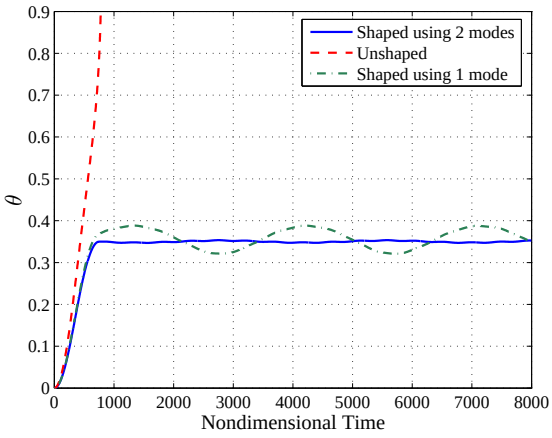

(a) Mirror Response

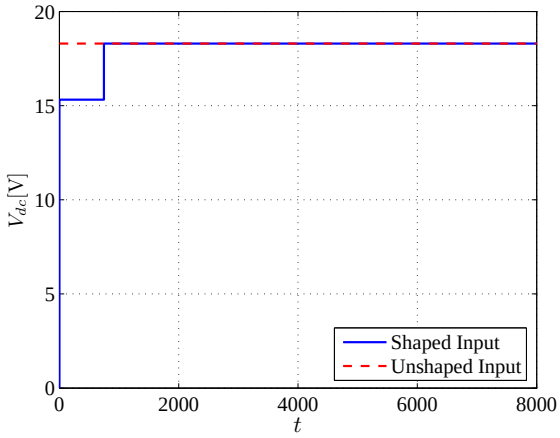

(b) Input Voltage

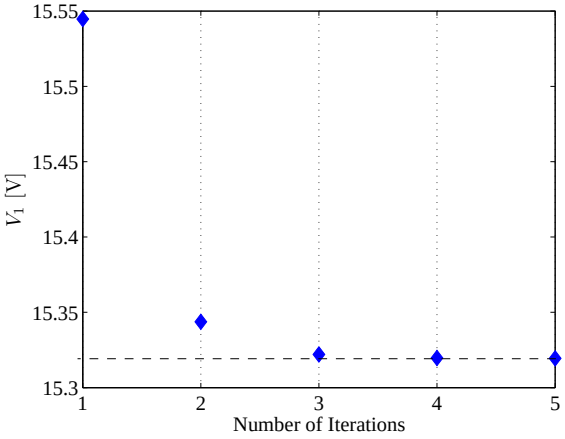

(c) Voltage Convergence

Figure 10.4: Response of the micromirror to shaped and unshaped commands designed to drive the mirror to $\theta_d = 0.35$.

beam of length $l = 45\mu m$ and electrode parameters $\alpha = 0.3$ and $\beta = 1$. In the first case, we shape a step voltage to drive the micromirror to a desired tilt angle $\theta_d = 0.15$. We start by calculating V_1 assuming that u and $\dot{u}$ are equal to zero. The value obtained from the first iteration is $V_1 = 11.14$ V. Within five iterations, the solution converges to $V_1 = 11.079$ V, as shown in Figure 10.3 (c). This value of V_1 and the corresponding value of t_p are then used to shape the input, as shown in Figure 10.3 (b). The shaped and unshaped commands

are applied to the mirror and the response is shown in Figure 10.3 (a). It is clear from the figure that, for zero damping, the shaped commands are capable of driving the mirror to the desired angle with zero residual vibrations.

In the second case, we repeat the same procedure. However, this time we choose $\theta_d = 0.35$, a tilt angle that is very close to pull-in. This illustrates the effectiveness of the procedure in the nonlinear region. Figure 10.4 (a) illustrates that, unlike the unshaped command which results in an unstable response, the shaped command is capable of realizing the desired tilt angle with almost zero residual vibrations. In Fig. 10.4 (a), we also demonstrate the effect of neglecting the higher modes on the shaper design. The figure illustrates that neglecting the energy stored in bending results in erroneous values for V_1 and t_p, which results in large residual oscillations. Therefore, even if the goal is to design a shaper for the dominant mode when the amplitudes of the higher modes are very small and do not appear in the first mode, the effect of the higher modes on the shaped command parameters can not be neglected.

10.2.2 Input Shaping with Large Damping Effects

Due to damping, energy is lost as the mirror moves form its initial position to θ_d. Therefore, to find an accurate value for V_1 and t_p, we need to account for the energy losses in Equation (10.6). An expression for the energy lost due to damping can be written as

$$EL = \frac{1}{2}\int_{t_0}^{t_p} \mu_1 \theta_{cr}^2 \dot{\theta}^2 \, dt + \frac{1}{2}\int_{t_0}^{t_p} \mu_2 d^2 \dot{u}^2 \, dt \tag{10.8}$$

where μ_1 and μ_2 are modal damping terms and given in Equation (7.8). The total energy of the mirror at $t = t_p$ can be related to the total energy at $t = t_0$ using the following energy balance equation:

$$\frac{1}{2}k_{11}\theta_{cr}^2(\theta_d^2-\theta_0^2)+\frac{1}{2}k_{22}d^2(u^2-u_0^2)+\frac{1}{2}m_{22}d^2(\dot{u}^2-\dot{u}_0^2)-\frac{1}{2}m_{11}\theta_{cr}^2\dot{\theta}_0^2+\frac{1}{2}V_1^2(-C(t_p)+C(0))+EL=0. \tag{10.9}$$

In a similar manner, we repeat the iterative procedure explained in the previous section. In

addition to assuming that u and $\dot{u}$ are equal to zero in the first step, we also assume EL is equal to zero. Equation (10.9) is then solved for V_1 and the resulting value is used to obtain a first-order nonlinear approximate solution around an equilibrium position defined by V_1. Using Equation (10.5), t_p is obtained. New values for u and $\dot{u}$ at t_p are then obtained using Equations (10.1) and (10.3). The magnitude of the energy loss EL is obtained using Equation (10.8). The new values are then used as initial guesses for the next iteration. The process is repeated until V_1, u, $\dot{u}$ and EL converge.

Numerical simulations

Figure 10.5 (a) illustrates the response of the system to shaped and unshaped commands applied to drive the mirror to $\theta_d = 0.3$. Using a single impulse voltage destabilizes the mirror. The shaped two impulse voltage, however, drives the mirror to the desired angle with less than 0.9% overshoot. Figure 10.5 (c) illustrates that the iterative procedure converges within 8 iterations compared to 5 iterations when the system is undamped. The reason is that the energy balance expression needs to compensate for EL in addition to u and $\dot{u}$.

The same technique can be extended to mirrors with multiple successive switching positions. The only difference in the process is that the final equilibrium position defined by θ_d and u_d is used as an initial condition for the next desired position. Figure (10.6) demonstrates a mirror switching successively between three different tilt angles. The mirror first tilts to $\theta_d = 0.2$, then to 0.1, and finally to 0.25. During the switching operation, the maximum mirror overshoot with shaping is $M_p = 0.75\%$ compared to $M_p = 75\%$ for the first step without shaping. Before the mirror can switch to a new tilt angle, the mirror response should settle within certain limits to allow for accurate switching. It is clear from Fig. 10.6 (a) that accurate and fast successive switching can be obtained with shaped voltages. On the other hand, unshaped voltage commands can only achieve very slow successive switching.

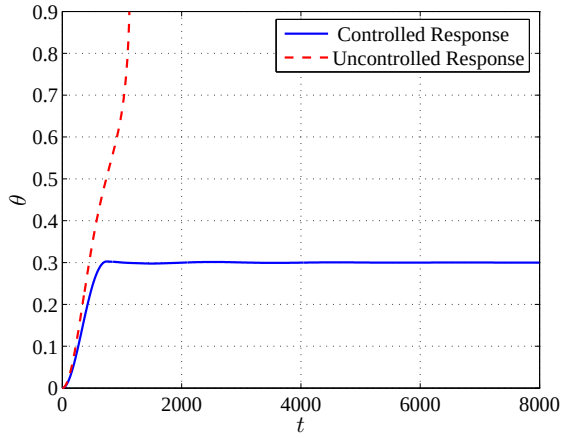

(a) Mirror Response

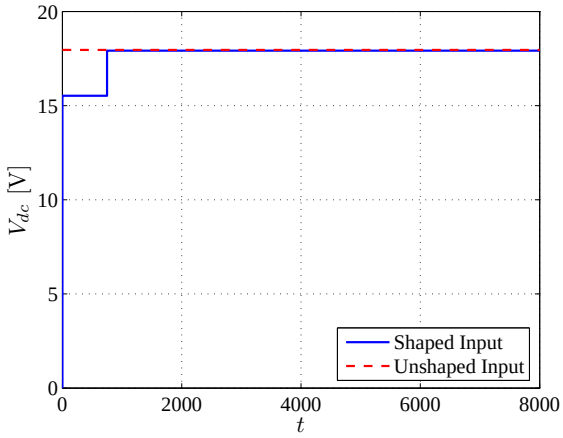

(b) Input Voltage

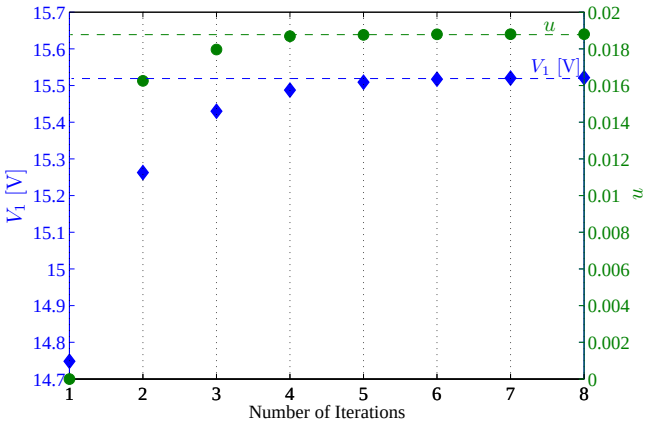

(c) Parameters Convergence

Figure 10.5: Response of the micromirror to shaped and unshaped commands designed to drive the mirror to $\theta_d = 0.30$. A quality factor $Q = 5$ is used in this simulation.

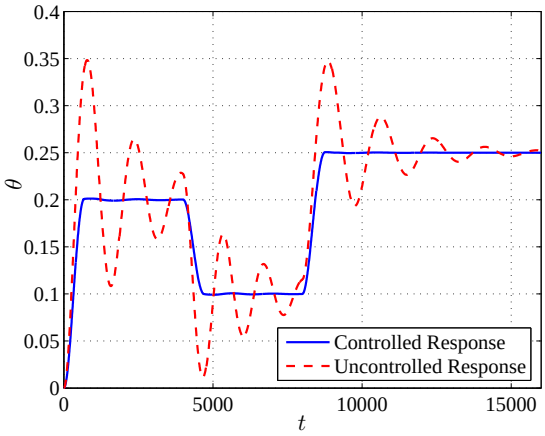

(a) Mirror Response

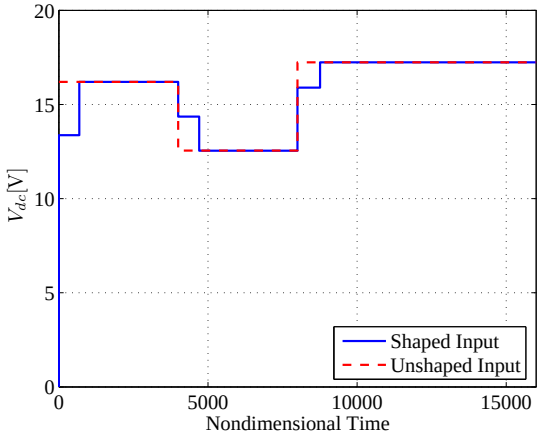

(b) Input Voltage

Figure 10.6: Response of the micromirror to shaped and unshaped commands designed to successively switch the mirror between multiple equilibrium positions. A quality factor $Q = 5$ is used in this simulation.

Chapter 11

Conclusions and Future Work

11.1 Quay-Side Container Cranes

For linear time-invariant systems, an accurate theoretical or experimental estimate of the frequency and damping ratio are enough to achieve satisfactory shaper performance. Therefore, traditional shaping techniques, such as the zero vibration shaper, are expected to perform well on these systems. However, in general, for linear time-variant or nonlinear systems, successful implementation of input-shaping controllers is highly dependent on the availability of an accurate model of the system. Our results demonstrated that a single-step input-shaping controller based on a simple pendulum model falls short of satisfying the goal of eliminating residual oscillations on quay-side container cranes. The residual oscillations obtained with a shaped acceleration profile based on a simple pendulum were as large as 2 m. The reason for this poor performance is that a simple pendulum model is not an accurate model of a quay-side container crane.

To achieve satisfactory performance, we based our shaper on an accurate constrained double-pendulum model derived from the geometry of a four-bar-mechanism model of a container crane. For predefined system parameters, the input-shaping acceleration profiles based on

a nonlinear frequency approximation of this model were capable of reducing the residual oscillations to less than 0.01 m.

Based on this model, we successfully extended input-shaping controllers to include large hoisting operations (more than 50% of the initial cable length), thereby overcoming the degradation in their performance for large hoisting operations. This new approach is based on a graphical representation of the phase portrait that describes the response of a container crane payload to a double-step acceleration profile. This controller is suitable for automated crane operations and does not require any additions to current crane-system configurations.

In contrast with single-step input-shaping controllers, the new controller is less sensitive to frequency approximations. In fact, our results showed that a nonlinear frequency approximation of the payload oscillations has a slight influence on the performance of the controller. Numerical simulations conducted on the full-model of the crane illustrated that, for different combinations of lowering and hoisting maneuvers, the double-step input-shaping controller was capable of reducing the transient and residual oscillations of the payload to less than 15 mm.

A delayed-position feedback controller was used to minimize the sensitivity of input-shaping controllers to variations in system parameters and to improve their robustness to modeling errors. Since feedback controllers do not use the maximum crane capabilities (*certain percentage of the available input goes to the feedback control signal*), we augmented the delayed-feedback controller to the preshaped commands only at the end of the transfer maneuver for a very short period of time. The feedback controller accounts for system delays, mitigates external disturbances, and compensates for uncertainties in the system. The controller was capable of reducing the residual oscillations of the payload to less than 0.05 m within 5 s of the end of the transfer maneuver.

To validate the controllers, we built a 1:10 scale model of a 65-ton container crane. This facility is unique and can be used to test new technologies that are related to payload transfer on cranes. For automated crane operations, we tested the novel double-step input-shaping

controller. Using the maximum crane capabilities, we conducted different experiments that involved large hoisting and lowering operations. The results demonstrated that the controller is capable of very fast payload transfer with less than 5 mm payload sway.

For operator-in-the-loop crane operations, input-shaping controllers do not provide an alternative. These controllers require predefined trolley and payload paths, which are not available if the operator was to operate the crane using the crane joysticks. Therefore, we used the delayed-position feedback controller analyzed in Chapter 3 to stabilize the payload for random trolley input commands and hoisting operations. The controller feedback signal was added to the operator input commands and the controller was experimentally tested. The results demonstrated that the controller is very effective in reducing payload oscillations for virtually any operator input. As a result, the controller minimizes the burdens imposed by intensive training of crane operators.

11.2 Torsional Micromirrors

We developed a comprehensive model of a torsional micromirror subjected to electric excitations. We used a Galerkin expansion in the Lagrangian to develop a reduced-order model for the system. As trial functions, we used the mode shapes of the free vibrations of a clamped-clamped beam to represent the angular motion of the mirror and the mode shapes of the free vibrations of a clamped-clamped beam with a mass at its center to represent the transverse vibrations of the mirror. We validated the static response of the reduced-order model by gradually increasing the number of assumed modes until the results converged to the exact static stable and unstable branches of the solution using 9 torsional modes and 3 bending modes. We compared the results to experimental data and showed excellent agreement. Similarly, we validated the dynamic response of the model by gradually increasing the number of assumed modes and then solving for the eigenvalues and the associated mode shapes. We found that using 8 torsional modes and 3 bending modes is sufficient to realize

convergence of the natural frequencies for voltage values ranging from zero to pull-in.

The results of the eigenvalue problem indicated that the natural frequencies of the higher modes are two orders of magnitude larger than the first two natural frequencies. Further, at zero voltage, the eigenfunctions associated with the lowest two modes are those of the first torsion and bending modes of the suspension beams. Therefore, under normal operating conditions, we found that one can treat the mirror as a lumped mass attached to two springs representing the suspension beams. This conclusion significantly facilitated further analysis of the problem.

In an attempt to provide a deep insight into the response of torsional microscanners, their design, and possible ways to improve their performance capabilities, we developed a second-order nonlinear analytical solution of the scanner's response to combined DC and AC resonance excitations. Due to the softening-type nonlinearity, we found that the frequency-response curves are bent to the left and that the bending increases as the magnitude of the DC or AC voltages increase. This nonlinear behavior causes multiple stable solutions to exist for values of the frequency that are slightly less than the natural frequency. This may result in significant jumps in the response amplitude as the AC voltage is varied.

For the given mirror parameters, we identified a region of the DC voltage in which a two-to-one internal resonance between the first two modes may be activated. The resonance occurs at a critical voltage $V_{dc} \approx 13.2$ V, but it affects a region extending from $V_{dc} \approx 12$ V to $V_{dc} \approx 15$ V. To account for the internal resonance, we developed a second-order nonlinear analytical solution that describes the response of the scanner in that region. We found that, as we excited the mirror near primary resonance of the first mode and approached the critical internal resonance voltage, the equilibrium solution of the modulation equations loses stability via two Hopf bifurcation, giving way to a region of dynamic solutions. These dynamic solutions result in undesirable quasi-periodic responses of the scanner, which can produce distorted images.

We also explored exciting the mirror near the second-mode frequency. We found that, due to

the considerable effects of the cubic nonlinearities, increasing the magnitude of the applied AC voltage does not cause the second mode response to saturate. Hence, we could not use the saturation phenomenon to obtain a large-amplitude periodic steady-state torsional response with a very small amplitude bending response.

To avoid the undesired internal resonance, we proposed a redesign approach based on changing the length of the suspension beams and the sizes and positions of the electrodes. We found that, decreasing the length of the suspension beams, did not only increase the second natural frequency, but it also resulted in a significant increase in the voltage required to realize the same tilt angles. To counter this effect, we increased the electrode parameters α and β to achieve a scanner response free of internal resonance with minimal additional voltage requirements.

Finally, we developed a novel technique for preshaping input commands applied to torsional micromirrors used for light switching applications. Unlike traditional shaping methods which are suitable for linear systems, this technique accounts for the frequency-voltage dependance resulting from the nonlinearities in the electrostatic field. Our numerical simulations illustrated that, using this approach, we can achieve very fast switching with almost zero overshoot and minimal settling time. The technique is suitable for both switching operations in the presence of large and small quality factors as well as successive variable-angle switching. Most importantly, the technique does not require any alterations to the current mirror design or feedback measurements that are very cumbersome at the micro scale.

11.3 Recommendations for Future Work

Because the research conducted in this dissertation is diverse and covers two different topics, the horizon has been expanded to explore various new research subjects at the micro and macro scales. Following an approach similar to that used in Chapter 10, a theory for input-shaping control of general nonlinear systems can be developed. This theory is expected to

have tremendous applications, especially at the micro scale, where systems are highly nonlinear and feedback measurements are very difficult and costly. The theory should account for significant effect of higher modes and similar to input shaping of linear systems, robustness constraints should also be derived. We are currently investigating the application of this theory to a microbeam subjected to a step electrostatic voltage.

We are also investigating the development of a general theory for input-shaping control of linear time-variant systems with slowly varying coefficients. In Chapter 4, we successfully demonstrated the development of an input-shaping controller for container cranes with variable cable length. Currently, we are generalizing the procedure and investigating its application to rotating flexible beams with variable length, such as flexible variable-length robot arm manipulators.

In this work and previous work conducted by Masoud et al. [92, 93], delayed-position feedback control has been shown to be a very efficient means for suppressing payload oscillations on various types of cranes. However, the application of a delayed-position feedback controller to continuous systems has not been thoroughly investigated. The application of this controller to continuous systems is expected to be more complicated. This stems from the fact that, for multimode systems, one gain-delay combination that stabilizes the lower dominant mode does not guarantee the stability of the other modes. In this aspect, we are currently investigating the application of a delayed-feedback controller to extend the travel range of a micromirror beyond the pull-in limit. However, since the equilibria are not defined beyond the pull-in point, we cannot linearize or even expand the equations of motion. Therefore, we propose a feedback linearization technique combined with a delayed-feedback controller. One problem that appears however, is that using available technologies it is extremely hard to measure both of the tilt angle and the deflection of the mirror for feedback. Therefore, an observer has to be designed for state estimation. The question is how can one guarantee the stability of the observer in the delayed-feedback measurements. This opens a whole new problem for research and investigation. In general, the area of delayed-feedback control is very rich in interesting dynamics and control problems that have not yet been explored. We

recommend further investigation of this exciting area of research.

Bibliography

[1] d'Andrea Novel B., Boustany F., and Conrad F. Control of an overhead crane: stabilization of flexibilities. In *Proceedings of the IFIP WG 7.2 Conference: Boundary Control and Boundary Variation*, pages 1–26, Sofia, France, 1990.

[2] d'Andrea Novel B., Boustany F., Conrad F., and Rad B. P. Feedback stabilization of a hybrid pde-ode system: application to an overhead crane. *Mathematics of Controls, Signals, and Systems*, 7:1–22, 1994.

[3] d'Andrea Novel B. and Boustany F. Control of an overhead crane: feedback stabilization of a hybrid pde-ode system. In *Proceedings of the* 1^{st} *European Control Conference: ECC 91*, pages 2244–2249, Grenoble, France, 1991.

[4] Joshi S. and Rahn C. D. Position control of a flexible cable of a gantry crane: Theory and experiment. In *Proceedings of the American Control Conference*, pages 2820–2824, Seattle, WA, 1995.

[5] Martindale S. C., Dawson D. M., Zhu J., and Rahn C. D. Approximate nonlinear control for a two degree of freedom overhead crane: Theory and experimentation. In *Proceedings of the American Control Conference*, pages 301–305, Seattle, WA, 1995.

[6] Rahn C. D., Zhang F., Joshi S., and Dawson D. M. Asymptotically stabilizing angle feedback for a flexible cable gantry crane. *Journal of Dynamic Systems, Measurement, and Control*, 15:563–566, 1999.

[7] Masoud Z. N. Nayfeh N. A. and Nayfeh A. H. Sway reduction on container cranes using delayed feedback controller: Simulations and experiments. In *Proceedings of the 19th Biennial ASME Conference on Mechanical Vibrations and Noise*, Chicago, IL, 2003.

[8] Nayfeh N. A. Adaption of delayed position feedback to the reduction of payload sway on container cranes. Master's thesis, Virginia Polytechnic Institute and State University, Blacksburg, VA, 2002.

[9] Smith O. J. M. *Feedback control systems*. McGraw-Hill Book Company, Inc., NY, 1st edition, 1958.

[10] Singer N. C. *Residual vibration reduction in computer controlled machines*. PhD thesis, MIT, Cambridge, MA, 1989.

[11] Singer N. C. and Seering W. P. Preshaping command inputs to reduce system vibration. *Journal of Dynamic Systems, Measurement, and Control*, 112:76–82, 1990.

[12] Singhose W. E. Shaping inputs to reduce vibration, vector diagram approach. Master's thesis, MIT, Cambridge, MA, 1989.

[13] Hyde J. M. Multimode vibration suppression in controlled flexible systems. Master's thesis, MIT, Cambridge, MA, 1991.

[14] Pao L. Y. Input shaping design of flexible systems with multiple actuators. In *Proceedings of the 13th World Congress of the International Federation of Automatic Control*, San Fransisco, CA, 1996.

[15] Smith J. Y., Kozak K., and Singhose W. E. Input shaping for a simple nonlinear system. In *Proceedings of the American Control Conference*, pages 821–826, Anchorage, AK, 2002.

[16] Alsop C. F., Forster G. A., and Holmes F. R. Ore unloader automation - a feasibility study. In *Proceedings of IFAC Workshop on Systems Engineering for Control Systems*, pages 295–305, Tokyo, Japan, 1965.

[17] Jones J. F. and Petterson B. J. Oscillation damped movement of suspended objects. In *Proceedings of the IEEE International Conference on Robotics and Automation*, pages 956–962, Philadelphia, PA, 1988.

[18] Dadone P. and Vanlandinham H. F. Load transfer control for a gantry crane with arbitrary delay constraints. *Journal of Vibration and Control*, 7:135–158, 2001.

[19] Alzinger E. and Brozovic V. Automation and control system for grab cranes. *Brown Boveri Review*, 7:351–356, 1983.

[20] Starr G. P. Swing-free transport of suspended objects with a path-controlled robot manipulator. *Journal of Dynamic Systems, Measurement, and Control*, 107:97–100, 1985.

[21] Strip D. R. Swing-free transport of suspended objects: A general treatment. *IEEE Transactions on Robotics and Automation*, 5(2):234–236, 1989.

[22] Singer N. C., Singhose W. E., and Krikku E. An input shaping controller enabling cranes to move without sway. In *ANS Seventh Topical Meeting on Robotics and Remote Systems*, Augusta, GA, 1997.

[23] Kress R. L., Jansen J. F., and Noakes M. W. Experimental implementation of a robust damped-oscillation control algorithm on a full-sized, two-degree-of-freedom, ac induction motor-driven crane. In *Proceedings of the 5th International Symposium on Robotics and Manufacturing: Research, Education, and Applications: ISRAM'94*, pages 585–592, Maui, HI, 1994.

[24] Parker G. G., Groom K., Hurtado J., Robinett R. D., and Leban F. Command shaping boom crane control system with nonlinear inputs. In *Proceedings of the IEEE International Conference on Control Applications*, pages 1774–1778, Kohala Coast, HI, 1999.

[25] Parker G. G., Groom K., Hurtado J. E., Feddema J., Robinett R. D., and Leban

F. Experimental verification of a command shaping boom crane control system. In *Proceedings of the American Control Conference*, pages 86–90, San Diego, CA, 1999.

[26] Singhose W. E., Porter L. J., and Seering W. P. Input shaped control of a planar crane with hoisting. In *Proceedings of the American Control Conference*, pages 97–100, Albuquerque, NM, 1997.

[27] Singhose W. E., Porter L. J., Kenison M., and Kriikku E. Effect of hoisting on the input shaping control of gantry cranes. *Control Engineering Practice*, 8:1159–1165, 2000.

[28] Abdel-Rahman E. M. Nayfeh A. H. and Masoud Z. N. Dynamics and control of cranes: A review. *Journal of Vibration and Control*, 5:863–908, 2003.

[29] Hazlerigg A. D. G. Automatic control of crane operations. In *Proceedings of the IFAC 5th World Congress*, volume 1, Paris, France, 1972.

[30] Ohnishi E., Tsuboi I., Egusa T., and Uesugi M. Automatic control of crane operations. In *Proceedings of the IFAC 8th triennial World Congress*, pages 1885–1890, Kyoto, Japan, 1981.

[31] Ridout A. J. Anti swing control of the overhead crane using linear feedback. *Journal of Electrical and Electronics Engineering*, 9:17–26, 1987.

[32] Virkkunen J. and Marttinen A. Computer control of a loading bridge. In *Proceedings of the IEE International Conference: Control '88*, pages 484–488, Oxford, UK, 1988.

[33] Caron B., Perrad P., and Rozinoer J. Reference model control of a variable length overhead crane. In *Low Cost Automation: Techniques, Components, Instruments, and Applications*, pages 475–480, Milan, Italy, 1989.

[34] Moustafa K. A. F. Feedback control of overhead cranes swing with variable rope length. In *Proceedings of the American Control Conference*, pages 691–695, Baltimore, MD, 1994.

[35] Lee H.-H., Cho S.-K., and Cho J.-S. Feedback control of overhead cranes swing with variable rope length. In *Proceedings of the IFAC International Workshop on Automation in the Steel Industry*, pages 115–120, Kyongju, Korea, 1997.

[36] Yong-Seok A., Hyungbo S., Hidemasa Y., Naoki F., Hideshi K., and Seung-Ki S. A new vision-sensorless anti-sway control system for container cranes. In *IEEE Industry Applications Conference*, pages 262–269, Salt Lake City, UT, 2003.

[37] Yong-Seok A., Hyungbo S., Hidemasa Y., Naoki F., Hideshi K., and Seung-Ki S. Anti-sway control of container cranes: Inclinometer, observer, and state feedback. *International Journal of Control, Automation, and Systems*, 2(4):435–449, 2004.

[38] Zinober A. S. I. The self-adaptive control of an overhead crane operations. In *Proceedings of the 5th IFAC Symposium on Identification and System Parameter Estimation*, pages 1161–1167, Darmstadt, East Germany, 1979.

[39] DeSantis R. M. and Krau S. Bang bang motion of a cartesian crane. *Robotica*, 12:174–177, 1994.

[40] Yu J., Lewis F. L., and Huang T. Nonlinear feedback control of a gantry crane. In *Proceedings of the American Control Conference*, pages 4310–4315, Seattle, WA, 1995.

[41] Pyragas K. Continuous control of chaos by self-controlling feedback. *Physics Letters*, A 170:421–428, 1992.

[42] Gregory D. V. and Rajarshi R. Chaotic communication using time-delayed optical systems. *International Journal of Bifurcations and Chaos*, 9:2129–2156, 1999.

[43] Masoud Z. N., Nayfeh A. H., and Al-Mousa A. Delayed-position feedback controller for the reduction of payload pendulations on rotary cranes. *Journal of Vibration and Control*, 8:1–21, 2002.

[44] Masoud Z. N., Daqaq M. F., and Nayfeh N. Pendulation reduction on small ship mounted telescopic cranes. *Journal of Vibration and Control*, 10(8):1167–1181, 2004.

[45] Pacora L. M. and Carroll T. L. Synchronization in chaotic systems. *Physics Review Letter*, 64:821–824, 1990.

[46] Cheng C. C. and Chen C. Y. Controller design of an overhead crane system with uncertainties. *Control Engineering Practise*, 4:645–653, 1996.

[47] Nayfeh N. A., Masoud Z. N., and Bawmann W. A comparison of three feedback controllers for container cranes. In *Proceedings of the ASME 2005 International Design Engineering Technical Conferences*, Long Beach, CA, 2005.

[48] Computer Optics Inc. *http://www.piezomems.com*.

[49] Ford J. E., Aksyuk V. A., Bishop D. J., and Walker J. A. Wavelength add-drop switching using tilting micromirrors. *Journal of Lightwave Technology*, 17(5):904–911, 1999.

[50] Walker J. A. The future of mems in telecommunication networks. *Journal of Hydromechanics and Microengineering*, 10:R1–R7, 2000.

[51] Lin L. Y., Goldstein A. L., and Tkach R. W. Free-space micromachined optical switches for optical networking. *IEEE Journal for Selected Topics in Quantum Electronics*, 5(1), 1999.

[52] Glimmerglass 2006. *http://www.glimmerglass.com*.

[53] Associated Press. New fiber-optic technology unveiled. Technical report, USA Today Tech Reviews, November, 1999.

[54] Van Kessel P. F., Hornbeck L. J., Meier R. E., and Douglass M. R. Mems-based projection display. *Proceedings of the IEEE*, 86(8):1687–1704, 1998.

[55] Hornbeck L. J. Projection displays and mems: Timely convergence for a bright future. In *Proceedings of the SPIE*, volume 2639, Austin, TX, 1995.

[56] Hornbeck L. J. Digital light processing update-status and future applications. *Proceedings of the SPIE*, 3634:158–170, 1999.

[57] Texas Instruments 2006. *http://www.dlp.com*.

[58] Fan L. and Yu M. C. Two dimensional optical scanners with large angular rotation realized by self-assembled micro-elevator. In *Proceedings of the IEEE LEOS Summer Topical Meeting on Optical MEMS*, pages 107–108, Monterey, CA, 1998.

[59] Peter Y., Herzig H. P., Etienne R., Dadlinker R., Marxer C., and de Rooij F. N. Pulsed fiber laser using mico-electro-mechanical mirrors. *Optical Engineering*, 38(4):636–640, 1999.

[60] Collins D. R., Sampsell J. B., Hornbeck L. J., Florence P. A., Penz P. A., and Gately M. T. Application of improved deformable mirror array technology to neural network realization. *Neural Netwroks*, 1(1):378–382, 1988.

[61] Cohn R. W. and Sampsell J. B. Deformable mirror device uses in frequency excision and optical switching. *Applied Optics*, 27:937–940, 1988.

[62] Hornbeck L. J. 128 multiplied by 128 deformable mirror device. *IEEE Transactions on Electron Devices*, 30(5):539–545, 1983.

[63] Osterberg P. M. *Electrostatically actuated microelectromechanical test structures for material property measurements*. PhD thesis, MIT, Cambridge, MA, 1995.

[64] Hornbeck L. J. Deformable-mirror spatial light modulators. *SPIE Critical Review Series*, 1150:86–102, 1989.

[65] Degani O. B., Socher E., Lipson A., Leitner T., Setter D. J., Kaldor S., and Nemirovisky Y. Pull-in study of an electrostatic torsion microactuator. *Journal of Microelectromechanical Systems*, 7(4):373–379, 1998.

[66] Nemirovisky Y. and Degani O. B. A methodology and model for the pull-in parameters of electrostatic actuators. *Journal of Microelectromechanical Systems*, 10(4):601–614, 2001.

[67] Degani O. B. and Nemirovisky Y. Design considerations of rectangular electrostatic torsion actuators based on new analytical pull-in expressions. *Journal of Microelectromechanical Systems*, 11(1):20–26, 2002.

[68] Hah D., Toshiyoshi H., and Wu M. Design of electrostatic actuators for moems applications. *Proceedings of the SPIE*, 4755:200–207, 2002.

[69] Zhang X. M., Chau F. S., Quan C., and Liu A. Q. Modeling of the optical torsion micromirror. In *Proceedings of the SPIE Conference on Photonics Technology in the 21st Century: Semiconductors, Microstructures, and Nanostructures*, pages 109–116, Singapore, 1999.

[70] Zhang X. M., Chau F. S., Quan C., Lam Y. L., and Liu A. Q. Study of the static characteristics of a torsional micromirror. *Journal of Microelectromechanical Systems*, 90:73–81, 2001.

[71] Xiao Z., Wu X. T., Wuyong P., and Farmer K. R. An angle-based design approach for rectangular electrostatic torsion actuators. *Journal of Microelectromechanical Systems*, 10(4):561–568, 2001.

[72] Guardia N. R., Ainger R., Nessler W., Handtmann M., and Castaner L. M. Control positioning of torsional electrostatic actuators by current driving. In *Proceedings of the Third International Euro Conference on Advanced Semiconductor Devices and Microsystems*, pages 91–94, Slovakia, 2000.

[73] Wetzel G. C. and Strozewski K. J. Dynamical model of microscale electromechanical spatial light modulator. *Journal of Applied Physics*, 73(11):7120–7124, 1993.

[74] Camon H. and Lanaudi F. Fabrication, simulation, and experiment of a rotating electrostatic silicon mirror with large angular deflections. In *Proceedings of the IEEE Micro Electro Mechanical Systems (MEMS)*, pages 645–650, Japan, 2000.

[75] Sattler R., Florian P., Fattinger G., and Wachutka G. Modeling of an electrostatic torsional actuator: Demonstrated with an rf mems switch. *Sensors and Actuators A*, 97:337–346, 2002.

[76] Degani O. B. and Nemirovisky Y. Modeling the pull-in parameters of electrostatic actuators with a novel lumped two degrees of freedom pull-in model. *Sensors and Actuators A*, 97-98:569–578, 2002.

[77] Huang J. M., Liu A. Q., Deng Z. L., Zhang Q. X., Ahn J., and Asundi A. An approach to the coupling effect between torsion and bending for electrostatic torsional micromirrors. *Sensors and Actuators A*, 115:159–167, 2004.

[78] Zhao J. P., Chen H. L., Huang J. M., and Liu A. Q. A study of dynamic characterestics and simulations of mems torsional micromirror. *Sensors and Actuators A*, 120:199–210, 2005.

[79] Chen L. and Lee C. Design and modeling for comb drive actuator with enlarged static displacement. *Sensors and Actuators A*, 115:530–539, 2004.

[80] Borovic B., Liu A. Q., Popa D., Cai H., and Lewis F. L. Open-loop versus closed-loop control of mems devices, choices and issues. *Journal of Micromechanics and Microengineering*, 15:1917–1924, 2005.

[81] Popa D., Hun Kang B., Wen J., Stephanou H., Skdimore G., and Geisberger A. Dynamic modeling and input shaping of thermal biomorph mems actuators. In *Proceedings of the 2003 IEEE International Conference on Robotics and Automation*, pages 1470–1475, Taipei, Taiwan, 2003.

[82] Chiou J. C., Lin Y. C., and Wu S. D. Closed-loop fuzzy control of torsional micromirror with multiple electrostatic electrodes. In *Proceedings of the IEEE/LEOS International Conference on Optical MEMs*, pages 85–86, Lugano, Switzerland, 2002.

[83] Liao K.-M., Wang Y.-C., Yeh C.-H., and Chen R. Closed-loop adaptive control for torsional micromirrors. In *Proceedings of the SPIE*, pages 184–193, Bellingham, WA, 2004.

[84] Sane H. S., Yazdi N., and Carlos H. M. Application of sliding mode control to electrostatically actuated two-axis gimbaled micromirrors. In *Proceedings of the American Control Conference*, pages 3726–3731, Denver, Co, 2003.

[85] Blajer W. and Kolodziejczyk A. A geometric approach to solving problems of control constraints: Theory and a dae framework. *Multibody System Dynamics*, 11(4):343–364, 2004.

[86] Nayfeh A. H. *Introduction to perturbation techniques*. Wiley-Interscience, New York, 1981.

[87] Pao L. Y. An analysis of the frequency, damping, and total insensitivies of input shaping designs. *AIAA Journal on Guidance, Control, and Dynamics*, 20(5):909–915, 1997.

[88] Nayfeh A. H. *Nonlinear Interactions*. Wiley-Interscience, New York, 2000.

[89] Nayfeh A. H. and Mook D. T. *Nonlinear Oscillations*. Wiley-Interscience, New York, 1979.

[90] Nayfeh A. H. Resolving controversies in the application of the method of multiple scales and the generalized method of averaging. *Nonlinear Dynamics*, 40:61–102, 2005.

[91] Ogata K. *Modern Control Engineering*. Prentice-Hall, New Jersey, 2002.

[92] Masoud Z. N., Nayfeh A. H., and Al-Mousa A. Delayed position-feedback controller for the reduction of payload pendulations of rotary cranes. *Journal of Vibration and Control*, 8:1–21, 2001.

[93] Masoud Z. N., Daqaq M. F., and Nayfeh N. A. Pendulation reduction on small ship-mpounted telescopic cranes. *Journal of Vibration and Control*, 10:1167–1179, 2001.

Vita

Mohammed F. Daqaq was born on May 15, 1979 in the city of Bethlehem, Palestine. He lived there until 1996 where he graduated form the Evangelical Lutheran "Talitha Kumi" high school. In October 1996, he moved to Irbid, Jordan. He joined Jordan University of Science and Technology and received a Bachelor of Science degree in Mechanical Engineering in January 2001. In July 2001, he moved to Blacksburg, Virginia, where he joined the Department of Engineering Science and Mechanics at Virginia Polytechnic Institute and State University (Virginia Tech). He received his Master of Science degree in Engineering Mechanics on May 9, 2003 and his Doctor of Philosophy degree in Engineering Mechanics on July 28, 2006. In August 2006, he will join Clemson University as an assistant professor of mechanical engineering.